Study on Nanostructured Pb(Zr,Ti)O_3 for Piezoelectric Energy Harvesting

A doctoral dissertation
Department of Energy Engineering
Graduate School of Engineering
Nagoya University

SONG Jundong
January 2021

Contents

Contents 2

Chapter 1 - General introduction 1

1.1 Research background 1

1.1.1 Piezoelectricity and ferroelectricity 1

1.1.2 Piezoelectric energy harvesting 3

1.1.3 Piezoelectric materials for PEH 5

1.2 Research topics on improving FOM of piezoelectric materials 5

1.2.1 Polarization rotation controlled by the MPB composition 6

1.2.2 Polarization rotation controlled by the external field 7

1.3 Objective and organization of the dissertation 8

1.3.1 Objective of this study 8

1.3.2 Organization of the thesis 9

1.4 References 11

Chapter 2 - Theoretical analysis on the output performance of piezoelectric nanorod arrays 15

2.1 Introduction 15

2.2 Theoretical models 15

2.2.1 Direct d_{33} of a clamped film 15

2.2.2 Output performance of the nanorod array 17

2.2.3 Theoretical models analyzed via the finite-element method 19

2.3 Results and discussion 20

2.3.1 Effect of the aspect ratio 20

2.3.2 Effect of the density of the nanorod array 22

2.3.3 Comparison of devices in the 33 and 31 modes 24

2.4 Conclusion 27

2.5 References 27

Chapter 3 - Enhanced FOM from the decreased density of PZT nanorod arrays 29

3.1 Introduction 29

3.2 Experimental 30

3.3 Results and discussion 31

3.3.1 Morphology and crystal structure 31

3.3.2 Dielectric and piezoelectric properties 33

3.3.3 Evaluation of $\mathrm{FOM}_{\mathrm{eff}}$ 35

3.4 Conclusion 37

3.5 References 38

Chapter 4 - Fabrication of PZT nanorods by RF-magnetron sputtering 40

4.1 Introduction 40
4.2 Experimental 41
4.3 Result and discussion 42
4.3.1 Effect of Pb content, T–S distance and thickness 42
4.3.2 Effect of temperature and pressure 44
4.4 Conclusion 47
4.5 References 47
Chapter 5 - Theoretical analysis on piezoelectric response of ferroelectric superlattice films 49
5.1 Introduction 49
5.2 Model building 50
5.2.1 Single-layer films 50
5.2.2 Superlattice films with two types of PZT 53
5.3 Results and discussion 54
5.3.1 u_m-E_{ext} phase diagrams for single-layer films and the superlattice film 54
5.3.2 Polarization state for the superlattice film 57
5.3.3 Dielectric constant of single-layer films 59
5.3.4 Piezoelectric response of single-layer films and superlattice films 60
5.4 Conclusion 64
5.5 References 65
Chapter 6 - Large piezoelectric response from polarization rotation in artificial superlattice films 66
6.1 Introduction 66
6.2 Experimental 66
6.3 Results and discussion 67
6.3.1 Crystallinity, periodicity and the polarization state of superlattice films 67
6.3.2 Dielectric and piezoelectric properties of superlattice films 70
6.4 Conclusion 72
6.5 References 73
Chapter 7 - General conclusion and future prospective 74
7.1 General conclusion 74
7.2 Positioning and meaning of this research method 76
7.3 Future perspective 77
7.4 References 78
Appendix 79
Accomplishments 84
Acknowledgements 86

Chapter 1 - General introduction

1.1 Research background

1.1.1 Piezoelectricity and ferroelectricity

Piezoelectricity is an electromechanical phenomenon that convert mechanical energy into electric energy (known as the direct piezoelectricity), and vice versa (known as the converse piezoelectricity). The knowledge about piezoelectric effect originated from 1880s, when the Curie brothers discovered that electric charges in quartz can be generated by applying pressure on it [1,2]. Since that time, however, piezoelectric materials had not been widely used owing to their fairly low Curie temperature and other unstable chemical properties. Not until 1940s, the discovery of a piezoelectric perovskite material, barium titanate ($BaTiO_3$, BT) [3–5], had formally initiated the application of piezoelectric materials and devices owing to a Curie temperature T_c over 120 °C. In 1954, Jaffe [6] observed a giant piezoelectric response in lead zirconate titanate ($Pb(Zr,Ti)O_3$, PZT) with the composition around morphotropic phase boundary (MPB) [7]. As the PZT phase diagram [8] illustrates in Figure 1-1, PZT with a Zr/Ti ratio of 52/48, which locates at the phase transition boundary between a tetragonal crystal and a rhombohedral, can easily cause a discontinuous change of the physical properties. The discovery of PZT and MPB became a milestone in the development of piezoelectric materials and devices, and have been changing the world until today.

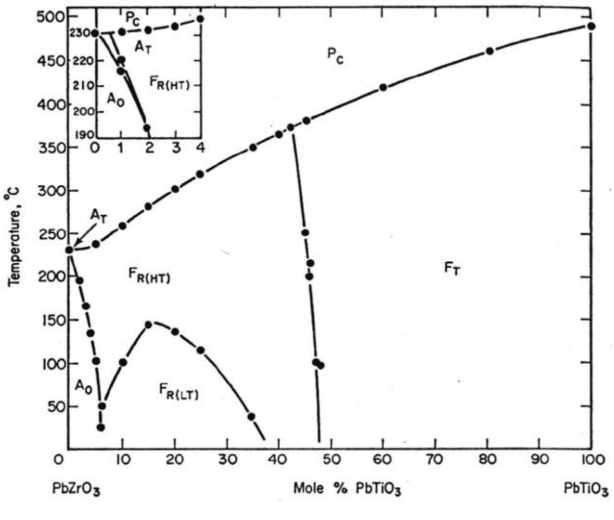

Figure 1-1 Phase diagram for PZT [8]. P_C, F_T, F_R, A_T and A_O represent paraelectric cubic, ferroelectric tetragonal, ferroelectric rhombohedral, and antiferroelectric tetragonal and antiferroelectric orthorhombic phases, respectively.

Among a variety of piezoelectric materials, there is one the polarization of which can be rearranged by an external electric field, and even exists in the absence of the electric field. This phenomenon is called ferroelectricity, which was first discovered by Valasek [9] who observed a hysteretic relationship between the polarization (P) and the external electric field (E) in Rochelle salt in 1920s. Figure 1-2 shows a typical

P-E relationship [10], known as a hysteresis loop for ferroelectric materials. In general, a piece of ferroelectric material contains many domains in random directions and need to be poled by applying an external electric field for utilization. After all the ferroelectric domains are switched to a preferred direction during poling, P becomes a linear function of E along the line BC shown in the figure. The P intercept of BC is called saturated polarization, P_s, which reflects the intrinsic polarization in the material. When reducing E afterwards, P decreases as the ferroelectric domains partially switch back to the initial state. When E goes back to zero, there are still a number of domains maintaining the preferred direction, causing a remnant polarization P_r at $E = 0$. Continuing applying a reverse E, P further decreases from P_s to zero at $-E_\mathrm{c}$, and the similar behaviors start in the opposite direction. The reverse E that is able to cancel P_s is called coercive electric field E_c.

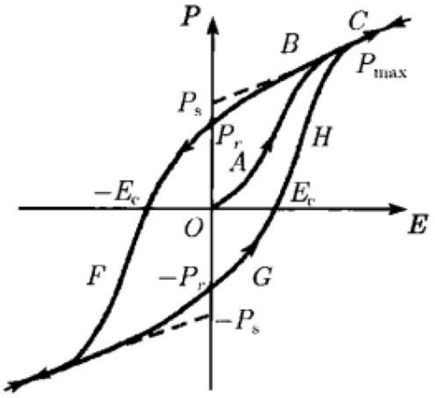

Figure 1-2 A typical hysteresis loop for ferroelectric materials [10].

A representative ferroelectric is the perovskite structure, with a general chemical formula of ABO_3 such as BT and PZT. As an example of the PZT atom structure shown in Figure 1-3 [10], Pb^{2+} of A-sites and Zr^{4+}/Ti^{4+} of B-sites are located at the center of oxygen octahedra, showing the coincidence of the centers of positive and negative charges. When the temperature goes down below T_c, the cubic perovskite will transform into a tetragonal structure and an electric dipole is produced by the ions deviated from the symmetric position, as shown in Figure 1-3(b). Since the dipole moment varies with the change of the ion position which can be affected by external pressure, the material exhibits piezoelectricity. This also indicates that the piezoelectricity and ferroelectricity must exist in the materials with a non-centrosymmetric point group, whereas the centers of positive and negative charges will always coincide for the centrosymmetric crystals.

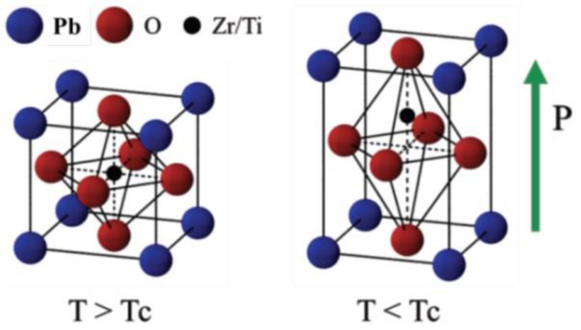

Figure 1-3 Perovskite structure of PZT [10]. (a) The cubic phase above Curie temperature. (b) The tetragonal phase below Curie temperature, in which the deviation of atoms exhibits piezoelectricity.

Apart from piezoelectricity, many factors, e.g. heat, light, etc., can affect the electric dipole and thus derive various interesting phenomena that achieve mutual conversion among different sorts of energy, as listed in Table 1-1 [11]. Materials with those off-diagonal coupling properties are known as “smart” materials, which can be utilized in multiple fields as high-permittivity dielectrics, piezoelectric/pyroelectric/electro-optic sensors and actuators, etc. Although ferroelectric materials have not achieved the industrial application in some areas where competitive materials exist, their promising potential in miniaturized and integrated devices has been attracting considerable interests and efforts from researchers and experts.

Table 1-1 Various effects in materials [11]

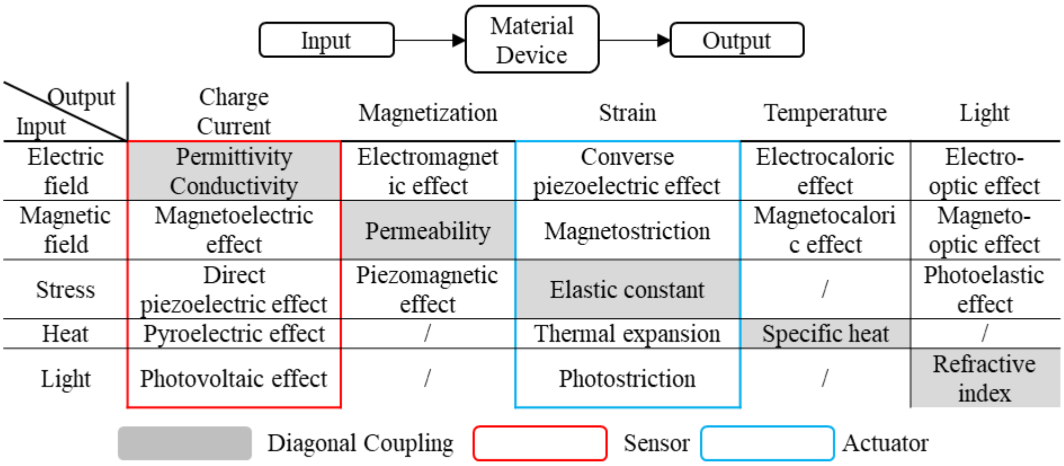

Input → Material Device → Output

Output / Input	Charge Current	Magnetization	Strain	Temperature	Light
Electric field	Permittivity Conductivity	Electromagnetic effect	Converse piezoelectric effect	Electrocaloric effect	Electro-optic effect
Magnetic field	Magnetoelectric effect	Permeability	Magnetostriction	Magnetocaloric effect	Magneto-optic effect
Stress	Direct piezoelectric effect	Piezomagnetic effect	Elastic constant	/	Photoelastic effect
Heat	Pyroelectric effect	/	Thermal expansion	Specific heat	/
Light	Photovoltaic effect	/	Photostriction	/	Refractive index

▨ Diagonal Coupling ▭ Sensor ▭ Actuator

1.1.2 Piezoelectric energy harvesting

Since the industrial revolution, excessive exploit of fossil fuels has made a negative impact on the global environment. Toughing issues such as air pollution and global warming are calling for reasonable and effective utilization of non-renewable resources as well as the exploit and application of eco-friendly energy sources, e.g. solar, wind, hydra, biomass, etc. [12]. As one of the promising technologies to produce renewable energy, energy harvesting PEH, that converts the ambient energy to electric power, has received much attention. In addition, energy harvesting plays an important role in the development of micro-electromechanical systems (MEMSs). For those wireless sensors and actuators that operate in the remote area where replacing the battery will be a demanding task or even impossible, energy harvesting will become an expected solution [13].

Among three mechanisms to convert mechanical energy to electric power: (1) electromagnetic [14-15], (2) electrostatic [16] and (3) piezoelectric, piezoelectric energy harvesting (PEH) can be easily integrated with other transducers to create self-powered devices due to the rapid electromechanical response [17-18]. The inspiration of using piezoelectric materials to generate electrics derived from piezoelectric dampers, which intended to consume kinetic energy more rapidly [19-20]. However, instead of wasting the generated power by converting to Joule heat, many problems in piezoelectric configuration, circuitry, power storage, etc. need to be deal with. Until now, there has not been an absolutely clear criterion to evaluate the output performance of PEH devices. Most studies evaluate the output voltage or active power, but it is difficult to compare them with each other due to the diverse vibration source and device configuration.

To simplify the discussion and highlight the effect of piezoelectric materials on PEH, the output performance in this dissertation is evaluated mainly based on the piezoelectric configuration. Figure 1-4 shows two basic working modes for piezoelectric materials. Here, available energy E_a, which is proportional to the output power, is expressed as Eq. (1-1) in the model of charging a parallel plate capacitor.

$$E_a = \frac{1}{2}CV^2 \tag{1-1}$$

where C stands for the capacitance of the piezoelectric materials, V the voltage generated by applying a mechanical stress σ. C is known as Eq. (1-2) with the dimension given in Figure 1-4,

$$C = \frac{\varepsilon ab}{h} \tag{1-2}$$

where ε is the dielectric constant of the piezoelectric materials. According to the piezoelectric equation, V in the 33 mode (Figure 1-4(a)) and the 31 mode (Figure 1-4(b)) is expressed as Eqs. (1-3) and (1-4), respectively.

$$V = \frac{d_{33}}{\varepsilon}\sigma h \tag{1-3}$$

$$V = \frac{d_{31}}{\varepsilon}\sigma h \tag{1-4}$$

Substituting Eqs. (1-2)–(1-4) for Eq. (1-1), E_a becomes

$$E_a = \frac{1}{2}\frac{d_{33}^2}{\varepsilon}\sigma^2(abh) \quad \text{for the 33 mode,} \tag{1-5}$$

$$E_a = \frac{1}{2}\frac{d_{31}^2}{\varepsilon}\sigma^2(abh) \quad \text{for the 31 mode.} \tag{1-6}$$

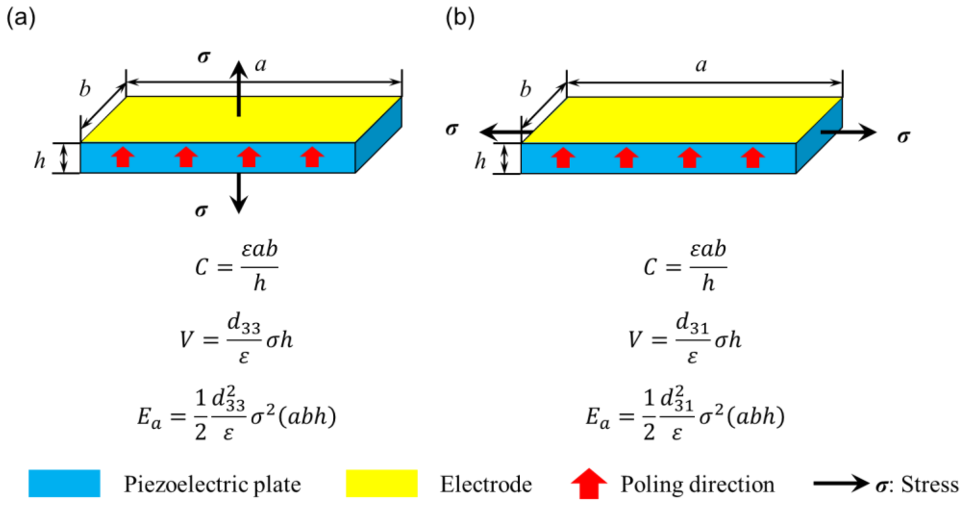

Figure 1-4 Two basic working modes for piezoelectric materials. (a) The 33 mode and (b) the 31 mode.

It is concluded from Eqs. (1-5) and (1-6) that E_a, or the available energy density which is expressed with

$E_a/(abh)$, are affected by the applied stress σ and d_{33}^2/ε (or d_{31}^2/ε) which is defined as the figure of merit (FOM) that is only determined by the material-specific property. Thus, methods to improve E_a are mainly based on two viewpoints: (1) optimizing the device structure for large applied stress and (2) achieving piezoelectric materials with an excellent FOM. The optimization for the device structure always depends on the specific occasions. For instance, the flexible PEH [21-23] can serve as wearable or implantable devices to scavenge mechanical energy from human motions; the frequency-tunable PEH [24-25] can adapt to the vibration with a varied frequency. Above all, this dissertation mainly involves the improvement of the piezoelectric materials, the electrical and electromechanical properties of which are discussed in the later sections as the major point.

1.1.3 Piezoelectric materials for PEH

Up to now, lead-containing piezoelectric materials are still predominant in various piezoelectric applications. Besides the outstanding properties near the MPB composition, it is also found that many elements are easy to solute in Pb-based compositions, which provides more modified solutions with desirable properties. For example, the commercial PZT ceramics [26-27] can exhibit a piezoelectric constant d_{33} as high as 593 pC/N and d_{31} as -274 pC/N, showing a FOM in the 33 mode (FOM_{33}) of 5.4-14.4 TPa^{-1}. Furthermore, the single-crystal ferroelectric relaxor such as $Pb(Zn_{1/3}Nb_{2/3})O_3$–$PbTiO_3$ (PZN-PT) and $Pb(Mg_{1/3}Nb_{2/3})O_3$–$PbTiO_3$ (PMN-PT) developed by Park et al. [28] showed a giant d_{33} over 1000 pC/N and FOM_{33} is 7-8 times larger than that of PZT. However, because lead is harmful to the human bodies, the use of lead-containing items will be restricted more and more in the near future [29-30]. Nevertheless, improving the piezoelectric properties of PZT and clarifying the mechanism of this enhancement are meaningful, which can be used as a guidance to exploiting the excellent lead-free piezoelectric materials.

Except for PZT and BT, many prospective candidates have been reported in recent decades. For example, $(Na_{0.5}Bi_{0.5})TiO_3$ (BNT), which was first discovered by Hagivev et al. [31], exhibits a higher T_c (320°C) but a lower piezoelectric constant (72.9 pC/N) [32] compared with BT. Since then the binary system BNT-BT has been intensively investigated [33-35] for the comprehensive T_c and d_{33} properties. In 2004, Saito et al. [36] prepared a KNN-based derivation by doping $LiTaO_3$ and $LiSbO_3$, achieving d_{33} of 416 pC/N that is comparable to that of PZT ceramics.

Apart from piezoceramics, piezoelectricity was also found in the polymer polyvinylidene fluoride (PVDF) by Kawai [37]. The piezoelectric polymer shows excellent flexibility, indicating a much longer working life span than the peizoceramics have. In spite of a much lower d_{33} (-12 pC/N) than PZT, FOM can reach 4–8 TPa^{-1} due to a low dielectric constant [27], which is suitable for the PEH application.

1.2 Research topics on improving FOM of piezoelectric materials

As mentioned above, FOM is an important criterion to evaluate the output performance of the piezoelectric materials. However, there is seldom straightforward way to achieve a high FOM as the way to improve piezoelectric constant, due to the positive correlation between dielectric and piezoelectric properties.

Figure 1-5 shows a range of FOM_{33} for some common piezoelectric materials. It is shown that FOM_{33} between BT, PZT, KNN and PVDF are comparable to each other, even though the piezoelectric constant of PZT can be one or two orders of magnitude larger than that of PVDF. Of note, FOM_{33} of PZT is still higher than that of PVDF due to a quadratic relationship between FOM_{33} and d_{33}. Thus, it should be admitted that improving the piezoelectric properties does not contradict with improving FOM.

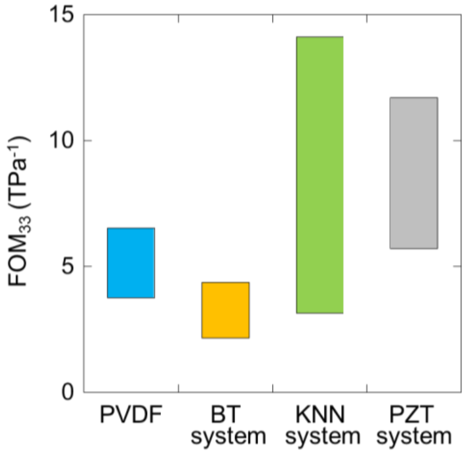

Figure 1-5 FOM_{33} for different piezoelectric materials [38]

In recent years, it has been found that two classes of polarization behavior, as shown in Figure 1-6, are correlated with the piezoelectric response: (1) polarization extension, which changes the magnitude of polarization by ionic displacement and (2) polarization rotation by the movement of domain walls [39]. The latter behavior that greatly affect the piezoelectric response includes the movement of non-180° ferroelectric domains under electric fields (domain wall motion) and the electrical response of the domain wall itself. However, controlling the polarization rotation is not easy because it involves the change of the polarization state, domain structure and even the phase of the ferroelectric materials. Strategies to control the polarization rotation would be obtained by clarifying the related factors and their mechanisms.

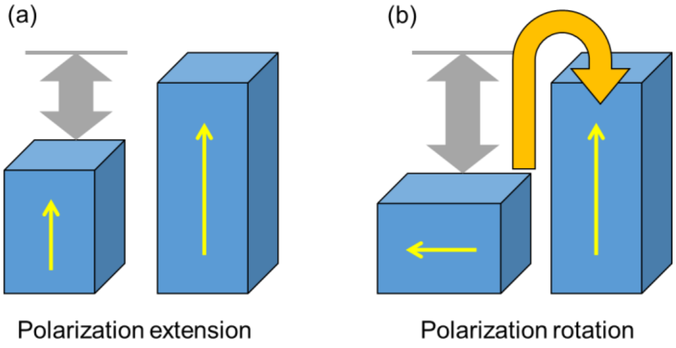

Figure 1-6 Two classes of polarization behavior that relate to the piezoelectric response in ferroelectric materials. (a) Polarization extension and (b) polarization rotation.

1.2.1 Polarization rotation controlled by the MPB composition

It has been reported that giant electric and electromechanical properties exist in the bulk PZT ceramics around the MPB composition. This phenomenon result from the metastable coexistence of tetragonal and rhombohedral phases that can increase the ease of changing the polarization [39]. However, for the PEH application, highly-oriented thin films are widely used and the scenario is quite different from the bulk PZT. It has been reported that the piezoelectric response of the thin films is clearly suppressed by the substrate clamping [40-42]. For example, it has been reported that even though a single-domain thin film, the piezoelectric constant is only about 1/3 of that for the bulk with the same composition. In addition, considering PZT as a reference, MPBs that involve simple phase transition and do not change dramatically with temperature are extremely rare. Thus this strategy may not fit the situation of other materials, which requires to explore other innovative strategies.

1.2.2 Polarization rotation controlled by the external field

Since the MPB composition may not play a dominant role in the ferroelectric thin films, other factors, such as the external field (e.g. electrical, mechanical, thermal, etc.), should be taken into consideration. It is reported that domain wall motion can be driven by an electric field due to the energetically equivalent domains, and a large macroscopic distortion is caused by the sum of different micro distortions from each domain movement [43]. It has also been reported that when an electric field is applied on a ferroelastic material in the non-poling direction, the domain wall itself exhibits giant piezoelectric properties [44]. Of note, the strain induced by the domain wall motion can be considerable large. It is reported that even lead-free materials such as BT can generate an electric field-induced strain of about 1% [45]. In addition, a similar approach is often adopted for ferroelastic materials and magnetostrictive materials, and the reported strain that is associated with domain wall motion can reach as much as 10% [46].

In particular, the electric field-induced strain in the thin films can be larger than in the bulk materials, in which the contribution of this domain wall motion is a one-off phenomenon because there is no driving force returning to the initial state when the voltage is not applied. The analyses focusing on the non-linear behavior of permittivity and piezoelectric constants in the ferroelectric thin films have been conducted since the early 2000s, and it is reported that domain wall motion is remarkably affected by the film thickness [47,48]. In recent years, with the assistance of direct observations by in-situ transmission electron microscopy (TEM) and X-ray diffraction (XRD), it has been found that electrical and electromechanical properties are greatly affected by domain wall motion even in the film with the thickness lower than 100 nm [49,50]. An interesting phenomenon in the film clamped by the substrate is illustrated in Figure 1-7. Due to the stress from the substrate, the domain structure can return to the initial state even though the electric field is canceled [51]. This indicates that it is possible to design a unique domain structure in the thin film by utilizing the substrate constraint, which is supposed to be a negative factor in the conventional viewpoint. Therefore, dealing with the constraint from the substrate would be an important strategy to improve the piezoelectric response in the ferroelectric film.

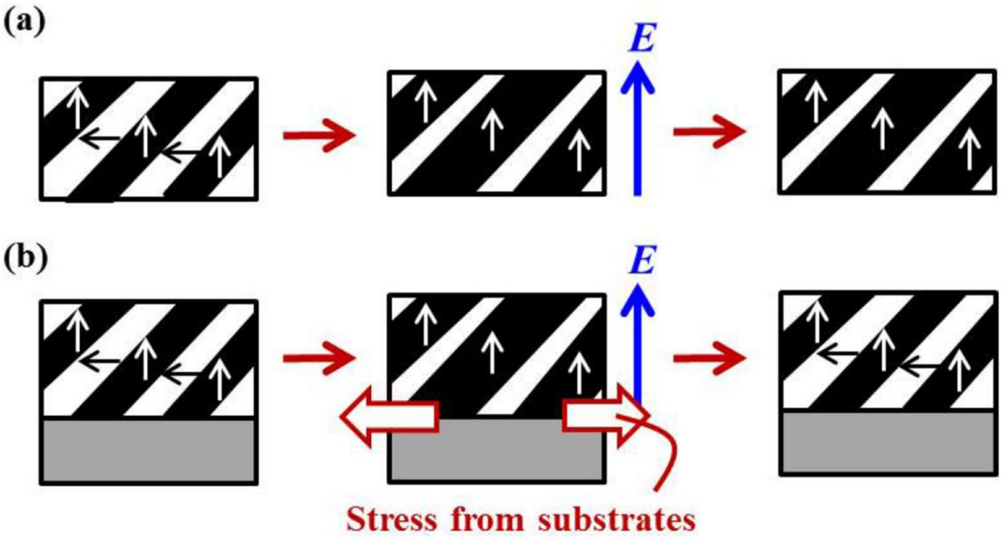

Figure 1-7 Schematics of domain wall motion for ferroelectric (a) bulk ceramics and (b) thin films [51].

In brief, by utilizing the stress induced by the substrates, it is possible to break though the conventional perspectives and achieve the enhanced extrinsic piezoelectric response which originates from the reorientation of polarization driven by an external electric field for the ferroelectric thin films.

1.3 Objective and organization of the dissertation

1.3.1 Objective of this study

As mentioned above, electrical and electromechanical properties of the ferroelectric thin films for PEH can be improved from the perspective of how to deal with the internal stress induced in the films. For one thing, it is possible to eliminate this internal stress to avoid the disadvantage of the substrate clamping and thus achieve the piezoelectric properties comparable to the bulks. For another thing, it is also possible to utilize this internal stress to control the polarization rotation, which can exhibit the similar behavior as the phase transition near MPB for the ferroelectric bulks. In this dissertation, methods and analyses on the improvement of piezoelectric response and output performance for the highly-oriented ferroelectric thin films originate from these two perspectives, and two objectives are established as follows.

(1) Fabricating and evaluating aligned PZT nanorods to improve the output performance, from the perspective of reducing the lateral stress (Chapter 2 – Chapter 4). The finite-element method (FEM) and the experiments conducted by pulsed laser deposition (PLD) will be used to evaluate the FOM of a nanorod array and compare it with that of a dense film. In addition, fabricating PZT nanorod arrays by RF-magnetron sputtering will be attempted for the purpose of commercializing the nanorod-based PEH devices.

(2) Fabricating and evaluating PZT superlattice films to improve the piezoelectric response, from the perspective of utilizing the lateral stress (Chapter 5 – Chapter 6). The dependence of the lateral stress on the polarization state and piezoelectric properties in the PZT films will be first clarified based on the Landau-

Gintzburg-Devonshire (LGD) phenomenological theory. Then theoretically analyzed dependence will be validated by the superlattice films fabricated by PLD.

1.3.2 Organization of the thesis

Figure 1-8 shows the organization of this dissertation. Corresponding to the abovementioned objectives, two types of nanostructure, nanorod arrays and superlattice films, are investigated on their piezoelectric property and output performance and compared with the traditional clamped films. For either nanostructure, theoretical analysis is first conducted to predict the effectiveness the stress strategies, and then fabrication of the nanostructure is followed to validate the theoretical prediction. Contents of each chapter are explained in detail as follows.

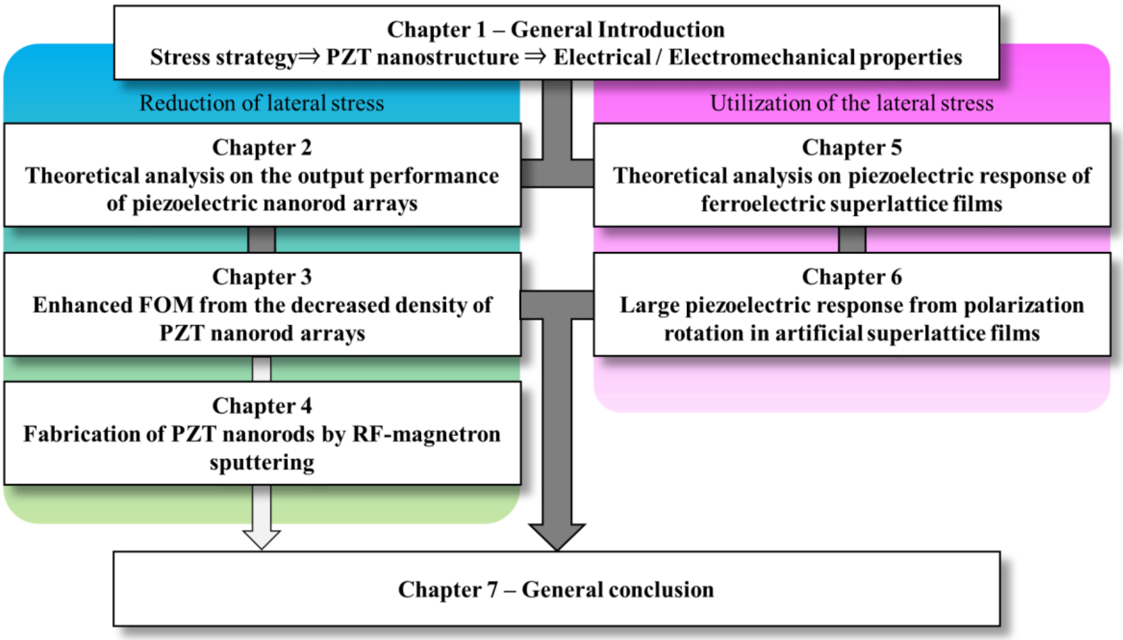

Figure 1-8 Organization of the dissertation

Chapter 2 - Theoretical analysis on the output performance of piezoelectric nanorod arrays

From the perspective of reducing the clamping stress in the film, using the piezoelectric nanorod array would be an effective way to improve the output performance along the out-of-plane direction. In this chapter, a theoretical model of a nanorod array is studied on the output voltage and power, by deducing their expressions from the piezoelectric equations and conducting the FEM simulation in the software *COMSOL Multiphysics*. The study includes (1) effect of the aspect ratio of one nanorod on piezoelectric constant d_{33}, (2) effect of the density of the nanorod array on the output voltage and output power, and (3) comparison with the 33-mode film and the cantilever-based film on their output performance.

Chapter 3 - Enhanced FOM from the decreased density of PZT nanorod arrays

The theoretical study has predicted the enhanced output power of using the nanorod array, due to the increased d_{33} and the decreased density compared with a 33-mode film. It is worth noting that the decreased density achieved in the nanorod array is significant to improve FOM for the PEH application, since there is seldom straightforward way to achieve a high FOM in a piezoelectric film due to the positive correlation between dielectric and piezoelectric properties. However, the effect of the decreased density was scarcely validated by direct experiments. In this chapter, a nanorod array made of tetragonal PZT, with the piezoelectric property similar to a dense film, is fabricated by PLD. For the purpose of distinguishing the significance of the decreased density of the nanorod array from other factors, discussion on (1) the crystallinity and domain structure, (2) dielectric, converse piezoelectric and direct piezoelectric properties, (3) E_a and FOM is conducted in this study.

Chapter 4 - Fabrication of PZT nanorods by RF-magnetron sputtering

For the purpose of commercializing the nanorod-based PEH devices, PZT nanorods are expected to grow in an area up to several cm^2 and thus the fabrication using RF-magnetron sputtering is taken into consideration. Different from the fabrication in PLD, it is difficult to use high pressure for sputtering because the growth rate will be severely reduced by the interaction of the gas molecules. In this chapter, the strategy to grow PZT nanorods without elevating the pressure and the optimal fabrication condition are investigated. Effect of the parameters that are independent of the particle energy, such as Pb concentration in targets, target–substrate distance and deposition time, are first investigated on the crystallinity and growth rate of the PZT samples. Then the effect of temperature and pressure which affect the particle energy are investigated on the crystallinity and possibility of forming nanorods. In particular, it is found that the O_2 partial pressure also plays an important role in forming the nanorod structure, which can be used as a strategy to avoid high pressure sputtering.

Chapter 5 - Theoretical analysis on piezoelectric response of ferroelectric superlattice films

Previous studies have revealed the possibility of improving the piezoelectric response by utilizing the lateral stress. However, it is difficult to validate this possibility in a single-layer film with the thickness over 100 nm, in which a multidomain structure will form due to the local deformation determined by the minimal elastic energy. One of the strategies to achieve a single-domain film is using the superlattice structure with a thin layer thickness. In this chapter, the LGD phenomenological theory is used to clarify the stabilized polarization state in a single-layer film and a superlattice film, with the assumption of single-domain structure in the films. Calculation on (1) the phase diagram of the misfit strain and external electric field, (2) the stabilized polarization state, (3) the dielectric constant ε_{33} and (4) the piezoelectric constant d_{33} and e_{31} in this study, and the piezoelectric property of the superlattice film is evaluated by comparing to the (111)-oriented bulks with the same clamping stress.

Chapter 6 - Large piezoelectric response from polarization rotation in artificial superlattice films

The theoretical analysis has predicted the enhanced piezoelectric property by achieving a desired misfit strain to induce the polarization rotation in a single-domain film. The prediction can be validated by fabricating the superlattice films. In this chapter, (111)-epitaxial artificial superlattice films consisting of $Pb(Zr_{0.4}Ti_{0.6})O_3$ and $Pb(Zr_{0.6}Ti_{0.4})O_3$ were fabricated by PLD, which is in accordance with the theoretical model. The fabricated films with the layer thickness of 24, 12 and 3 nm are characterized on (1) the crystallinity and periodicity of the structure, (2) the domain structure and polarization state, and evaluated on (3) the piezoelectric property with comparison of the theoretical result.

Chapter 7 - General conclusion and future prospective

A general conclusion for all the studies conducted in the dissertation is given in this chapter. In addition, the effectiveness of the strategies employed in this dissertation are presented by positioning the piezoelectric constant and FOM achieved in this study among the recent research progress. Finally, the future prospective based on the present study is summarized in this chapter.

1.4 References

1. G. H. Haertling. Ferroelectric ceramics: history and technology. *Journal of the Ceramic Society of Japan*, **82**, 797–818 (1999).
2. K. Uchino. The development of piezoelectric materials and the new perspective. *In Advanced Piezoelectric Materials*, 1-92. Woodhead Publishing (2017).
3. E. Wainer, and N. Salomon. High titania dielectrics. *Journal of the Electrochemical Society*, **89**, 331–356 (1946).
4. T. Ogawa. On barium titanate ceramics. *Busseiron Kenkyu*, **6**, 1–27 (1947). [in Japanese]
5. B. M. Vul. High and ultrahigh dielectric constant materials. *Elektrichestvo*, 3 (1946). [in Russian].
6. B. Jaffe, R. S. Roth, and S. Marzullo. Piezoelectric properties of lead zirconate–lead titanate solid–solution ceramics. *Journal of Applied Physics*, **25**, 809–810 (1954).
7. B. Jaffe. U.S. Patent No. 2,708,244. Washington, DC: U.S. Patent and Trademark Office (1955).
8. B. Jaffe. Piezoelectric ceramics (Vol. 3). Elsevier (2012).
9. J. Valasek. Piezo-electric and allied phenomena in Rochelle salt. *Physical Review*, **17**, 475 (1921).
10. S. Yin. Integration of epitaxial piezoelectric thin films on silicon. Doctoral dissertation, École Centrale de Lyon (2013).
11. K. Uchino. Ferroelectric devices. CRC press, 1-2 (2009).
12. P. K. Sharma, and P. V. Baredar. Analysis on piezoelectric energy harvesting small scale device–a review. *Journal of King Saud University-Science*, **31**, 869-877 (2019).
13. H. A. Sodano, D. J. Inman, and G. Park. A review of power harvesting from vibration using piezoelectric materials. *Shock and Vibration Digest*, **3**, 197-206 (2004).
14. C. B. Williams, and R. B. Yates. Analysis of a micro-electric generator for microsystems. *Sensors and Actuators A: Physical*, **52**, 8-11 (1996).
15. R. Amirtharajah, and A. P. Chandrakasan. Self-powered signal processing using vibration-based power generation. *IEEE Journal of Solid-State Circuits*, **33**, 687-695 (1998).

16. R. Yeh, S. Hollar, and K. S. Pister. Single mask, large force, and large displacement electrostatic linear inchworm motors. *Journal of Microelectromechanical Systems*, **11**, 330-336 (2002).
17. S. S. Lee, and R. M. White. Self-excited piezoelectric cantilever oscillators. *Sensors and Actuators A: physical*, **52**, 41-45 (1996).
18. S. Roundy, P. K. Wright, and J. Rabaey. A study of low level vibrations as a power source for wireless sensor nodes. *Computer Communications*, **26**, 1131-1144 (2003).
19. K. Uchino, and T. Ishii. Mechanical damper using piezoelectric ceramics. *Journal of the Ceramic Society of Japan*, **96**, 863-867 (1988).
20. G. A. Lesieutre. Vibration damping and control using shunted piezoelectric materials. *Shock and Vibration Digest*, **30**, 187-195 (1998).
21. Y. Qi, J. Kim, T. D. Nguyen, B. Lisko, P. K. Purohit, and M. C. McAlpine. Enhanced piezoelectricity and stretchability in energy harvesting devices fabricated from buckled PZT ribbons. *Nano letters,* **11**, 1331-1336 (2011).
22. H. Chen, H. Wang, J. Wu, F. Wang, T. Zhang, Y. Wang, D. Liu, S. Li, R. V. Penty, and I. H. White. Flexible optoelectronic devices based on metal halide perovskites. *Nano Research*, **13**, 1997–2018 (2020).
23. F. Bouhjar, L. Derbali, and B. Marí. High performance novel flexible perovskite solar cell based on a low-cost-processed ZnO: Co electron transport layer. *Nano Research*, **13**, 2546-2555 (2020).
24. V. R. Challa, M. G. Prasad, Y. Shi and F. T. Fisher. A vibration energy harvesting device with bidirectional resonance frequency tenability. *Smart Materials and Structures,* **17**, 015035 (2008).
25. V. R. Challa, M. G. Prasad, and F. T. Fisher. Towards an autonomous self-tuning vibration energy harvesting device for wireless sensor network applications. *Smart Materials and Structures*, **20**, 025004 (2011).
26. G. Hayward, J. Bennett, and R. Hamilton. A theoretical study on the influence of some constituent material properties on the behavior of 1-3 connectivity composite transducers. *The Journal of the Acoustical Society of America*, **98**, 2187-2196 (1995).
27. C. R. Bowen, H. A. Kim, P. M. Weaver, and S. Dunn. Piezoelectric and ferroelectric materials and structures for energy harvesting applications. *Energy & Environmental Science*, **7**, 25-44 (2014).
28. S. E. Park, and T. R. Shrout. Ultrahigh strain and piezoelectric behavior in relaxor based ferroelectric single crystals. *Journal of Applied Physics*, **82**, 1804-1811 (1997).
29. J. Wu. Advances in lead-free piezoelectric materials. Singapore: Springer (2018).
30. A. Safari and M. Abazari. Lead-free piezoelectric ceramics and thin films. *IEEE Transactions on Ultrasonics, Ferroelectrics, and Frequency Control,* **57**, 2165- 2176 (2010).
31. M. S. Hagiyev, I. H. Ismailzade, and A. K. Abiyev. Pyroelectric properties of $(Na_{1/2}Bi_{1/2})TiO_3$ ceramics. *Ferroelectrics*, **56,** 215–217 (1984).
32. Y. Hiruma, H. Nagata, and T. Takenaka. Thermal depoling process and piezoelectric properties of bismuth sodium titanate ceramics. *Journal of Applied Physics,* **105**, 084112 (2009).

33. T. Takenaka, K. Maruyama, and K. Sakata. $(Bi_{1/2}Na_{1/2})TiO_3$-$BaTiO_3$ system for lead-free piezoelectric ceramics. *Japanese Journal of Applied Physics*, **30**, 2236–2239 (1991).
34. Q. Zhang, Y. Zhang, F. Wang, Y. Wang, D. Lin, X. Zhao, H. Luo, W. Ge, and D. Viehland. Enhanced piezoelectric and ferroelectric properties in Mn-doped $Na_{0.5}Bi_{0.5}TiO_3$–$BaTiO_3$ single crystals. *Applied Physics Letters*, **95**, 102904 (2009).
35. P. Fu, Z. Xu, R. Chu, W. Li, G. Zang, and J. Hao. Piezoelectric, ferroelectric and dielectric properties of Nd_2O_3-doped $(Bi_{0.5}Na_{0.5})_{0.94}Ba_{0.06}TiO_3$ lead-free ceramics. *Materials Science and Engineering: B*, **167**, 161-166 (2010).
36. Y. Saito, H. Takao, T. Tani, T. Nonoyama, K. Takatori, T. Homma, T. Nagaya, and M. Nakamura. Lead-free piezoceramics. *Nature*, **432**, 84-87 (2004).
37. H. Kawai. The piezoelectricity of poly(vinylidene fluoride). *Japanese Journal of Applied Physics*, **8**, 9751969 (1969).
38. J. Song, and J. Wang. Ferroelectric materials for vibrational energy harvesting. *Science China Technological Sciences*, **59**, 1012-1022 (2016).
39. D. J. Kim, J. P. Maria, A. I. Kingon, and S. K. Streiffer. Evaluation of intrinsic and extrinsic contributions to the piezoelectric properties of $Pb(Zr_{1-X}T_X)O_3$ thin films as a function of composition. *Journal of Applied Physics*, **93**, 5568-5575 (2003).
40. C. M. Foster, G. R. Bai, R. Csencsits, J. Vetrone, R. Jammy, L. A. Wills, E. Carr and J. Amano. Single-crystal $Pb(Zr_xTi_{1-x})O_3$ thin films prepared by metal-organic chemical vapor deposition: Systematic compositional variation of electronic and optical properties. *Journal of Applied Physics*, **81**, 2349-2357 (1997).
41. K. Nagashima, M. Aratani, H. Funakubo. Orientation dependence of ferroelectricity of epitaxially grown $Pb(Zr_xTi_{1-x})O_3$ thin films prepared by metalorganic chemical vapor deposition. *Journal of Applied Physics*, **89**, 4517-4522 (2001).
42. M. J. Haun. Thermodynamic theory of the lead zirconate titianate solid solution system. Ph.D. thesis, The Pennsylvania State University (1988).
43. J. Shieh, J. H. Yeh, Y. C. Shu, and J. H. Yen. Operation of multiple 90 switching systems in barium titanate single crystals under electromechanical loading. *Applied Physics Letters*, **91**, 062901 (2007).
44. P. Ondrejkovic, P. Marton, M. Guennou, N. Setter and J. Hlinka. Piezoelectric properties of twinned ferroelectric perovskites with head-to-head and tail-to-tail domain walls. *Physical Review B*, **88**, 024114 (2013).
45. Y. W. Li, and F. X. Li. Ultrahigh actuation strains in $BaTiO_3$ and $Pb(Mn_{1/3}Nb_{2/3})O_3$-$PbTiO_3$ single crystals via reversible electromechanical domain switching. *Applied Physics Letters*, **102**, 152905 (2013).
46. A. Sozinov, A. A. Likhachev, N. Lanska, and K. Ullakko. Giant magnetic-field-induced strain in NiMnGa seven-layered martensitic phase. *Applied Physics Letters*, **80**, 1746-1748 (2002).
47. A. Kholkin, Non-linear piezoelectric response in lead zirconate-titanate (PZT) films. *Ferroelectrics*, **238**,

235-243 (2000).

48. M. B. Kelman, P. C. McIntyre, B. C. Hendrix, S. M. Bilodeau, and J. F. Roeder. Effect of applied mechanical strain on the ferroelectric and dielectric properties of $Pb(Zr_{0.35}Ti_{0.65})O_3$ thin films. *Journal of Applied Physics*, **93**, 9231-9236 (2003).
49. Y. Ehara, S. Yasui, J. Nagata, D. Kan, V. Anbusathaiah, T. Yamada, O. Sakata, H. Funakubo, and V. Nagarajan. Ultrafast switching of ferroelastic nanodomains in bilayered ferroelectric thin films. *Applied Physics Letters*, **99**, 182906 (2011).
50. P. Gao, J. Britson, C. T. Nelson, J. R. Jokisaari, C. Duan, M. Trassin, S. H. Baek, H. Guo, L. Li, Y. Wang, Y. H. Chu, A. M. Minor, C. B. Eom, R. Ramesh, L. Q. Chen, and X. Pan. Ferroelastic domain switching dynamics under electrical and mechanical excitations. *Nature Communications*, **5**, 1-8 (2014).
51. K. S. Lee, Y. K. Kim, S. Baik, J. Kimand I. S. Jung. In situ observation of ferroelectric 90-domain switching in epitaxial $Pb(Zr,Ti)O_3$ thin films by synchrotron x-ray diffraction. *Applied Physics Letters*, **79**, 2444-2446 (2001).

Chapter 2 - Theoretical analysis on the output performance of piezoelectric nanorod arrays

2.1 Introduction

From the perspective of reducing the clamping stress in the film, using the piezoelectric nanorod array [52-55] would be an effective way to improve the output performance along the out-of-plane direction. In this chapter, a theoretical model of a nanorod array is studied on the output voltage and power, by deducing their expressions from the piezoelectric equations and conducting the FEM simulation in the software *COMSOL Multiphysics*. The study includes (1) effect of the aspect ratio of one nanorod on piezoelectric constant d_{33}, (2) effect of the density of the nanorod array on the output voltage and output power, and (3) comparison with the 33-mode film and the cantilever-based film on their output performance.

2.2 Theoretical models

2.2.1 Direct d_{33} of a clamped film

To evaluate the output performance of a nanorod array, comparison with the film clamped by the substrate will be frequently needed in this study. For the theoretical model of a nanorod, one assumes that the lateral stress is completely eliminated, and thus the nanorod will exhibit the same deformation as a bulk material, for which the theoretical model can be easily referred from the previous studies. In contrast, the deformation of a film that is fully clamped by the substrate is more complicated and how the deformation affects the piezoelectric property, especially in the direct mode, needs to be clarified.

Figure 2-1 shows two common stress states in a piezoelectric unit. Here the coordinate system (*1,2,3*) corresponds to the crystallographic frame of the piezoelectrics. For a piezoelectric bulk, there is nothing to limit the deformation and thus the material tends to shrink in the transverse direction (here refers to the *1,2*-direction) while expands along with the tensile stress (here refers to the *3*-direction), as shown in Figure 2-1(a). For a piezoelectric thin film, in most occasions, the transverse deformation is prevented by the substrate and thus the deformation in the *3*-direction becomes small, as shown in Figure 2-1(b). These two stress state can be approximately described as

$$\sigma_1 = \sigma_2 = 0,\ \sigma_3 \neq 0 \text{ for a bulk,} \tag{2-1}$$

$$u_1 = u_2 = 0,\ \sigma_3 \neq 0 \text{ for a fully clamped film,} \tag{2-2}$$

where u and σ stand for the strain and the stress, respectively.

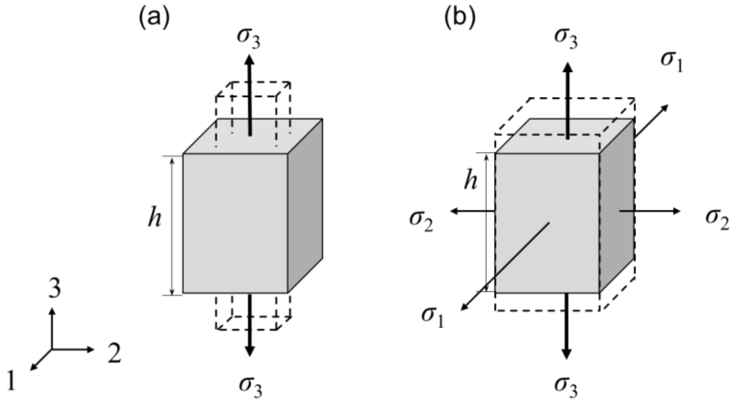

Figure 2-1 Deformation of a piezoelectric unit with different stress states. (a) Transverse deformation is allowed for a bulk. (b) Transverse deformation is not allowed for a clamped film.

Equation (2-3) gives the general piezoelectric equation in a tensor form,

$$\begin{cases} \boldsymbol{u} = \boldsymbol{s}^E\boldsymbol{\sigma} + \boldsymbol{d}_t \cdot \boldsymbol{E} \\ \boldsymbol{D} = \boldsymbol{d} \cdot \boldsymbol{\sigma} + \boldsymbol{\varepsilon}^\sigma \boldsymbol{E} \end{cases} \tag{2-3}$$

where, the upper equation is used for describing the converse piezoelectric effect and the lower one is for the direct piezoelectric effect. $\boldsymbol{D}$ and $\boldsymbol{E}$ are vectors which represents the dielectric displacement and the electric field, respectively. $\boldsymbol{u}$ and $\boldsymbol{\sigma}$ stands for the strain and the stress, respectively, in the form of the second-order tensor in Voigt notation. $\boldsymbol{\varepsilon}^\sigma$ is also a second-order tensor, representing the dielectric constant under constant stress. $\boldsymbol{d}$ is the piezoelectric coefficient in the form of a third-order tensor and $\boldsymbol{d}_t$ is the transpose of $\boldsymbol{d}$. $\boldsymbol{s}^E$ is the elastic compliance constant under constant electric field, and known as a fourth-order tensor. In this study, the differences caused by the boundary conditions (denoted by the superscript E or σ) of measuring $\boldsymbol{s}$ and $\boldsymbol{\varepsilon}$ are neglected. With respect to the clamped film shown in Figure 2-1(b), the following equations are obtained from Eq. (2-3).

$$u_1 = (s_{11} + s_{12})\sigma_1 + s_{13}\sigma_3 + d_{31}E_3 \tag{2-4}$$

$$u_3 = (s_{31} + s_{32})\sigma_1 + s_{33}\sigma_3 + d_{33}E_3 \tag{2-5}$$

$$D_3 = 2d_{31}\sigma_1 + d_{33}\sigma_3 + \varepsilon_{33}E_3 \tag{2-6}$$

where one assumes that the physical properties in *1*- and *2*-direction are isotropic. The piezoelectric constant d_{33} can be figured out with the mechanical boundary condition given by Eq. (2-2) as well as the open-circuit condition, giving $D_3 = 0$. Then solving the simultaneous Eqs. (2-4) and (2-6), one obtains

$$\begin{cases} \sigma_1 = \frac{-d_{31}d_{33}\sigma_3 + s_{13}\varepsilon_{33}\sigma_3}{2d_{31}^2 - (s_{11}+s_{12})\varepsilon_{33}} \\ E_3 = \frac{d_{33}(s_{11}+s_{12})\sigma_3 - 2d_{31}s_{13}\sigma_3}{2d_{31}^2 - (s_{11}+s_{12})\varepsilon_{33}} \end{cases} \tag{2-7}$$

To discuss the clamped film as the way to deal with the bulk material, the apparent piezoelectric constant $d_{33,\mathrm{f}}$, redefined from definition of the bulk d_{33}, is frequently used. For the direct piezoelectric mode, $d_{33,\mathrm{f}}$ is given by

$$d_{33,\mathrm{f}}^{(\mathrm{di})} = -\frac{\varepsilon_{33}E_3}{\sigma_3} \tag{2-8}$$

Substituting Eq. (2-8) with the solution given in Eq. (2-7), $d_{33,\mathrm{f}}^{(di)}$ is expressed as

$$d_{33,\mathrm{f}}^{(\mathrm{di})} = d_{33} - 2d_{31}\frac{d_{31}d_{33} - \varepsilon_{33}s_{13}}{2d_{31}^{2} - \varepsilon_{33}(s_{11} + s_{12})} \tag{2-9}$$

From the above expression, it is found that $d_{33,\mathrm{f}}^{(di)}$ is not only determined by the piezoelectric property but also by the dielectric property, which is different from the apparent piezoelectric constant in the converse mode. It is difficult to conclude from this complicated expression whether $d_{33,\mathrm{f}}^{(\mathrm{di})}$ is suppressed by the clamping effect when compared with the bulk d_{33}.

2.2.2 Output performance of the nanorod array

A model of a nanorod array in connection with an external resistance R and its equivalent circuit are shown in Figure 2-2. For the model shown in Figure 2-2(a), a sinusoidal vibration expressed by $F = F_{\mathrm{m}}\sin(\omega t)$, where F_{m} is the maximum force, ω the angular frequency of the vibration and t the time, is applied uniformly along the axial direction of the nanorods. Here the axial direction is defined as the *3*-direction and thus the operation mode of the nanorod array is known as the 33 mode. Each of the nanorod units is treated as a cuboid with the height of h and the width of b. The total contact area between the nanorod array and the substrate, occupied by both nanorods and air gaps, is denoted with A, and the ratio of the nanorod part to the total is denoted with x_{NR}. The bottom surface of the nanorods is fixed (total displacement is always zero) and the top surface is free (without clamping). Considering the low working frequency of the PEH devices, the dielectric loss is neglected and then the piezoelectric layer can be treated as a parallel plate capacitor with the reactance of X_{c}. Then the mechanical and electrical boundary conditions of the nanorod array are related via the piezoelectric equation from Eq. (2-3).

$$D_3 = d_{33}\sigma_3 + \varepsilon_{33}E_3 \tag{2-10}$$

here, $\sigma_3 = F/(Ax_{NR})$ according to the above definitions. The current in the circuit, I_{R}, and the voltage applied on the resistance, V_{R}, are expressed as shown in Figure 2-2(b).

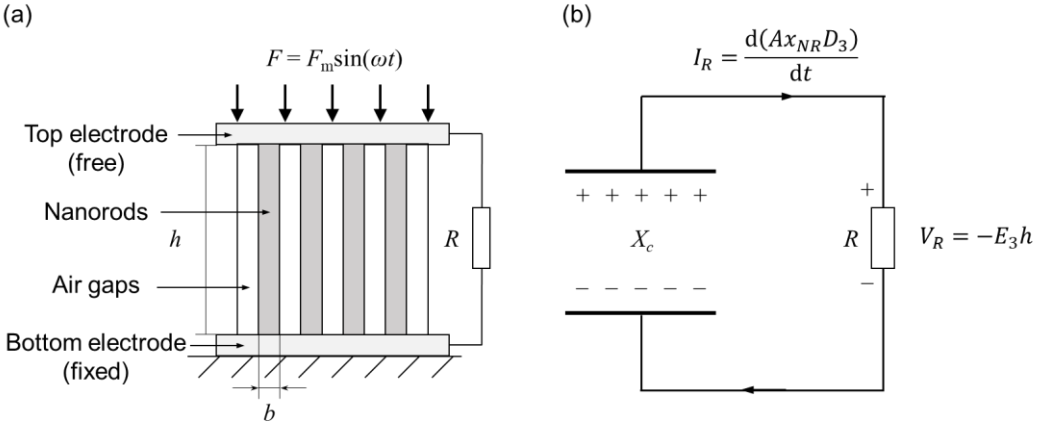

Figure 2-2 (a) Schematic configuration of a model of a nanorod array connected to the resistance R. (b) Equivalent circuit of the model.

The open-circuit voltage V_{open} can be deduced from Eq. (2-10) at $D_3 = 0$. Substituting σ_3 and E_3 with F

and V_{open}, one obtains

$$V_{\text{open}} = -E_3 h = \frac{d_{33} F_m h}{\varepsilon_{33} x_{NR} A} \sin \omega t \tag{2-11}$$

Similarly, the short-circuit current I_{short} at $E_3 = 0$ with the substitution of D_3 is expressed as

$$I_{\text{short}} = A x_{NR} \frac{\mathrm{d}D_3}{\mathrm{d}t} = \omega d_{33} F_m \cos \omega t \tag{2-12}$$

With respect to the nanorod array connected with an external resistance, current and voltage are not both zero. The relationship can be deduced by differentiating Eq. (2-10) with respect to the time t as

$$\frac{\mathrm{d}D_3}{\mathrm{d}t} = d_{33} \frac{\mathrm{d}\sigma_3}{\mathrm{d}t} + \varepsilon_{33} \frac{\mathrm{d}E_3}{\mathrm{d}t} \tag{2-13}$$

Substituting D_3, σ_3 and E_3 with the above expressions, Eq. (2-13) becomes

$$I_R = d_{33} \frac{\mathrm{d}F}{\mathrm{d}t} - \frac{\varepsilon_{33} x_{NR} A}{h} \frac{\mathrm{d}V_R}{\mathrm{d}t} \tag{2-14}$$

where V_R is known as RI_R according to the Ohm’s law. The equivalent capacitance C_{NR} of the nanorods is expressed as

$$C_{NR} = \frac{\varepsilon_{33}(A x_{NR})}{h} = \frac{1}{\omega X_c} \tag{2-15}$$

then Eq. (2-14) becomes

$$I_R = d_{33} \frac{\mathrm{d}F}{\mathrm{d}t} - \frac{R}{\omega X_C} \frac{\mathrm{d}I_R}{\mathrm{d}t} \tag{2-16}$$

which is a partial differential equation. Here the initial current is assumed to be zero at $t = 0$. Then the solution for Eq. (2-16) is

$$I_R = \frac{d_{33} F_m \omega}{\frac{R^2}{X_C^2} + 1} \left[-\frac{R}{X_C} \sin \omega t + \cos \omega t - \exp\left(-\frac{\omega t}{\frac{R}{X_C}} \right) \right] \tag{2-17}$$

Assuming that the PEH device operates for a sufficiently long time, the exponent term tends to be zero and then Eq. (2-17) becomes

$$I_R = \frac{d_{33} F_m \omega}{\sqrt{\frac{R^2}{X_C^2} + 1}} \sin(\omega t + \varphi) \tag{2-18}$$

where

$$\tan \varphi = \frac{\mathrm{X_C}}{R} \tag{2-19}$$

The effective current I_{eff}, also known as the root mean square (RMS) value of I_R, is

$$I_{\text{eff}} = \left(\frac{\omega}{2\pi} \int_0^{\frac{2\pi}{\omega}} I_R^2 dt \right)^{\frac{1}{2}} = \frac{d_{33} F_m \omega}{\sqrt{2\left(\frac{R^2}{X_C^2} + 1 \right)}} \tag{2-20}$$

and thus the output power P_{out} is

$$P_{\text{out}} = I_{\text{eff}}^2 R = \frac{(d_{33} F_m \omega)^2}{2\left(\frac{R^2}{X_C^2}+1\right)} R \le \frac{(d_{33} F_m \omega)^2}{4} X_C \tag{2-21}$$

The maximum P_{out}, denoted with P_{m}, is obtained when and only when $R = X_{\text{C}}$ at which R is known as the optimal resistance R_{opt}.

The above equations for the output performance can also be applied to a clamped film operated in the 33 mode, when $x_{\text{NR}} = 1$ and $d_{33} = d_{33,\text{f}}^{(\text{di})}$. Here one gives the ratio of the nanorod array to the film on V_{open} and P_{m} as follows, which will be further discussed in the next section.

$$\frac{V_{\text{open,NR}}}{V_{\text{open,f}}} = \frac{d_{33}}{d_{33,\text{f}}^{(\text{di})}} (x_{NR})^{-1} \tag{2-22}$$

$$\frac{P_{\text{m,NR}}}{P_{\text{m,f}}} = \left(\frac{d_{33}}{d_{33,\text{f}}^{(\text{di})}}\right)^2 (x_{NR})^{-1} \tag{2-23}$$

where “NR” and “f” in the subscript denote the case of a nanorod array and the case of a clamped film, respectively.

2.2.3 Theoretical models analyzed via the finite-element method

The output performance based on the abovementioned equations is only applied to some simple and ideal piezoelectric models. For the more complicated models, such as a partially clamped film or a 31-mode (cantilever-based) film, the finite-element method (FEM) conducted by the simulation software *COMSOL Multiphysics* is used to evaluate their output performance. Figure 2-3 shows the simulation procedures in *COMSOL*, taking the 31-mode PEH device as an example. The output performance of the 31-mode PEH device is also used to compare with that of the nanorod array from the perspective of the practical applications.

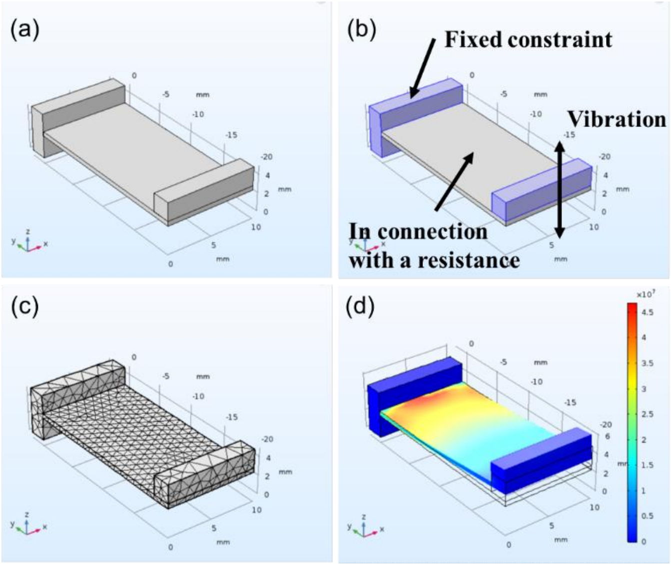

Figure 2-3 Simulation procedures in *COMSOL*. (a) Model building. (b) Setting boundary conditions. (c) Meshing. (d) Computing and result display.

In this study, $Pb(Zr_{0.35}Ti_{0.65})O_3$ is selected as the piezoelectric layer for comparison with experimental results. The dielectric and piezoelectric constants are based on the average of those properties of

$Pb(Zr_{0.3}Ti_{0.7})O_3$ and $Pb(Zr_{0.4}Ti_{0.6})O_3$, which are obtained from the study of Haun *et al.* [56]. The elastic compliance constants of a PZT ceramic in the material library of *COMSOL* are used. Steel is selected as the material of the substrate and seismic mass for the built models. The detailed values are listed in Table 2-1.

Table 2-1 Properties of materials used in simulation. [51]

	Property	Notation	Value
Piezoelectric layers, made of $Pb(Zr_{0.35}Ti_{0.65})O_3$	Piezoelectric constants (pC/N)	d_{33}	133
		d_{31}	-45.8
	Elastic compliance constants (10^{-12} Pa^{-1})	s_{11}	16.4
		s_{12}	-5.74
		s_{13}	-7.22
	Relative permittivity	ε	155
	Density (g • cm^{-3})	ρ	7.75
Substrates and masses, made of steel	Young's module (GPa)	Y_{sub}	200
	Poisson ratio	v	0.3
	Density (g • cm^{-3})	ρ_{sub}	10

2.3 Results and discussion

2.3.1 Effect of the aspect ratio

The aspect ratio determines the clamping state of the piezoelectric unit. It is known that the small aspect ratio will lead to a large proportion of the clamped area in the piezoelectric unit. Figure 2-4 shows a FEM model of a cuboid piezoelectric unit and the deformation depended on the aspect ratio. The boundary condition is illustrated in Figure 2-4(a). As mentioned above, the total displacement of the bottom surface is fixed to zero and the top surface is free of clamping. The aspect ratio is defined as h/b, where h (i.e. the thickness of the film or the height of the nanorods) is set to 1 μm and thus h/b only varies with the width b. A sinusoidal vibration with the stress amplitude of 1 MPa and the frequency of 100 Hz is applied along the out-of-plane direction, which can be treated as an off-resonant vibration since the nature frequency of the one-side-fixed unit is over 1 MHz. In addition to the deformation, the total lateral stress, expressed by $\sqrt{\sigma_1^2+\sigma_2^2}$ and represented by the color map is shown in Figure 2-4(b) and (c). Here a unit of $h/b = 0.05$ is exemplified for a case of a film and $h/b = 5$ for a rod. It can be concluded from the color map of two units that a low lateral stress is induced in the unit with a large h/b, indicating the rod will deform more easily and exhibit larger piezoelectric constant than the film.

With the model in Figure 2-4, effect of h/b on the apparent piezoelectric constant of the unit can be clarified by calculating the open-circuit voltage, as illustrated by Figure 2-5. The ordinate is the voltage ratio as described in Eq. (2-22). When h/b is smaller than 0.001 or larger than 10, the voltage is almost constant, which can be assumed as a fully clamped film or a free bulk, respectively. For $0.001 < h/b < 10$,

$V_{\text{open,NR}}/V_{\text{open,f}}$ increases gradually as h/b becomes large, indicating a partially clamped piezoelectric unit. Since σ_3 and h are set to be constant and the effect of the mechanical boundary condition on ε_{33} is neglected, the change of the open-circuit voltage is due to the change of apparent d_{33} according to the equation shown in Figure 2-5. Therefore, it is indicated that d_{33} can be increased by 33% if one employs the nanorod array instead of a dense film in the 33 mode. Of note, an experimental dependence of the aspect ratio on d_{33} was obtained by Barzegar et al. [57], who observed a similar enhancement of d_{33} in the PZT ceramics with various aspect ratios. Although the material properties and size are different between our simulation and their experiment, the similar dependence supports our scenario.

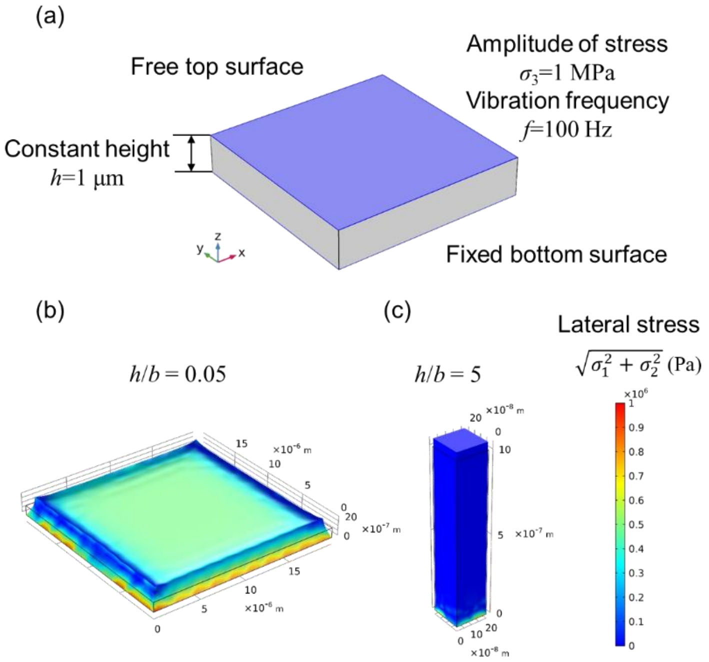

Figure 2-4 Effect of the aspect ratio on the deformation and induced lateral stress. (a) The model in FEM with the related boundary conditions. (b) The result for a film with h/b = 0.05. (c) The result for a rod with h/b = 5

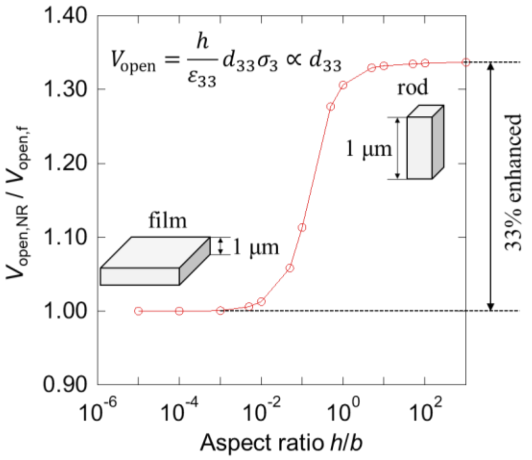

Figure 2-5 Effect of the aspect ratio on the open-circuit output voltage.

For the fully clamped film with the condition given in Eq. (2-2), $d_{33,\mathrm{f}}^{(\mathrm{di})}$ can be figured out with Eq. (2-9). Using the parameters shown Table 2-1, $d_{33,\mathrm{f}}^{(\mathrm{di})}$ is estimated to 99.5 pC/N and the ratio of d_{33} (= 133 pC/N) to $d_{33,\mathrm{f}}^{(\mathrm{di})}$ is 34%, which basically agrees with the enhancement shown in Figure 2-5. For further discussion, the converse clamped piezoelectric constant $d_{33,\mathrm{f}}^{(\mathrm{con})}$ can be figured out to 71 pm/V by the following equation [55].

$$d_{33,\mathrm{f}}^{(\mathrm{con})} = d_{33} - 2d_{31}\frac{s_{13}}{s_{11}+s_{12}} \tag{2-24}$$

It is found that the direct $d_{33,\mathrm{f}}$ is larger than the converse $d_{33,\mathrm{f}}$ but still smaller than the bulk d_{33}. Comparison of theses d_{33} constants can be further clarified by investigating PZT with different Zr/Ti ratio, as shown in Figure 2-6. The piezoelectric constants are obtained in Ref. [58] and The elastic compliance coefficients s_{11}, s_{12}, s_{13} are assumed to be constant and have the values given in Table 2-1. All the compositions are calculated in the tetragonal phase. It is shown that except for $\mathrm{Pb(Zr_{0.5}Ti_{0.5})O_3}$ that is near the MPB composition, the direct $d_{33,\mathrm{f}}$ is smaller than the bulk d_{33} but larger than the converse $d_{33,\mathrm{f}}$. Therefore, employing the nanorod structure to enhance the piezoelectric response is meaningful for both direct and converse situations.

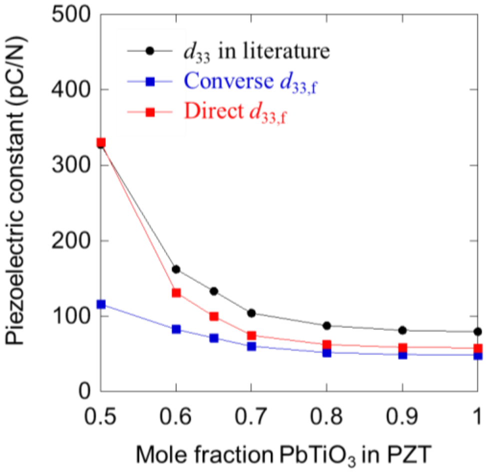

Figure 2-6 comparison of the bulk d_{33}, the converse $d_{33,\mathrm{f}}$ and the direct $d_{33,\mathrm{f}}$ for PZT with different Zr/Ti ratios.

2.3.2 Effect of the density of the nanorod array

In the above section, the enhanced piezoelectric response has been clarified by enlarging h/b without changing the applied stress. In more cases, the force applied on a PEH device is given and thus the applied stress will change with the density of the nanorod array, specifically, the contact area between the piezoelectric layer and the substrate. The effect of the density of the nanorod array on the output performance is studied with the model shown in Figure 2-7(a). The boundary conditions of the surfaces of each nanorods are the same as used in Figure 2-4(a). A vibration force is applied along the z-direction, with the amplitude of F_m = 25 μN and a frequency of 50 Hz which is far from the resonant frequency. The aspect ratio of h/b = 10 is employed to all the nanorods, and the dimension of the nanorod-based device is limited to 10 × 10 × 1 μm for shortening the computation time. According to the experimental results found in the PZT nanorods fabricated by PLD [62–64], it is easy to achieve a nanorod with an aspect ratio larger than 5, and thus the unclamped d_{33} (= 155 pC/N) is used for the simulated nanorods.

The maximum output voltage is calculated with the open-circuit condition and the maximum output power is evaluated with the connection to the optimal resistance R_{opt}. For the latter condition, generated current I_{R} depended on time is calculated by FEM as shown in Figure 2-7(b). It is shown that the dependence is in accordance with the expression of I_{R} in Eqs. (2-17) and (2-18). The amplitude of I_{R} is suppressed at the beginning due to the exponent term, and the wave has a phase shift of φ compared to the wave of the vibration F.

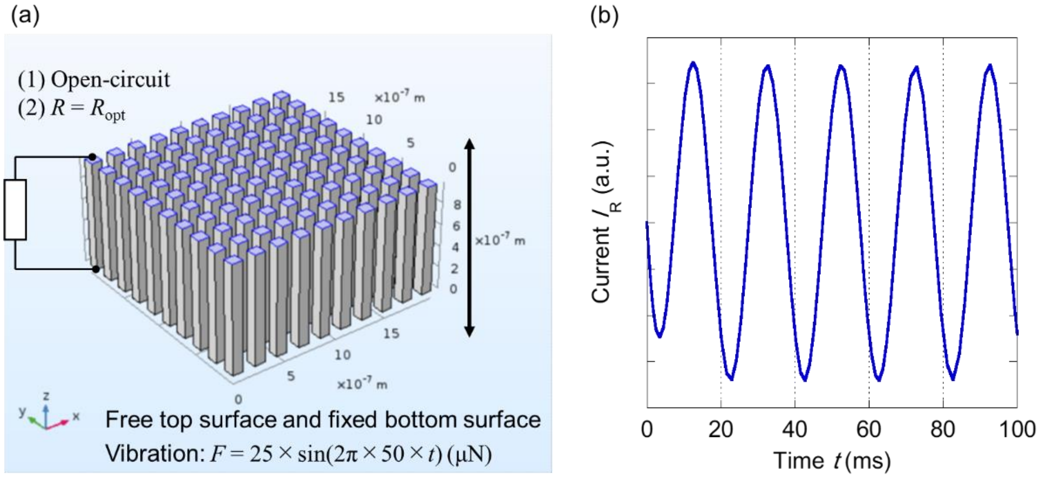

Figure 2-7 (a) Model of the nanorod array used for studying the effect of the density on the output performance. (b) generated current I_{R} depended on time by FEM with the connection to R_{opt}.

Figure 2-8 shows the theoretical open-circuit voltage and output power density depended on the density of the nanorod array. Here the density of the nanorod array is denoted by x_{NR}, the volume ratio of the nanorod part to the total device. For $x_{NR} = 1$, the piezoelectric layer is assumed as a dense film and $d_{33,\mathrm{f}}^{(\mathrm{di})}$ (=99.5 pC/N) is employed to this case. In Figure 2-8(a), the amplitude of V_{open}, denoted by V_{m}, is used as the ordinate. The black dots represent the result of the FEM simulation, and the red line and the blue line stand for the results calculated by Eq. (2-11) with the unclamped d_{33} and $d_{33,\mathrm{f}}^{(\mathrm{di})}$, respectively. It is clear to see that V_{m} increases as x_{NR} decreases, and a discontinuous change occurs from the film to the nanorod structure in the FEM result, indicating the enhancement of d_{33} due to the change of the aspect ratio. Comparing with the difference between the red line and the blue line, caused by the different aspect ratio, it is shown that x_{NR} also plays an important role in increasing the open-circuit voltage. In addition, the FEM result for the nanorod array agrees well with the result calculated by Eq. (2-11) with the unclamped d_{33}. Figure 2-8(b) shows the FEM simulation of the maximum power density depended on x_{NR}. Here the power density is defined as the output power divided by the volume of the piezoelectric layer. The dependence with x_{NR} is in accordance with that of the open-circuit voltage in Figure 2-8(a). This dependence can also be clarified with Eqs. (2-22) and (2-23), which is also shown in the figures. It is known that both voltage and power are inversely proportional to the density of $x_{\mathrm{NR}} < 1$, and the discontinuous change of the power at $x_{\mathrm{NR}} = 1$ is larger due to the larger coefficient of proportionality.

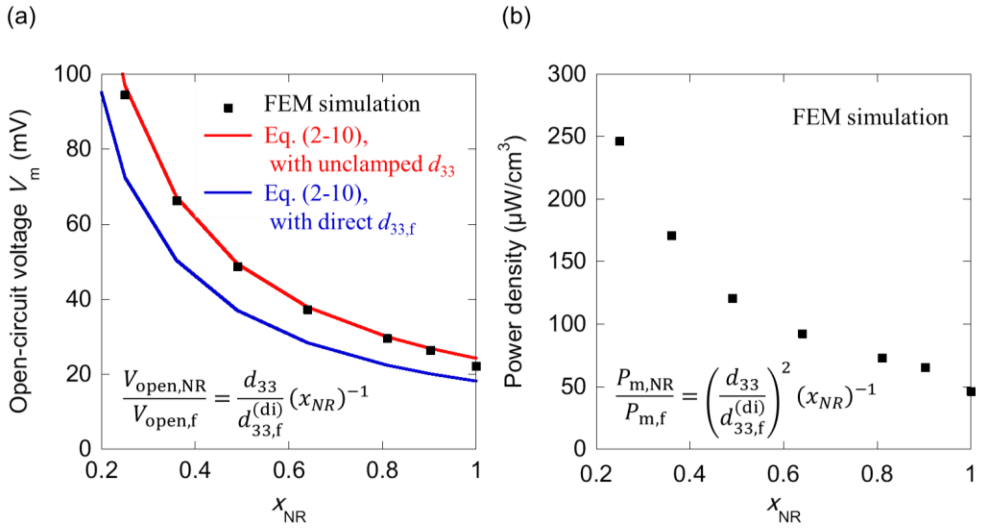

Figure 2-8 Dependence of the (a) output voltage and (b) power on the area ratio of the nanorods.

Therefore, the nanorod structure is proved to be an effective way of improving the output power of the PEH device because of the enhanced d_{33} (thus FOM) and stress of the piezoelectric materials. Since d_{33} is known to be always higher than d_{31}, the d_{33} working mode will be more efficient as long as the generated stress is comparable to that of the 31 mode used in a cantilever structure.

There are, however, several limitations for the practical use of nanorod arrays. For example, the enhancement of stress has a limitation because of the mechanical strength of the piezoelectric material. Since in the environment the vibration cannot be applied perfectly along the axial direction of the nanorods, it is inevitable that lateral oscillations of a low frequency are generated. Such lateral oscillations cause shear stresses in the nanorods, which become larger with decreasing the area ratio of nanorod array. Therefore, the nanogenerators have to be designed so that the induced stresses can be enough below the fracture stress. It should also be noted that the output voltage and power in the practical devices will be limited by the mechanical, dielectric and piezoelectric damping, though they are not major factors to limit power at off-resonance frequencies. For example, the effect of dielectric loss on the output power can be neglected due to the low working frequency (hundreds of Hz) of the PEH devices.

2.3.3 Comparison of devices in the 33 and 31 modes

From the perspective of applying nanorods to practical PEH devices, it is necessary to compare the nanorod array with the cantilever structure which has been widely utilized so far. In this study, three structures, (1) a nanorod array in the 33 mode, (2) a film in the 33 mode and (3) a film in the 31 mode are selected and compared to evaluate the output performance of the nanorod array. As shown in Figure 2-9, piezoelectric layers in the three models occupy the same volume, and the same mass is applied to them. The vibration source is expressed as

$$F = M \cdot ACC \cdot sin(2\pi f t), \tag{2-25}$$

where ACC is the acceleration, which is fixed to 10 m/s^2 in the simulation, and f is the frequency (where $f = \omega/2\pi$) of the vibration. The aspect ratio of h/b = 10 is employed to the nanorods as used in the former study. For the purpose of shortening the computation time, the density of the nanorod array x_{NR} is set to 0.09 to reduce the number of the nanorods. According to the given dimensions, the resonant frequency f_{r} is 105 Hz for the cantilever-based film (Structure 3) and over 200 kHz for the 33-mode structures. The output power is calculated by connecting the piezoelectric layers to an optimal external resistance, namely $R = X_{\mathrm{C}}$.

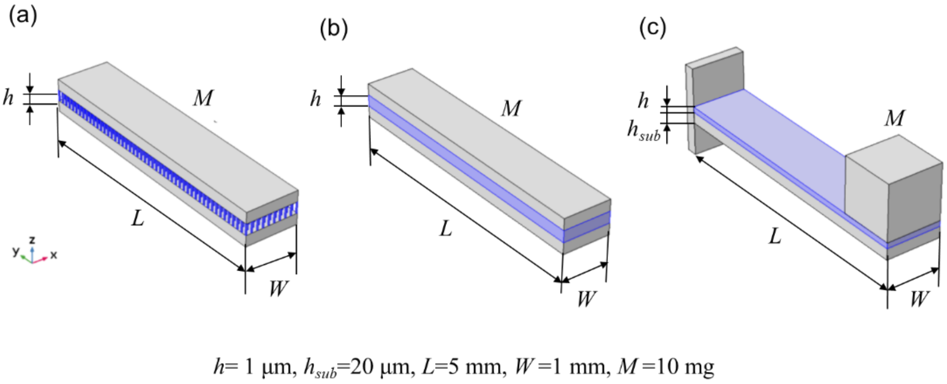

Figure 2-9 Schematic models for comparison, with the same volume and the same mass applied to the piezoelectric layers. (a) A nanorod array in the 33 mode. (b) A film in the 33 mode (c) a film in the 31 mode.

Figure 2-10(a) shows the frequency response from 0 to 200 Hz on the output power density for these structures. It is clearly shown that the nanorod array generates higher power than the film in the same working mode, but much lower than the cantilever-based film. Of note, the power density of the cantilever structure at the resonant frequency is over 1 W/cm^3, which has exceeded that of the best-performing PEH devices in literature [38, 59–60]. This is because the device in the simulation induces a large stress over 500 MPa in the piezoelectric layer, which will not be achieved in reality. Nevertheless, the output power density of the 33-mode structures is far lower than the cantilever even away from the resonance.

Except for the output power density, it is found that the nanorod array has some other advantages over the cantilever structure. According to the simulation result, the high output power in cantilever-based device is due to the high input power, which can be expressed as $P_{in} = F^2/2k$, where k represents the spring constant of the device. k for these three structures is known as the following expressions.

$$k = \frac{LWY}{h} \text{ for film or nanorods in the 33 mode} \tag{2-26}$$

$$k = \frac{Wt_{sub}{}^3 Y_{sub}}{4L^3} \text{ for film cantilever in 31 mode [61]} \tag{2-27}$$

where Y and Y_{sub} stand for Young's moduli of the piezoelectric and the substrate, respectively. Using the parameters shown in Figure 2-9 and Table 2-1 (in which Y of the piezoelectric layer can be estimated by $Y = 1/s_{11}$), it is known that the cantilever is more efficient to acquire larger input power due to the low k. However, for the nanorod structure, the mechanical-to-electrical conversion efficiency, defined as a ratio of the output power to the input power, is twice higher than that of the cantilever structure as shown in Figure 2-10(b). It is because the cantilever-based PEH devices, especially those with piezoceramic layers, need metal substrates to avoid cracking during the bending, and thus part of the input power is obtained by the substrates.

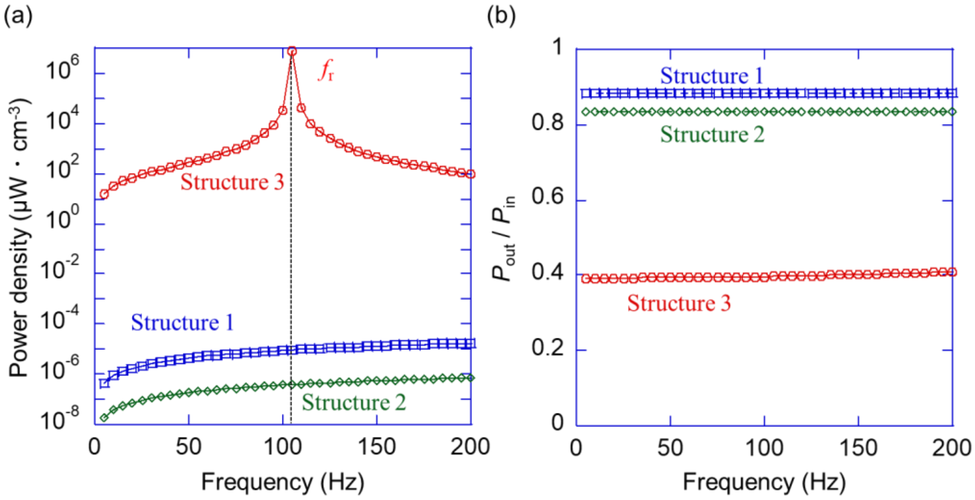

Figure 2-10 (a) The frequency response from 0 to 200 Hz on the power density for three studied structures. (b) Comparison of the conversion efficiency, defined as the ratio of the output power to the input power within the piezoelectric layers.

Another merit of the nanorod structure is the good compatibility with the miniaturized PEH devices. Figure 2-11 shows the dependence of output power density at 100 Hz on the length of the device loaded with a constant mass. It is found that the output of the nanorods increases with decreasing device length and is expected to exceed that of the film cantilever in the 31 mode when the length is less than 700 μm. This is because the resonant frequency of the film cantilever in the 31 mode significantly deviates from the vibration frequency. It is obviously difficult to fabricate microscale cantilevers at such a low resonant frequency. Therefore, fabricating nanorods can be a good alternative for powering miniaturized microsensors.

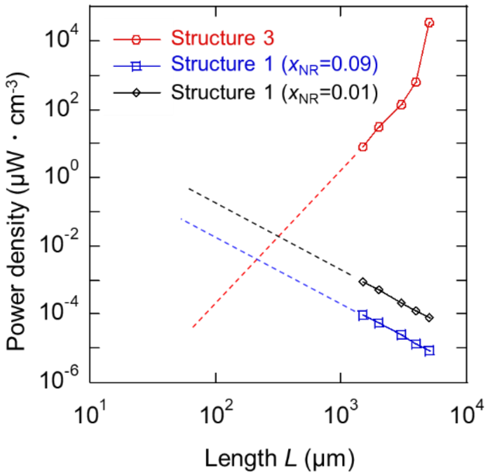

Figure 2-11 Dependence of output power density on the length of the device.

2.4 Conclusion

The nanorod structure has been proved to be an effective strategy to reduce the substrate clamping and enhance the out-of-plane output performance via the theoretical analysis. The aligned nanorod array will be a competitive candidate as an off-resonant PEH device, compared with the traditional cantilever-based PEH that has difficulty in operating at resonance in a volume of mm^3 or less. The enhancement of the output performance is confirmed from the following results.

1) Enhanced d_{33} and FOM. A low lateral stress is induced in the piezoelectric unit with a large aspect ratio, indicating the easier deformation of the nanorods than that of the film when the same stress is applied. d_{33} of the nanorods is closed to the bulk d_{33} which is 33% higher than the clamped direct d_{33} for the film, and thus a 77% enhanced FOM_{33}.

2) Enhanced V_{open} and P_{out} from the decreased x_{NR}. The density of the nanorod array could achieve larger V_{open} and P_{out} than that of a dense film, showing a larger impact over the aspect ratio.

3) Higher P_{out}/P_{in} than that of the cantilever. The cantilever achieves large input power at resonance due to a low k, while the 33-mode structures show the P_{out}/P_{in} twice higher than that of the 31-mode film, because the substrate does not account for the energy conversion in the 33 mode.

4) Enhanced P_{out} independent of the frequency. It is shown that the output of the nanorods increases with decreasing device length and tends exceed that of the film cantilever in the 31 mode when the length is less than 700 μm, because the resonant frequency of the film cantilever in the 31 mode significantly deviates from the vibration frequency.

2.5 References

52. L. Gu, N. Cui, L. Cheng, Q. Xu, S. Bai, M. Yuan, W. Wu, J. Liu, Y. Zhao, F. Ma, and Y. Qin. Flexible fiber nanogenerator with 209 V output voltage directly powers a light-emitting diode. *Nano Letters*, **13**, 91-94 (2013).
53. V. Nagarajan, A. Roytburd, A. Stanishevsky, S. Prasertchoung, T. Zhao, L. Chen, J. Melngailis, O. Auciello, and R. Ramesh. Dynamics of ferroelastic domains in ferroelectric thin films. *Nature Materials*, **2**, 43-47 (2003).
54. J. H. Li, L. Chen, V. Nagarajan, R. Ramesh, and A. L. Roytburd. Finite element modeling of piezoresponse in nanostructured ferroelectric films. *Applied Physics Letters*, **84**, 2626-2628 (2004).
55. V. Nagarajan. Scaling of the piezoelectric response in ferroelectric nanostructures: An effective clamping stress model. *Applied Physics Letters*, **87**, 242905 (2005).
56. M. J. Haun, Z. Q. Zhuang, E. Furman, S. J. Jang, and L. E. Cross. Thermodynamic theory of the lead zirconate-titanate solid solution system, part III: Curie constant and sixth-order polarization interaction dielectric stiffness coefficients. *Ferroelectrics*, **99**, 45-54 (1989).
57. A. F. Barzegar, D. Damjanovic, and N. Setter. The effect of boundary conditions and sample aspect ratio on apparent d_{33} piezoelectric coefficient determined by direct quasistatic method. *IEEE*

transactions on ultrasonics, ferroelectrics, and frequency control, **51**, 262-270 (2004).

58. M. J. Haun, E. Furman, S. J. Jang, and L. E. Cross. Thermodynamic theory of the lead zirconate-titanate solid solution system, part I: phenomenology. *Ferroelectrics*, **99**, 13-25 (1989).
59. K. H. Cho, H. Y. Park, J. S. Heo, and S. Priya. Structure–performance relationships for cantilever-type piezoelectric energy harvesters. *Journal of Applied Physics,* **115**, 204108 (2014).
60. J. Q. Liu, H. B. Fang, Z. Y. Xu, X. H. Mao, X. C. Shen, D. Chen, H. Liao, and B. C. Cai. A MEMS-based piezoelectric power generator array for vibration energy harvesting. *Microelectronics Journal,* **39**, 802-806 (2008).
61. E. L. Worthington. Piezoelectric energy harvesting: enhancing power output by device optimization and circuit techniques, PhD Thesis, Cranfield University (2010).

Chapter 3 - Enhanced FOM from the decreased density of PZT nanorod arrays

3.1 Introduction

As given in Eq. (1-1), the output performance of a PEH device can be predicted by evaluating its available energy E_a. With respect to the case of a nanorod array applied with a static force $F = x_{NR}A\sigma_3$, E_a is expressed as Eq. (3-1) with the substitution of C_{NR} in Eq. (2-15).

$$E_a = \frac{1}{2} \cdot \frac{\varepsilon_{33} x_{NR} A}{h} \cdot \left(\frac{d_{33} F h}{\varepsilon_{33} x_{NR} A}\right)^2 = \frac{1}{2} \cdot \frac{d_{33}^2}{\varepsilon_{33} x_{NR}} \cdot F^2 \cdot \left(\frac{h}{A}\right) \tag{3-1}$$

Here one obtains the figure of merit of the nanorod-based PEH device, which is also called the effective FOM (denoted with $\mathrm{FOM_{eff}}$).

$$\mathrm{FOM_{eff}} = \frac{d_{33}^2}{\varepsilon_{33} x_{NR}} \tag{3-2}$$

In Chapter 2, it has been predicted that the output power of the nanorod array can be enhanced due to the increased d_{33} and the decreased density compared with a 33-mode film. For the application of PEH, there is seldom straightforward strategy to achieve a large FOM in a piezoelectric film since the dielectric and piezoelectric properties have a positive correlation. Thus it is significant to employ the nanorod structure to PEH devices due to a large $\mathrm{FOM_{eff}}$ which can be realized by decreasing x_{NR}. As a matter of fact, the high $\mathrm{FOM_{eff}}$ achieved in the nanorod array is not only due to the decreased density. It has been reported [62–64] that the epitaxial PZT nanorods, owing to the release of substrate clamping and a large aspect ratio, exhibits a unique single-domain structure which can improve the out-of-plane piezoelectric response. However, for evaluating $\mathrm{FOM_{eff}}$, it is difficult to distinguish the contribution of d_{33} from x_{NR}.

In this chapter, a strategy to emphasize the contribution of the decreased density of the nanorod array is proposed, by fabricating the tetragonal PZT nanorods using PLD with a rapid growth rate. It has been revealed that growing nanorods by PLD is generally based on two methods, i.e. using either an elevated pressure or an elevated deposition rate. The former method can realize spatially separated nanorods, for which the domain structure is different from that of a clamped film and is strongly affected by their size and their electrostatic boundary conditions [62–64]. Such nanorods may exhibit an improvement of the piezoelectric constant. In contrast, the latter method can fabricate the nanorods with a similar the domain structure to that of a clamped film [65], which can be used for clarifying the effect of the decreased density on $\mathrm{FOM_{eff}}$. Discussion on (1) the crystallinity and domain structure, (2) dielectric, converse piezoelectric and direct piezoelectric properties, (3) E_a and FOM is conducted in this study.

3.2 Experimental

The study employed Pb($Zr_{0.35}Ti_{0.65}$)O_3, a tetragonal PZT at room temperature, to form the nanorods and films on $SrTiO_3$ (STO) (001) substrates by PLD. The PZT ceramic with 5%-excess PbO sintered by spark plasma sintering was used as a target. A KrF excimer laser with the wavelength of $\lambda = 248$ nm, energy of 59.4 mJ and a repetition rate of 5 Hz was used for deposition. The nanorod or film growth depended on the pressure and temperature [62,66] can be schematically illustrated by Figure 3-1. For the second method of growing nanorods, the oxygen pressure was set to 200 mTorr, and the target–substrate distance was shortened to 37 mm to increase the deposition rate. As a result, the PZT samples were fabricated with a thickness of ~1 μm using the relatively fast deposition rate of 8.3 nm/min. A dense film as comparison was fabricated by increasing the substrate temperature. Before the fabrication of the PZT samples, SrRuO3 (SRO) bottom electrode layers with a thickness of 30 nm were deposited on STO at 700°C with 200 mTorr of O_2 via PLD. After the fabrication of the PZT films and nanorods, 100-μm diameter Pt top electrodes were deposited by electron-beam evaporation (EBV). Detailed fabrication parameters are listed in Table 3-1.

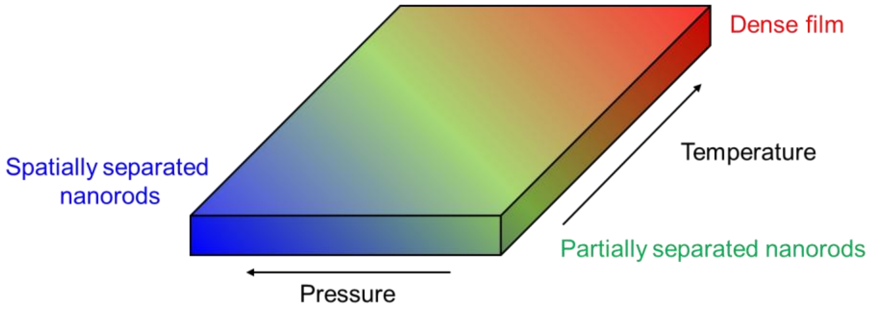

Figure 3-1 A schematic change from the film growth to the nanorod growth by adjusting pressure and temperature

Table 3-1 Fabrication parameters of electrodes and the studied samples

	Method	Material	Temperature (°C)	Pressure (mTorr)	Energy / Current	Thickness (nm)
Bott. electrode	PLD	$SrRuO_3$	700	200	59.4 mJ, 10 Hz	30
PZT film	PLD	PZT	590	200	59.4 mJ, 5 Hz	1000
PZT nanorod	PLD	PZT	575	200	59.4 mJ, 5 Hz	1000
Top electrode	EBV	Pt	RT	$<10^{-4}$	200 mA	30

For the measurement, the orientation and domain structure of PZT were characterized by XRD using four-axis diffractometers with Cu Kα1 X-rays (Bruker, D8 Discover), and the microstructure was characterized by field emission scanning electron microscopy (SEM) (Hitachi, S-4800). The dielectric constant was measured using an LCR meter (Agilent Technologies, E4980A). The converse piezoelectric constant was characterized by a double beam laser interferometer (DBLI) (aixACCT Systems GmbH, aixDBLI), and the direct piezoelectric constant was measured using a d_{33} meter (Lead Techno Co.).

3.3 Results and discussion

3.3.1 Morphology and crystal structure

Figure 3-2 shows the SEM images of the fabricated PZT film and nanorods. A dense film was obtained at a substrate temperature of 590°C as shown in Figure 3-2(a) and (c), and aligned nanorods formed at 575°C as shown in Figure 3-2(b) and (d). The area ratio and average width of the nanorods were analyzed by distinguishing the different heights between nanorods and gaps using the software Gwyddion, as the red marked elements shown in Figure 3-2(e). The average width of the nanorods was estimated to be 51 nm and the density of the nanorod array x_{NR} was estimated to be 78%.

The different PZT products were due to temperature-dependent surface diffusion. At low temperature, the diffusivity of the PLD species on the growing surface was suppressed, which promoted the formation of islands and eventually nanorods. Of note, the deposition rate of 8.3 nm/min used in this study was lower than the reported rate [65], which resulted in the formation of a film at a higher temperature of 590°C. The rectangular top of the nanorods, as shown in Figure 3-2(b), implies that PZT was crystallized with $\{100\}_{\mathrm{pc}}$ (where the subscript "pc" means pseudo cubic) facets, which was the most stable surface for the employed deposition conditions [67,68]. The density of 78% is higher than that (55%–60%) used in our previous study where PZT nanorods were fabricated at elevated pressure [63,64]. However, it was rather close to that (above 80%) reported by Nguyen et al. [65] owing to the similar approach for nanorod fabrication.

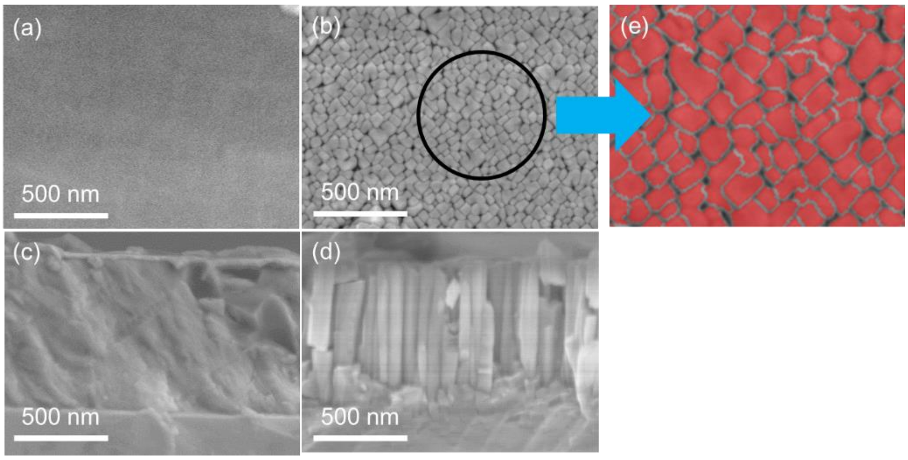

Figure 3-2 (a), (c) SEM images of the PZT film deposited at 590°C and (b), (d) the PZT nanorods deposited at 575°C. (a) and (b) are top views, and (c) and (d) are cross-sectional views.

The crystallinity and domain structures of the fabricated film and nanorods were characterized by XRD. As shown in Figure 3-3, only peaks corresponding to *h*00 and 00*l* of the tetragonal phase were observed in the XRD $2\theta/\omega$ scans, indicating that both the film and nanorods grew epitaxially on the STO substrate with the *a*/*c*-domain structure. The similar intensity of the Miller index peaks of the film and nanorods indicated a comparable crystallinity and domain fraction. The lattice constants of both the film and the nanorods was estimated to be $a = 3.996$ Å and $c = 4.141$ Å, which were close to those of bulk PZT ($a = 3.99$ Å and $c = 4.15$

Å) [69]. This indicated that the fabricated PZT samples were relaxed from the lattice mismatch by forming the *a*/*c*-domain structure during cooling down from the deposition temperature.

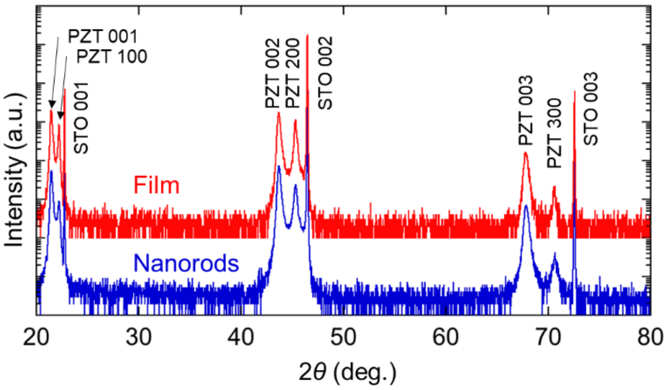

Figure 3-3 XRD $2\theta/\omega$ scans of the fabricated PZT film and nanorods

The volume fraction of the *c*-domains, V_c, was estimated from the XRD reciprocal space maps (RSMs) for PZT 200 and 002, as shown in Figure 3-4(a) and (b). A PZT 002 peak and split PZT 200 peaks along the STO [100] direction were observed, which originated from *c*- and *a*-domains, respectively. Splitting of PZT 200 peaks is often observed in *a*/*c*-domained films with a larger V_c [70] so the elastic energy of the system can be minimized. The intensity that appeared in between the two PZT 200 peaks split along STO [100] is the tail of the PZT 200 peaks that were split along STO [010] because the employed XRD system has a low angular resolution along the STO [010] direction. The physical connectivity of the *a*- and *c*-domains at their {101} plane, shown in Figure 3-4(c), explains the domain structure revealed in the RSMs. Here, the clapping angle, 2α, which represents the angle of mutual rotation of *a*- and *c*-domains, is defined by [71]

$$\alpha = 45° - tan^{-1}(a/c) \tag{3-3}$$

where a and c are the lattice constants. In the RSMs, 2α corresponds to the angle between two lines connecting 000 with 002 and 200. For our PZT film and nanorods, α was estimated from the lattice constant and Eq. (3-3) to be 1.02°, which is close to but slightly larger than that found for the RSMs (0.60° for the film and 0.63° for the nanorods). The smaller α observed for both the film and nanorods could be due to the influence of substrate clamping [72], thus indicating that the nanorods do not fully separate from each other as can also be found in the microstructure shown in Figure 3-4(c). From the XRD intensities of PZT 002 and PZT 200 in the RSM, V_c was estimated to be 52% for the film and 67% for the nanorods. V_c of the fabricated film was close to that found in a previous study [73]. Of note, V_c of the nanorods in this study is somewhat larger than that of the film but much lower than that (100%) of the fully separated nanorods reported in our previous studies [63,64,74]. Thus, the fabricated nanorods are suitable for demonstrating the impact of the reduced density on $\mathrm{FOM_{eff}}$ owing to the negligible change in the domain structure.

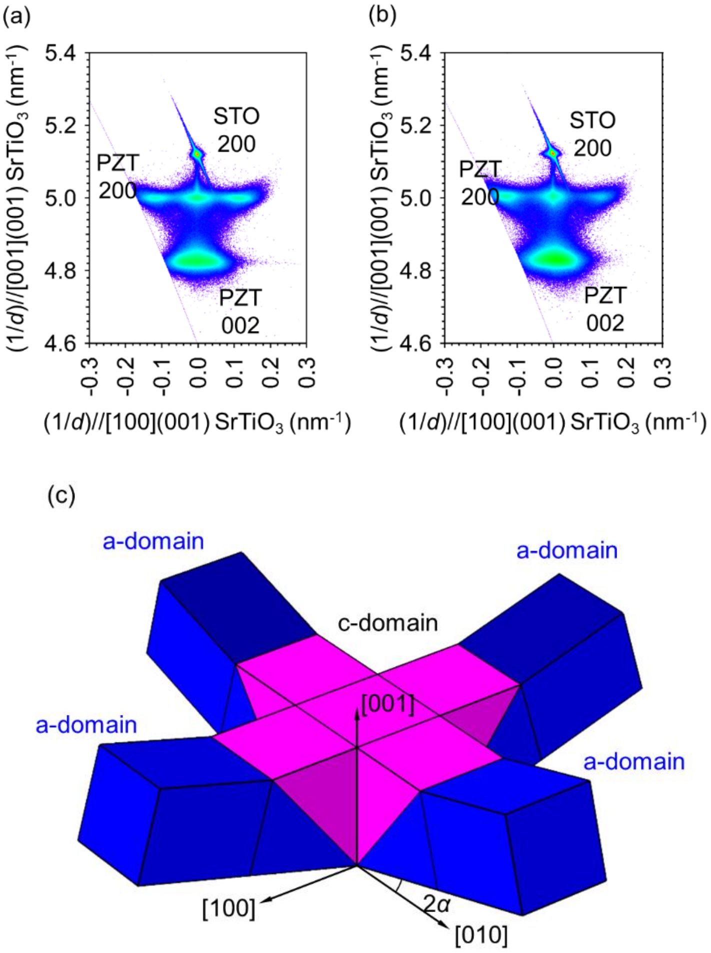

Figure 3-4 XRD RSMs of (a) the film and (b) the nanorods for PZT 200 and 002. (c) Schematic illustration of the *a*/*c*-domain structure in the film and nanorods.

3.3.2 Dielectric and piezoelectric properties

The dielectric properties of the fabricated film and nanorods were measured by an LCR meter from 1 kHz to 1 MHz. As shown in Figure 3-5(a), a lower measured ε is achieved in the nanorod array due to the low ε of the air gaps than in the film. ε only for the PZT part in the nanorod array can be figured out by measured ε divided by x_{NR}. From Figure 3-5(b), the dielectric constant is stable within the measured range, and dielectric loss is lower than 0.1, indicating that the fabricated electrodes showed excellent conductivity that would not affect the electrical properties of the PZT samples. This low dielectric loss can be neglected for evaluating the output performance as discussed in the theoretical analysis.

Figure 3-6 shows the dependence of ε on V_{c}. The open circles denote the ε of the PZT films and nanorods. The theoretical ε of the *a*/*c*-domain structure can be predicted using Eq. (3-4) [75],

$$\varepsilon = \frac{1}{2}\left\{\frac{\varepsilon_a \varepsilon_c}{(1-V_c)\varepsilon_c + V_c \varepsilon_a} + [(1 - V_c)\varepsilon_a + V_c \varepsilon_c]\right\} \tag{3-4}$$

where ε_a and ε_c are the dielectric constants of the *a*- and *c*-domains, respectively. Because ε_c (= 157) is lower than ε_a (= 358) for the employed PZT composition [56], ε of the *a*/*c*-domained PZT decreased with an increase in V_c. Thus, the nanorods that possess a larger V_c have a lower ε than the film. Additionally, the experimental ε is indeed in accordance with the theoretical dependence of ε on V_c. Of note, the filled circle shown in the figure denotes the measured ε of the nanorod array, also known as the effective dielectric constant including ε of the nanorods as well as the air gaps. It is shown that ε is further decreased by the decrease density of the nanorod array, and the effect is larger than that of V_c.

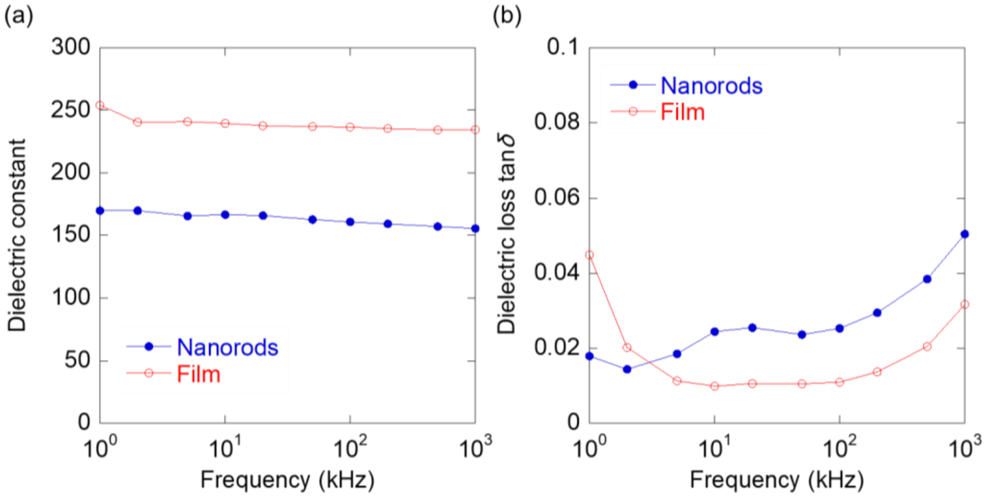

Figure 3-5 Frequency response on (a) dielectric constant and (b) dielectric loss from 1kHz to 1 MHz

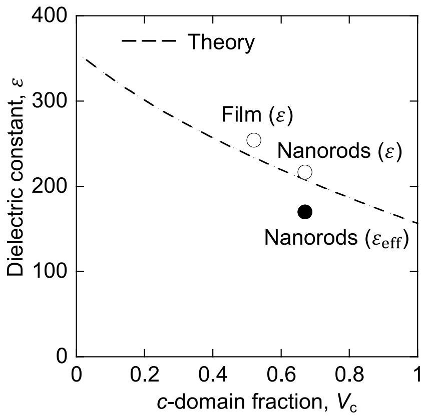

Figure 3-6 Dielectric constant ε and volume fraction of *c*-domains V_c of the fabricated film and nanorods. The theoretical dependence is also shown by the dotted line.

Figure 3-7 shows the converse piezoelectric response of the fabricated film and nanorods characterized by DBLI at 100 Hz. The displacement is almost a linear function of the electric field. The converse d_{33}, acquired from the average value of the positive and negative slopes of the displacement at zero voltage, was estimated to be 92 pm/V for the film and 96 pm/V for the nanorods.

For the direct piezoelectric response, the samples were poled and a load force F with 0.5 s was repeatedly applied normal to the substrate by a d_{33} meter. The generated electrical charges were acquired by a built-in charge amplifier. Figure 3-8(a) shows typical examples of the generated charge profiles during the measurement. The reproducible change in the charge indicated that the direct piezoelectric response of the samples was successfully detected. Based on the acquired charges, the direct d_{33} was estimated to be in the range of 52 to 66 pC/N for the film and 53 to 72 pC/N for the nanorods, as shown in Figure 3-8(b). The lower values of the direct d_{33} compared with those of the converse d_{33} may be due to the poor measurement accuracy. Nevertheless, it can be said that the nanorods showed a similar piezoelectric response compared to the film. Note that the density of nanorods affects neither the converse d_{33} nor the direct d_{33} if V_c is the same. In other words, the difference in V_c should affect d_{33} because the *a*-domains are not active for the d_{33} response. Although there was a 15% difference in the V_c between the film and nanorods, the difference in d_{33} was not clear within the measurement accuracy.

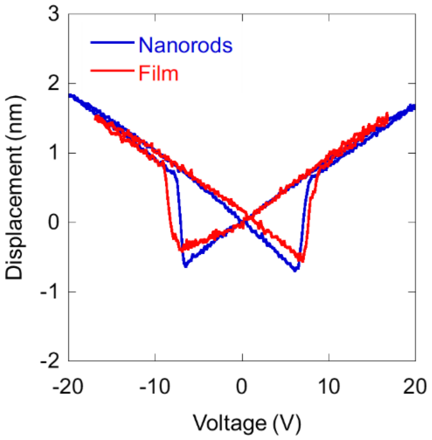

Figure 3-7 Converse piezoelectric response characterized by DBLI at 100 Hz

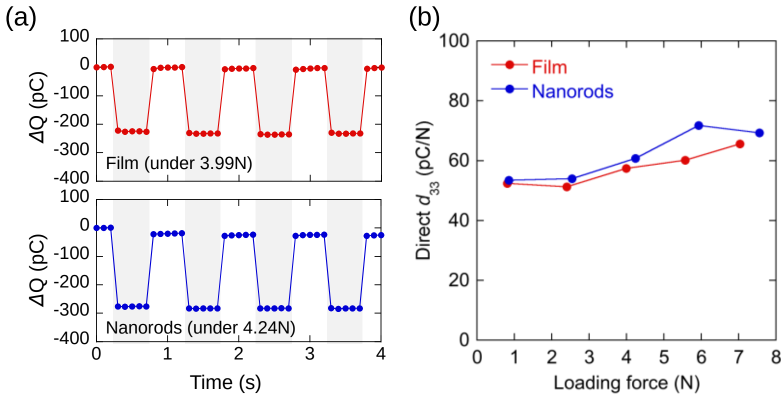

Figure 3-8 (a) Charge profiles generated by the d_{33} meter and (b) the estimated direct d_{33}

3.3.3 Evaluation of FOM$_{\mathrm{eff}}$

E_a is inversely proportional to the density. Namely, a lower density will result in a higher E_a when the same force per area is applied. In Table 3-2, the PEH-related properties between the fabricated PZT film and nanorods are compared. Although the piezoelectric property of the nanorods is similar to the film, the FOM$_{\mathrm{eff}}$ of the nanorods was appreciably enhanced by the reduced density.

Table 3-2 Comparison of PEH-related properties between the fabricated PZT film and nanorods

		Film	Nanorods
x		100%	78%
ε_{eff}		254	170
Converse piezoelectric measurement	d_{33} (pm/V)	92	96
	FOM_{eff} (TPa^{-1})	3.8	6.1
Direct piezoelectric measurement	Ave. d_{33} (pC/N)	62	57
	Ave. FOM_{eff} (TPa^{-1})	1.7	2.2

Since the measurement using the d_{33} meter was based on the open-circuit condition, and applied with the loading force in a square-wave profile, the output power was not obtained directly in this study. Thus, one evaluated the available energy per unit area for different F to reflect the output performance of the PEH devices, as shown in Figure 3-9. The converse piezoelectric measurement was used for the calculation of FOM_{eff} due to the higher accuracy, and FOM_{eff} is assumed to be independent of the load force F. It is seen from Figure 3-9 that E_a of the nanrods is higher than that of the film, and the difference in E_a becomes clear with the increase in F.

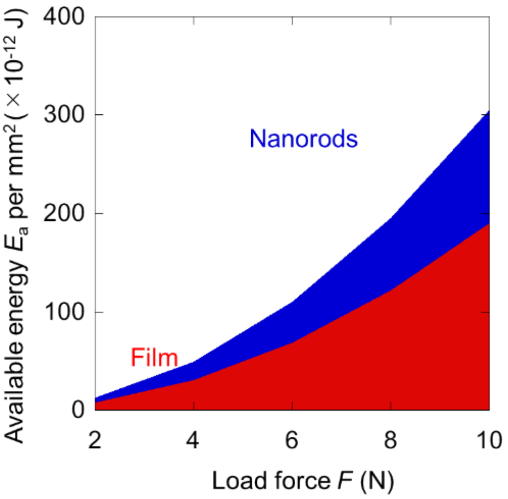

Figure 3-9 Available energy E_a per unit area estimated for the film and nanorods

To further discuss the impact of the reduced density by forming the nanorods on E_a, the relationship between FOM_{eff} and x_{NR} of the nanorods was investigated.

$$\log \text{FOM}_{\text{eff}} = (2 \log d_{33} - \log \varepsilon_{33}) - \log x_{NR} \tag{3-5}$$

As shown by Eq. (3-5), $\log \text{FOM}_{\text{eff}}$ and $\log x_{NR}$ have a linear relationship with the slope of -1. Figure 3-10 shows the log–log plot of FOM_{eff} and x_{NR} for the films and nanorods with different compositions and orientations. Here, the nanorods for comparison are the spatially separated nanorods with a Zr/Ti ratio of 53/47, known as the MPB composition of PZT. These nanorods have a small x_{NR} and a remarkably enhanced d_{33} (355 and 131 pm/V for (111)- and (001)-orientation) as compared with the films (138 and 78 pm/V for (111)- and (001)-orientation), the details of which will be further investigated and described elsewhere. It is interesting that the FOM enhancement in these nanorods show an appreciable deviation from the line with the slope of −1 owing to the enhanced d_{33}. In contrast, the dependence of the film and nanorods achieved in this study is closer to the slope of –1. According Eq. (3-5), it is indicated that the enhanced FOM_{eff} can be basically explained by the decrease of the density. The comparison on the log–log plot of FOM_{eff} and x_{NR} provides a method to clearly distinguish the contribution of the decreased density of the nanorod array from other factors, and indicates the promising application of the nanorod-based PEH devices.

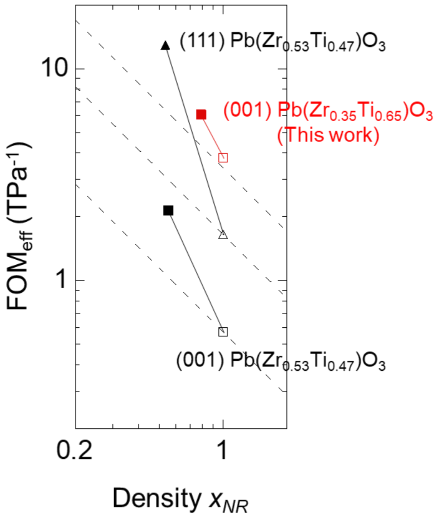

Figure 3-10 Log–log plot of FOM_{eff} and x_{NR} for the films and nanorods. Open and filled symbols denote films and nanorods, respectively. Dashed lines are the lines with the slope of −1 through the data of the films. For the comparison, FOM_{eff} of the spatially separated nanorods and films of $PbZr_{0.53}Ti_{0.47}O_3$ are also plotted.

3.4 Conclusion

This study experimentally clarified that the effective FOM of the PZT nanorod array can be enhanced by the decreased density by comparing the nanorods with a film having the same orientation and similar domain structure. This approach enables us to independently control the piezoelectric and dielectric constants of materials, making it possible to lower the effective dielectric constant while maintaining the piezoelectric constant. In addition, a method to distinguishes the effect of the decreased density from that of the other factors is proposed, which makes it possible to evaluate the FOM of the nanorod array in a more accurate way. The following results indicate that piezoelectric nanorods are a prospective candidate for small-sized PEH devices where the cantilever-based PEH cannot be used at a resonant frequency.

1) Nanorods with a similar domain structure to the film. By increasing the growth rate while maintaining the deposition pressure, the nanorod structure originated from the suppressed diffusion of the deposition species forms, and a/c domain structure is basically identical to a dense film which is suitable for highlighting the effect of the decreased density of the nanorod array.

2) Lower effective dielectric constant and similar piezoelectric properties. Owing to the similar structure with the film, the converse and direct piezoelectric properties do not change to a large degree. However, the effective dielectric constant decreased clearly by decreasing the density of the nanorod array, indicating an effective way to control the dielectric properties independent of the piezoelectric response for a desired FOM.

3) Enhanced FOM from the decreased density. The observed dielectric and piezoelectric properties give an enhanced effective FOM_{33} in the nanorod array, which can be regarded as a prospective candidate for the off-resonant PEH.

3.5 References

62. K. Okamoto, T. Yamada, J. Yasumoto, K. Nakamura, M. Yoshino, and T. Nagasaki. Influence of deposition conditions on self-assembled growth of $Pb(Zr,Ti)O_3$ nanorods by pulsed laser deposition at elevated oxygen pressure. *Journal of the Ceramic Society of Japan*, **126**, 276-280 (2018).
63. T. Yamada, D. Ito, T. Sluka, O. Sakata, H. Tanaka, H. Funakubo, and N. Setter. Charge screening strategy for domain pattern control in nano-scale ferroelectric systems. *Scientific Reports*, **7**, 1-9 (2017).
64. K. Okamoto, T. Yamada, K. Nakamura, H. Takana, O. Sakata, M. Phillips, T. Kiguchi, M. Yoshino, H. Funakubo, and T. Nagasaki. Enhanced intrinsic piezoelectric response in (001)-epitaxial single c-domain $Pb(Zr,Ti)O_3$ nanorods. *Applied Physics Letter*, **117**, 042905 (2020).
65. M. D. Nguyen, E. P. Houwman, M. Dekkers, and G. Rijnders. Strongly enhanced piezoelectric response in lead zirconate titanate films with vertically aligned columnar grains. *ACS Applied Materials & Interfaces*, **9**, 9849-9861 (2017).
66. J. A. Thornton. High rate thick film growth. *Annual Review of Materials Science*, **7**, 239-260 (1977).
67. Y. Takagi, T. Yamada, M. Yoshino, T. Nagasaki. Ab initio study on face azimuth dependency of surface energy and structure in $PbTiO_3$. *Ferroelectrics*, **490**, 167-173 (2016).
68. J. M. Zhang, Q. Pang, K. W. Xu, and V. Ji. First-principles study of the (001) surface of cubic $PbTiO_3$. *Surface and Interface Analysis*, **40**, 1382-1387 (2008).
69. K. Kakegawa, J. Mouri, K. Takahashi, H. Yamamura, and S. Shirasaki, *The Chemical Society of Japan*, **49,** 717 (1976). [in Japanese]
70. H. Nakaki, Y. Kim, S. Yokoyama, R. Ikariyama, K. Nishida, K. Saito, and H. Funakubo. Strain-relaxed structure in (001)/(100)-oriented epitaxial $PbTiO_3$ films grown on (100) $SrTiO_3$ substrates by metal organic chemical vapor deposition. *Applied Physics Letters*, **91**, 112904 (2007).
71. A. K. Tagantsev, L. E. Cross, and J. Fousek. Domains in ferroic crystals and thin films. Springer, New York, p. 66 (2010).
72. D. Ito, T. Yamada, M. Yoshino, T. Nagasaki, O. Sakata, J. Kuroishi, T. Namazu, T. Shiraishi, T. Shimizu, and H. Funakubo. Fabrication of tetragonal $Pb(Zr,Ti)O_3$ nanorods by focused ion beam and

characterization of the domain structure. *IEEE Transactions on Ultrasonics, Ferroelectrics and Frequency Control*, **63**, 1642 (2016).

73. T. Fujisawa, H. Nakaki, R. Ikariyama, H. Morioka, T. Yamada, K. Saito, and H. Funakubo. Thick epitaxial $Pb(Zr_{0.35}Ti_{0.65})O_3$ films grown on (100) CaF_2 substrates with polar-axis-orientation. *Applied Physics Express*, **1**, 085001 (2008).
74. T. Yamada, D. Ito, O. Sakata, J. Kuroishi, T. Namazu, Y. Imai, and T. Nagasaki. Domain structure of tetragonal $Pb(Zr,Ti)O_3$ nanorods and its size dependence. *Japanese Journal of Applied Physics*, **54**, 10NA07 (2015).
75. T. Yamada, C. S. Sandu, M. Gureev, V. O. Sherman, A. Noeth, P. Muralt, and N. Setter. Self-assembled perovskite-fluorite oblique nanostructures for adaptive (tunable) electronics. *Advanced Materials*, **21**, 1363-1367 (2009).

Chapter 4 - Fabrication of PZT nanorods by RF-magnetron sputtering

4.1 Introduction

It has been reported that PZT nanorods form in high pressure or with a rapid growth rate during physical vapor deposition [62–66]. The mechanism of the nanorod growth can be illustrated by Figure 4-1 [76]. With a rapid growth rate, the diffusion of the PZT species is limited and then island growth occurs on the substrate. The similar non-uniform growth can also be achieved in high pressure, due to the reduced energy of the species. In addition, the species in the high pressure are scattered in various incident angle onto the substrate, and predominantly accumulate on the top of the islands. This growth process is also known as the shadowing effect [66]. As a result, the islands isolate with each other and continue to grow into the nanorods.

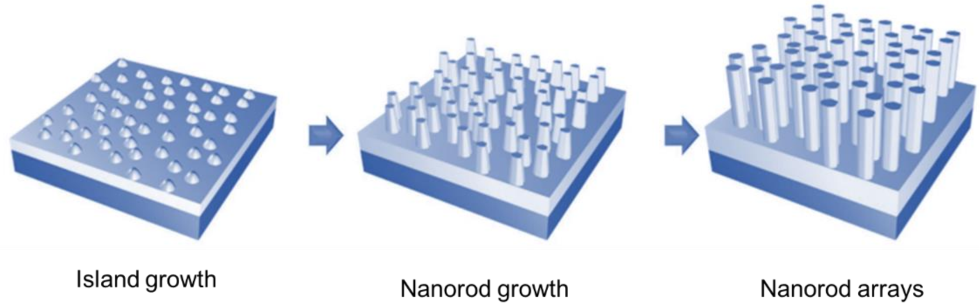

Figure 4-1 Schematic diagram illustrating the mechanism of growing epitaxial nanorod arrays [76].

For the purpose of commercializing the nanorod-based PEH devices, PZT nanorods are expected to grow in an area up to several cm^2 and thus the fabrication using RF-magnetron sputtering is taken into consideration. However, when employing the deposition parameters for PLD to the case of sputtering, the following problems must be dealt with. (1) The growth rate of sputtering is limited because an extra high RF power would crack the ceramic target. (2) Different from the pulsed laser, the stability of the plasma for sputtering is severely affected by the pressure. For example, a high pressure would cause the discharge of the plasma on the places other than the substrate. (3) Since the atmosphere (Argon and oxygen) in sputtering is different from that (only O_2) in PLD, the partial pressure of O_2 would also be a parameter of affecting the nanorod growth and needs to be investigated.

In this chapter, the strategy to grow PZT nanorods without elevating the pressure and the optimal fabrication condition are investigated. Effect of the parameters that are independent of the particle energy, such as Pb concentration in targets, target–substrate distance and deposition time, are first investigated on the crystallinity and growth rate of the PZT samples. Then the effect of temperature and pressure which affect the particle energy are investigated on the crystallinity and possibility of forming nanorods. In particular, it is found that the O_2 partial pressure also plays an important role in forming the nanorod structure, which can be used as a strategy to avoid high pressure sputtering.

4.2 Experimental

For the RF-magnetron sputtering method, the investigated conditions of depositing PZT on STO are listed in Table 4-1. 2-inch PZT ceramics with a Zr/Ti ratio of 35/65 and 10% or 20% excessive Pb is used as the sputtering target. The STO (001) and (111), with a 30 nm SRO layer deposited by PLD as the bottom electrode, is used as the substrates. The sputtering power is no higher than 110W and 5.4 W/cm^2 above which the target will severely crack and get poisoned (The sputter product forms on the target instead of on the substrate, or target itself is reacted). The sputter gun is set right under the substrate at the first investigation stage and then change to a 45° for the multiple sputtering. Before the deposition, the base pressure is decreased down to 5×10^{-4} Pa. Other parameters are investigated in a range as shown in Table 4-1. The crystallinity and the microstructure of the fabricated PZT sample are characterized by XRD and SEM, respectively.

Table 4-1 Parameters for (001) PZT

Target	$Pb_{1.1}Zr_{0.35}Ti_{0.65}O_3$, $Pb_{1.2}Zr_{0.35}Ti_{0.65}O_3$
Substrate	SRO//STO (001), SRO//STO (111)
RF Power (W)	100–110
Position of sputter gun	0°, 45°
T-S distance (mm)	60–80
Temperature (°C)	500–650
Base pressure (Pa)	5×10^{-4}
Working pressure (Pa)	0.6–27
$Ar:O_2$	40:1–2:1
Thickness (nm)	300–900

At the first investigation stage, parameters that seldom affect the free mean path of the sputtered particles, such as Pb content in targets, T–S distance and deposition time are investigated. The optimal conditions used in the second investigation stage are confirmed based on the fact that crystalized perovskite PZT is able to grow epitaxially on STO with a high growth rate as much as possible. Then the parameters related to the free mean path of the sputtered particles, i.e. temperature and pressure, including the O_2 partial pressure, are investigated with respect to the effect on crystallinity, growth rate and the formation of the nanorod structure in details.

4.3 Result and discussion

4.3.1 Effect of Pb content, T–S distance and thickness

Figure 4-2 shows the XRD patterns of PZT deposited on STO (111) by the targets with different Pb contents. T–S distance of 70 mm, pressure of 2.9 Pa, Ar:O_2 of 8:1, deposition time of 2 h and temperature of 567 °C and 611 °C are selected in a generally used range [76,78]. It is shown that only the peak of PZT (111) is observed from the PZT deposited by the target with 20% excessive Pb while the pyrochlore phase (chemical formula $A_2B_2O_7$, denoted as Py in the XRD patterns) appears in the PZT deposited by the target with 10% excessive Pb at 567 °C. The pyrochlore phase is due to the evaporation of Pb during the deposition where a compound with a low lead ratio forms more easily than the stoichiometric perovskite PZT. Therefore, the target with 20% excessive Pb is selected for the undermentioned studies.

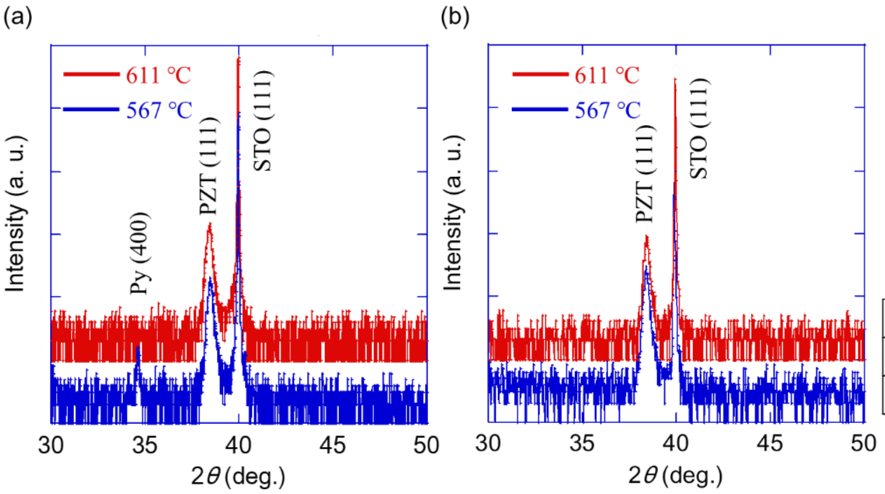

$d_{T–S}$ (mm)	70
Pressure (Pa)	2.9
Ar:O_2	8:1

Figure 4-2 Effect of excessive Pb in the target. (a) Pb+10%, (b) Pb+20%. Other parameters are given in the table.

Effect of the T–S distance is clarified by the PZT deposited on STO (111), using the pressure of 2.9 Pa, Ar:O_2 of 8:1, deposition time of 3 h and temperature of 620 °C. Figure 4-3 and Figure 4-4 show the XRD and SEM results of the fabricated samples, respectively. All the PZT samples show the *a*/*c*-domain structure grown epitaxially on the substrate, similar to the XRD patterns around STO (002) originated from the PZT fabricated by PLD as shown in Figure 3-4. However, it is also shown that weak peaks from the pyrocholre phase are observed in PZT deposited at $d_{T–S}$ = 70 mm and the intensity becomes strong as $d_{T–S}$ decreases. The reason for the crystallinity degradation could be the strong damage of the sputtered species onto the substrate. This is also implied from the top views in the SEM images by characterizing the rough surface of the PZT deposited at $d_{T–S}$ = 60. In addition, it is seen from the cross-sectional views that shorter $d_{T–S}$ achieves higher growth rate, indicating the advantage of forming the nanorod at the short T–S distance, in despite of the accompanied pyrochlore phase. Thus, considering to use a high growth rate with the desired crystallinity, 70 mm is selected as the optimal T–S distance for the deposition hereafter.

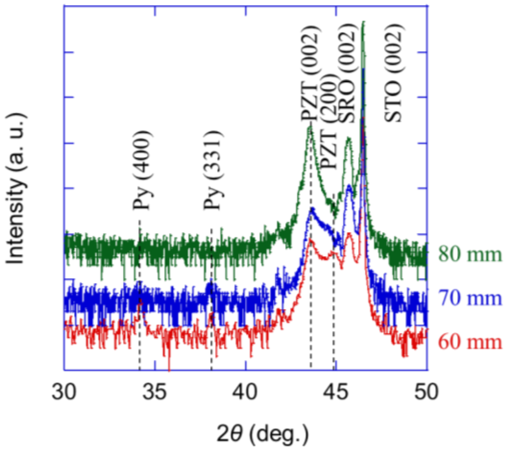

Temperature (°C)	620
$d_{\mathrm{T–S}}$ (mm)	70
Pressure (Pa)	2.9
Ar:O_2	8:1

Figure 4-3 XRD patterns of PZT depended on the T–S distance

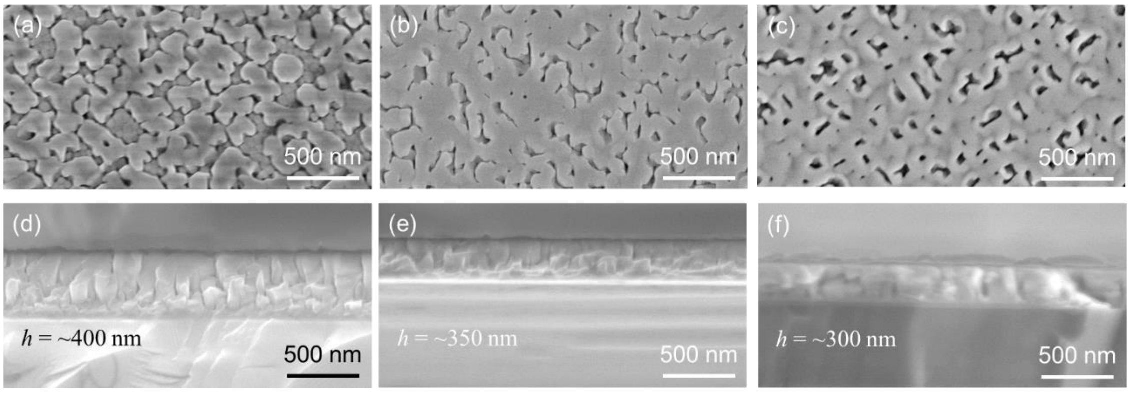

Figure 4-4 SEM images of PZT depended on the T–S distance. (a), (d) $d_{\mathrm{T–S}}$ = 60 mm, (b), (e) $d_{\mathrm{T–S}}$ = 70 mm, (c), (f) $d_{\mathrm{T–S}}$ = 80 mm. top views are shown in (a)–(c) and cross-sectional views in (d)–(f).

Even if the suitable environment for growing nanorods is obtained, it takes the necessary time to form the split columns aligning to the substrate, as illustrated in Figure 4-1 [76]. The effect of the film thickness is also investigated in the case of RF-magnetron sputtering. PZT (001) samples with different thickness are fabricated at the temperature of 620 °C, pressure of 1.4 Pa and Ar:O_2 of 8:1. As shown in Figure 4-5, the rectangular top of the surface implies that PZT has crystallized in the {100} facets. In the thick samples, the surface becomes more rough and exhibit the tendency of forming the isolated islands, agreeing with the illustration in Figure 4-1. Nevertheless, the cross-section shows that a dense film is fabricated even with the thickness of 900 nm.

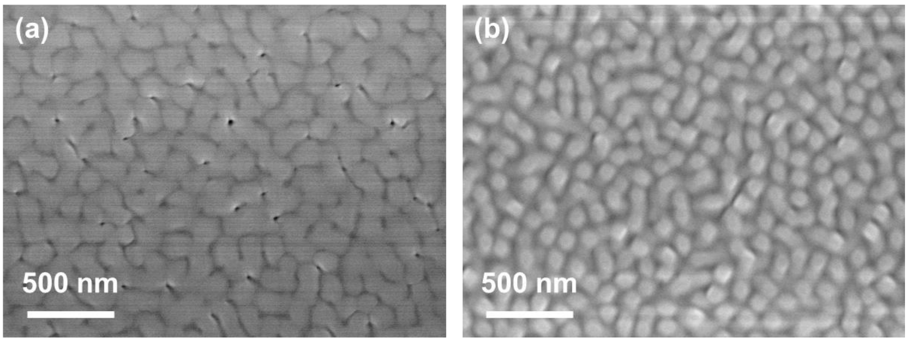

Figure 4-5 change of the surface depended on thickness. (a) h = 300 nm, (b) h = 900 nm.

4.3.2 Effect of temperature and pressure

Since the parameters studied in the above section do not affect the free mean path of the PZT species, these can be optimized by achieving a high growth rate with good crystallinity. Nevertheless, the highest growth rate is no more than 2.3 nm/min which is for lower than that in PLD. Thus, the number of RF sputtering guns is increased to three and equipped in the place 45° deviated from the bottom. RF power of each gun is set to be 100 W with the same angular phase. According to the previous study [62,64], PZT nanorods are easier to grow on STO (111) than STO (001), which is considered to investigate the effect of temperature and pressure in the next study.

Figure 4-6 and Figure 4-7 show the XRD patterns and SEM images of the PZT deposited at different temperatures. The deposition time is 2 h and the working pressure is 2.9 Pa with Ar:O_2 of 8:1. It is shown that PZT does not crystalize at 500 ℃ while forms the complete perovskite phase above 600 ℃. PZT with the complete perovskite phase shows the tendency of splitting into separate nanorods, but still forms into a dense film from the cross-sectional views. For the sputtering temperature of 550-600 ℃, pyrochlore and perovskite coexist in the PZT samples. It is worth noting from the SEM images that PZT grows separately into columns in the temperature of 550-600 ℃. In particular, triangle grains are observed in the PZT deposited at 600 ℃, which is close to those of the (111) nanorods fabricated by PLD [62]. Detailed crystallization is illustrated by Figure 4-8. It is found that the non-uniform crystallization is achieved at 580 ℃. This scenario can provide the chances for growing nanorods as reported in the previous study [66].

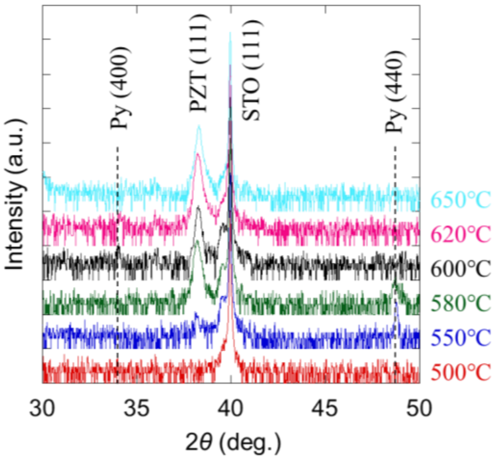

Figure 4-6 XRD of the temperature dependence on crystallinity of PZT.

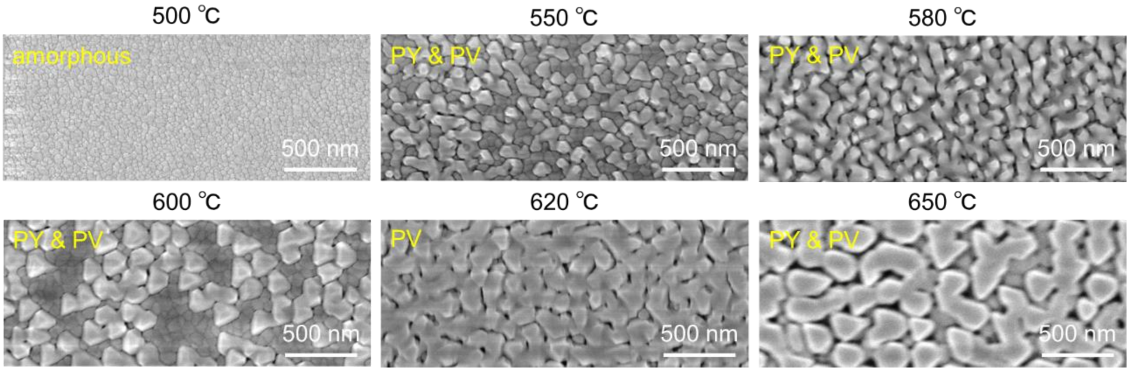

Figure 4-7 SEM images of the top view of PZT sample deposited at different temperature

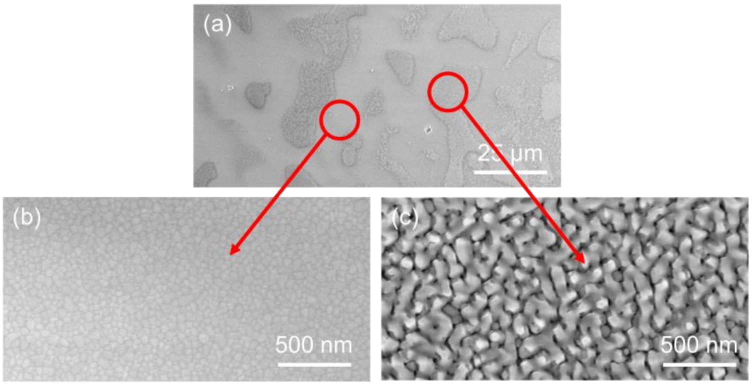

Figure 4-8 Both pyrochlore and perovskite grow at 580 °C(a) The SEM image at low magnification. (b) The pyrochlore part. (c) The perovskite part.

Figure 4-9 shows SEM images for investigating the effect of the working pressure. The deposition time is fixed to 2 h and the temperature is 620 °C with Ar:O_2 of 8:1. It is clearly to see that the pressure is strongly correlated with the growth rate; the higher pressure it is, the lower rate it achieves. Different from the case of using PLD, the pressure and growth rate become contradictive in RF magnetron sputtering to grow the nanorod structure. In addition, it is shown that the low pressure achieves a dense film while high pressure reinforces the tendency of separation but degrades the crystallinity.

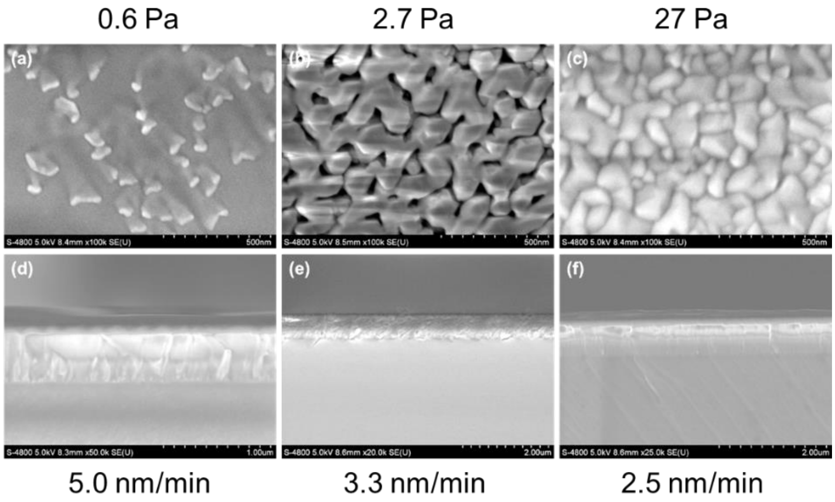

Figure 4-9 SEM images of PZT deposited at different pressure. (a), (d) 0.6Pa, (b), (e) 2.7 Pa, (c), (f) 27 Pa.

Figure 4-10 shows the XRD patterns and SEM images for PZT deposited at different gas composition. SEM images for investigating the effect of the working pressure. The deposition time is 2 h and the temperature is 620 °C with the working pressure of 1.4 Pa. It is shown that the gas composition causes the similar effect as the pressure does. A high O_2 partial pressure benefits the split of PZT but degrades the crystallinity. The effect of the O_2 partial pressure plays a considerable important role in growing PZT nanorods, which makes it possible to achieve the nanorod structure at low pressure and thus the rapid growth can be the dominant factor to grow the nanorods by adjusting Ar:O_2. Since the partial pressure of O_2 affects the crystallinity of PZT. The coexistence of perovskite and pyrochlore shown in Figure 4-8 is considered as a result of the interaction of the temperature and O_2.

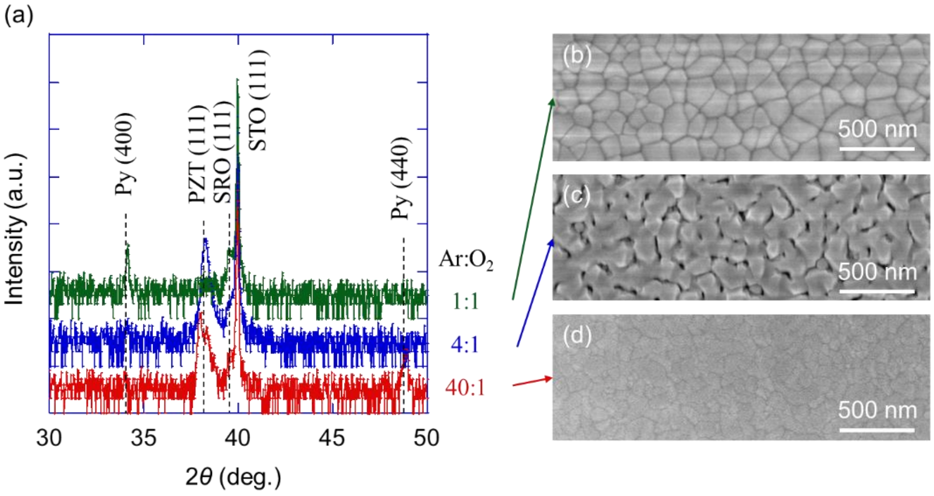

Figure 4-10 (a) XRD patterns and (b)–(d) SEM images for PZT deposited at different gas composition.

Therefore, the nanorod growth is supposed to occur in a high O_2 partial pressure with a high temperature to maintain the crystallinity. Figure 4-11 shows the PZT deposited at different Ar:O_2 with a high sputtering temperature of 650. The pressure is 2.7 Pa and deposition time is 2 h. It is shown that a nanorod-like PZT is obtained with Ar:O_2 = 2:1. With respect to the coexistence of perovskite and pyrochlore, it is considered that nanorod array with a much lower density can be obtained if one removes the pyrochlore part in the samples.

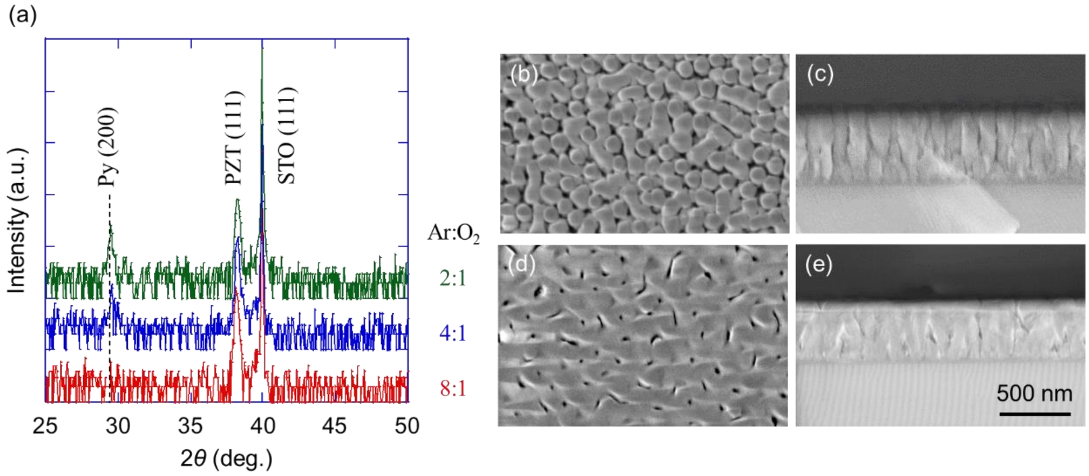

Figure 4-11 Optimization of the sputtering parameters

4.4 Conclusion

The optimal condition of fabricating PZT nanorods by RF-magnetron sputtering is investigated. At the first investigation stage, parameters that seldom affect the free mean path of the sputtered particles, such as Pb content in targets, T–S distance and deposition time are investigated. The optimal conditions used in the second investigation stage are confirmed based on the fact that crystalized perovskite PZT is able to grow epitaxially on STO with a high growth rate as much as possible. Then the parameters related to the free mean path of the sputtered particles, i.e. temperature and pressure, including the O_2 partial pressure, are investigated with respect to the effect on crystallinity, growth rate and the formation of the nanorod structure in details. It is shown that the effect of the O_2 partial pressure plays a considerable important role in growing PZT nanorods, which makes it possible to achieve the nanorod structure at low pressure and thus the rapid growth can be the dominant factor to grow the nanorods by adjusting Ar:O_2. Finally, a nanorod-like PZT is obtained with Ar:O_2 = 2:1 at 650 °C, even though using a general working pressure of 2.7 Pa.

It is unfortunate that the expected nanorod structure has not been realized by RF-magnetron sputtering with the studied conditions, due to the limitation of the used equipment. Nevertheless, the feasibility of growing nanorods can be predicted by the clarifying the effect of the temperature and O_2 pressure in the study. The possibility to achieve nanorods would be enhanced by further increasing the growth rate of sputtering.

4.5 References

76. M. G. Kang, S. M. Oh, W. S. Jung, H. G. Moon, S. H. Baek, S. Nahm, S. J. Yoon, and C. Y. Kang.

Enhanced piezoelectric properties of vertically aligned single-crystalline NKN nano-rod arrays. *Scientific reports*, **5**, 10151 (2015).

77. A. Bose, and M. Sreemany. Influence of processing conditions on the structure, composition and ferroelectric properties of sputtered PZT thin films on Ti-substrates. *Applied Surface Science*, **289**, 551-559 (2014).
78. K. Abe, H. Tomita, H. Toyoda, M. Imai, and Y. Yokote. PZT thin film preparation on Pt-Ti electrode by RF sputtering. *Japanese Journal of Applied Physics*, **30**, 2152 (1991).

Chapter 5 - Theoretical analysis on piezoelectric response of ferroelectric superlattice films

5.1 Introduction

The previous study has revealed the possibility of utilizing the internal stress in the thin films to control the polarization state. However, in an epitaxial film with the thickness over 100 nm, for example, PZT grown on the STO (001) substrate [73], an *a/c*-domained structure is often achieved instead of a single-domain structure, due to the local deformation which is determined by the minimal elastic energy. As a result, it becomes complicated to clarify how the internal stress affects the polarization state in a multidomain structured film.

Before finding out a strategy to experimentally fabricate a single-domain film without local deformation, a single-domain structure can be assumed in a theoretical model and analyzed by the LGD phenomenological theory. The original equation of the elastic Gibbs free energy G is expressed as Eq. (5-1) [79-81],

$$G(\boldsymbol{P},\boldsymbol{\sigma}) = \alpha_1(P_1^2+P_2^2+P_3^2)+\alpha_{11}(P_1^4+P_2^4+P_3^4)+\alpha_{12}(P_1^2P_2^2+P_2^2P_3^2+P_3^2P_1^2)+\alpha_{111}(P_1^6+P_2^6+P_3^6)+\alpha_{112}[P_1^4(P_2^2+P_3^2)+P_2^4(P_3^2+P_1^2)+P_3^4(P_1^2+P_2^2)]+\alpha_{123}(P_1^2P_2^2P_3^2)-\frac{1}{2}s_{11}(\sigma_1^2+\sigma_2^2+\sigma_3^2)-s_{12}(\sigma_1\sigma_2+\sigma_2\sigma_3+\sigma_3\sigma_1)-\frac{1}{2}s_{44}(\sigma_4^2+\sigma_5^2+\sigma_6^2)-Q_{11}(\sigma_1P_1^2+\sigma_2P_2^2+\sigma_3P_3^2)-Q_{12}[\sigma_1(P_2^2+P_3^2)+\sigma_2(P_3^2+P_1^2)+\sigma_3(P_1^2+P_2^2)]-Q_{44}(\sigma_4P_2P_3+\sigma_5P_3P_1+\sigma_6P_1P_2) \tag{5-1}$$

where σ_i and s_{ij} represent stress and elastic compliances, respectively, as mentioned above. a_1 is the dielectric stiffness, a_{ij} and a_{ijk} are higher order stiffness coefficients at constant stress, P_i are the polarization, Q_{ij} are the electrostrictive coefficients. By minimizing G with the given boundary condition, the stabilized polarization state, i.e. the solution for (P_1, P_2, P_3) can be obtained to predict the dielectric and piezoelectric properties of the fully clamped film. In addition, considering the feasibility of achieving this in experiment, a superlattice film, which is known as a periodic structure of (two or more) materials, is also investigated and analyzed theoretically.

In this chapter, two types of PZT, $PbZr_{0.4}Ti_{0.6}O_3$ (tetragonal at room temperature, denoted with T-PZT) and $PbZr_{0.6}Ti_{0.4}O_3$ (rhombohedral at room temperature, denoted with R-PZT) are selected as the studied objects. The (001) and (111) single-layer films are first analyzed to figure out the stabilized polarization state by changing the misfit strain and external electric field. For (111)-oriented films, the coefficients in G will be transformed by rotating the coordinate system. Then the superlattice structure is analyzed and predicted on the dielectric and piezoelectric properties. The coupling effect of the interface between two different materials in the superlattice is also evaluated in this study.

5.2 Model building

5.2.1 Single-layer films

The model of a single-layer film clamped by the substrate is illustrated in Figure 5-1(a). In this model, the residual depolarizing field is neglected due to possible incomplete screening under the assumption that the films are sandwiched between short circuited electrodes [82], which is consistent with experimental results [63]. The sextic polynomial (terms of P^6) in Eq. (5-1) is also neglected for simplifying the calculation. For (111)-oriented films, two sets of the coordinate system are defined, the substrate reference frame denoted with (x, y, z) and the crystallographic frame denoted with (1, 2, 3). According to the relationship illustrated in Figure 5-1(b), it can be understood that x-, y- and z-directions are along the crystal directions of $[\bar{1}10]$, $[\bar{1}\bar{1}2]$ and $[111]$, respectively.

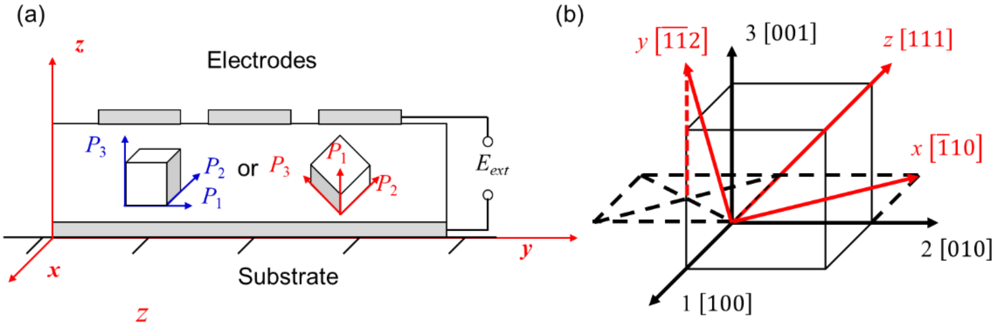

Figure 5-1 (a) Schematic model of a single-layer film clamped by the substrate and (b) the defined coordinate systems corresponding to the crystal directions for (111)-oriented films.

For a clamped epitaxial film, the mechanical boundary condition can be assumed as follows [79,83].

$$\begin{cases} \sigma_{zz} = \sigma_{yz} = \sigma_{xz} = 0 \\ u_{xx} = -\dfrac{\partial G}{\partial \sigma_{xx}} = u_m \\ u_{yy} = -\dfrac{\partial G}{\partial \sigma_{yy}} = u_m \\ u_{xy} = -\dfrac{\partial G}{\partial \sigma_{xy}} = 0 \end{cases} \tag{5-2}$$

In the film, the out-of-plane stresses are all zero, and the in-plane strain is totally determined by the misfit strain u_m between the film and the substrate. The internal elastic fields in the film are homogeneous and thus the above conditions hold throughout the film volume. Since G in (5-1) is associated with the equilibrium thermodynamic state at fixed the stress, the equilibrium potential G_1 for this 2D-clamping case is given by the following Legendre transformation of G.

$$G_1(\boldsymbol{P}, u_m) = G(\boldsymbol{P}, \boldsymbol{\sigma}) + u_{xx}\sigma_{xx} + u_{yy}\sigma_{yy} + 2u_{xy}\sigma_{xy} \tag{5-3}$$

Then the free energy G_2 under the external electric field E_{ext} is expressed as

$$G_2(\boldsymbol{P}, u_m, E_{ext}) = G(\boldsymbol{P}, \boldsymbol{\sigma}) + u_{xx}\sigma_{xx} + u_{yy}\sigma_{yy} + 2u_{xy}\sigma_{xy} - E_{ext}P_z \tag{5-4}$$

5.2.1.1 Expression of the free energy for (001)-oriented films

In the case of the (001) films, the coordinate system (*x,y,z*) is identical to (*1,2,3*). The simultaneous equations can be established with the mechanical conditions given in Eq. (5-2) to solve for the in-plane stresses σ_{xx}, σ_{yy} and σ_{xy}. Then substituting G_2 in Eq. (5-4) with the solved in-plane stresses, the free energy as a function of the polarization, misfit strain as well as the electric field can be expressed as Eq. (5-5), in which the transformed stiffness coefficients are given in Eqs. (5-6)–(5-11). These equations have also been clarified in the previous study [80].

$$G_2^{(001)}(\boldsymbol{P}, u_m, E_{ext}) = \alpha_{1\mathrm{n}}^*(P_1^2 + P_2^2) + \alpha_{3\mathrm{n}}^* P_3^2 + \alpha_{11\mathrm{n}}^*(P_1^4 + P_2^4) + \alpha_{33\mathrm{n}}^* P_3^4 + \alpha_{12\mathrm{n}}^* P_1^2 P_2^2 + \alpha_{13\mathrm{n}}^*(P_1^2 P_3^2 + P_2^2 P_3^2) + G_{0n}(u_m) - P_3 E_{ext} \tag{5-5}$$

where

$$\alpha_{1\mathrm{n}}^* = \alpha_1 - \frac{Q_{11}+Q_{12}}{s_{11}+s_{12}} u_m \tag{5-6}$$

$$\alpha_{3\mathrm{n}}^* = \alpha_1 - \frac{2Q_{12}}{s_{11}+s_{12}} u_m \tag{5-7}$$

$$\alpha_{11\mathrm{n}}^* = \alpha_{11} + \frac{(Q_{11}^2+Q_{12}^2)s_{11} - 2Q_{11}Q_{12}s_{12}}{2(s_{11}^2 - s_{12}^2)} \tag{5-8}$$

$$\alpha_{33\mathrm{n}}^* = \alpha_{11} + \frac{Q_{12}^2}{s_{11}+s_{12}} \tag{5-9}$$

$$\alpha_{12\mathrm{n}}^* = \alpha_{12} - \frac{(Q_{11}^2+Q_{12}^2)s_{12} - 2Q_{11}Q_{12}s_{11}}{s_{11}^2 - s_{12}^2} + \frac{Q_{44}^2}{2s_{44}} \tag{5-10}$$

$$\alpha_{13\mathrm{n}}^* = \alpha_{12} + \frac{Q_{12}(Q_{11}+Q_{12})}{s_{11}+s_{12}} \tag{5-11}$$

$$G_{0\mathrm{n}} = \frac{u_m^2}{s_{11}+s_{12}} \tag{5-12}$$

5.2.1.2 Expression of the free energy for (111)-oriented films

For the (111)-oriented films, coefficients in *G* can be deduced from the coordinate transformation, using a rotation matrix $\boldsymbol{R}$ of the axis angle between the old system and the new system.

$$R_{ij} = \cos\theta_{ij} = \frac{\boldsymbol{n_i}\cdot\boldsymbol{n_j}}{|\boldsymbol{n_i}||\boldsymbol{n_j}|},\ i = x,y,z \text{ and } j=1,2,3, \tag{5-13}$$

where either $\boldsymbol{n_i}$ or $\boldsymbol{n_j}$ represents a vector obtained from the miller indices. Then the matrix $\boldsymbol{R}$ is figured out as

$$\boldsymbol{R} = \begin{pmatrix} cos\theta_{x1} & cos\theta_{x2} & cos\theta_{x3} \\ cos\theta_{y1} & cos\theta_{y2} & cos\theta_{y3} \\ cos\theta_{z1} & cos\theta_{z2} & cos\theta_{z3} \end{pmatrix} = \begin{pmatrix} \frac{-1}{\sqrt{2}} & \frac{1}{\sqrt{2}} & 0 \\ \frac{-1}{\sqrt{6}} & \frac{-1}{\sqrt{6}} & \frac{2}{\sqrt{6}} \\ \frac{1}{\sqrt{3}} & \frac{1}{\sqrt{3}} & \frac{1}{\sqrt{3}} \end{pmatrix} \tag{5-14}$$

Then the coordinate transformation for a vector $\boldsymbol{V} = V_a$, a second-order tensor $\boldsymbol{T_2} = T_{ab}$, a third-order tensor $\boldsymbol{T_3} = T_{abc}$ and a fourth-order tensor $\boldsymbol{T_4} = T_{abcd}$ (a,b,c,d = 1,2,3) can be expressed as follows [84].

$$V_a(\text{new}) = \sum_{i=1}^{3} R_{ai} V_i\,(\text{old}) \tag{5-15}$$

$$T_{ab}(\text{new}) = \sum_{i=1}^{3} R_{ai} \sum_{j=1}^{3} R_{bj}\, T_{ij}(\text{old}) \tag{5-16}$$

$$T_{abc}(\text{new}) = \sum_{i=1}^{3} R_{ai} \sum_{j=1}^{3} R_{bj} \sum_{k=1}^{3} R_{ck}\, T_{ijk}(\text{old}) \tag{5-17}$$

$$T_{abcd}(\text{new}) = \sum_{i=1}^{3} R_{ai} \sum_{j=1}^{3} R_{bj} \sum_{k=1}^{3} R_{ck} \sum_{l=1}^{3} R_{dl}\, T_{ijkl}(\text{old}) \tag{5-18}$$

where "old" and "new" refer to the coordinate system (*1*, *2*, *3*) and (x, y, z), respectively. Similar to the above equations, a vector or a tensor in the "old" system can be deduced from those in the "new" system, using the inverse matrix of $\boldsymbol{R}$ (i.e. $\boldsymbol{R}^{-1}$). Then one can transform the stress tensor with Eq. (5-16) and obtains

$$\begin{cases} \sigma_{11} = \frac{1}{6}(3\sigma_{xx} + 2\sqrt{3}\sigma_{xy} - 2\sqrt{6}\sigma_{xz} + \sigma_{yy} - 2\sqrt{2}\sigma_{yz} + 2\sigma_{zz}) \\ \sigma_{12} = \frac{1}{6}(-3\sigma_{xx} + \sigma_{yy} - 2\sqrt{2}\sigma_{yz} + 2\sigma_{zz}) \\ \sigma_{13} = \frac{1}{6}(-2\sqrt{3}\sigma_{xy} - \sqrt{6}\sigma_{xz} - 2\sigma_{yy} + \sqrt{2}\sigma_{yz} + 2\sigma_{zz}) \\ \sigma_{22} = \frac{1}{6}(3\sigma_{xx} - 2\sqrt{3}\sigma_{xy} + 2\sqrt{6}\sigma_{xz} + \sigma_{yy} - 2\sqrt{2}\sigma_{yz} + 2\sigma_{zz}) \\ \sigma_{23} = \frac{1}{6}(2\sqrt{3}\sigma_{xy} + \sqrt{6}\sigma_{xz} - 2\sigma_{yy} + \sqrt{2}\sigma_{yz} + 2\sigma_{zz}) \\ \sigma_{33} = \frac{1}{3}(2\sigma_{yy} + 2\sqrt{2}\sigma_{yz} + \sigma_{zz}) \end{cases} \tag{5-19}$$

Similarly, each element in the strain tensor has the same form with Eq. (5-19) but noting that a coefficient of 1/2 will be added to the shear strain if using the Voigt notation. Then referring to the case of the (001)-oriented films, the expressions of the in-plane stress σ_{xx}, σ_{yy} and σ_{xy} can be solved as a function of $\boldsymbol{P}$ and u_m and finally Eq. (5-4) can be rewritten as

$$G_2^{(111)}(\boldsymbol{P}, u_m, E_{ext}) = \alpha_1^*(P_1^2 + P_2^2 + P_3^2) + \alpha_1^{**}(P_2P_3 + P_3P_1 + P_1P_2) + \alpha_{11}^*(P_1^4 + P_2^4 + P_3^4) + \alpha_{12}^*(P_1^2P_2^2 + P_2^2P_3^2 + P_3^2P_1^2) + \alpha_{11}^{**}[P_1^3(P_2 + P_3) + P_2^3(P_3 + P_1) + P_3^3(P_1 + P_2)] + \alpha_{12}^{**}P_1P_2P_3(P_1 + P_2 + P_3) + G_0(u_m) - \frac{1}{\sqrt{3}}(P_1 + P_2 + P_3)E_{ext} \tag{5-20}$$

where coefficients of deduced dielectric stiffness are listed below.

$$\alpha_1^* = \alpha_1 - \frac{4(Q_{11}+2Q_{12})}{4s_{11}+8s_{12}+s_{44}}u_m \tag{5-21}$$

$$\alpha_1^{**} = \frac{2Q_{44}}{4s_{11}+8s_{12}+s_{44}}u_m \tag{5-22}$$

$$\alpha_{11}^* = \alpha_{11} + \frac{Q_{11}^2(2s_{11}+2s_{12}+s_{44})-2Q_{11}Q_{12}(4s_{12}-s_{44})+Q_{12}^2(4s_{11}+3s_{44})}{(4s_{11}+8s_{12}+s_{44})(s_{11}-s_{12}+s_{44})} \tag{5-23}$$

$$\alpha_{12}^* = \alpha_{12} + \frac{-2Q_{11}^2(4s_{12}-s_{44})+4Q_{11}Q_{12}(4s_{11}+3s_{44})+2Q_{12}^2(4s_{11}-8s_{12}+5s_{44})+Q_{44}^2(3s_{11}+5s_{12}+s_{44})}{2(4s_{11}+8s_{12}+s_{44})(s_{11}-s_{12}+s_{44})} \tag{5-24}$$

$$\alpha_{11}^{**} = -\frac{[Q_{11}(2s_{11}+2s_{12}+s_{44})-Q_{12}(4s_{12}-s_{44})]Q_{44}}{(4s_{11}+8s_{12}+s_{44})(s_{11}-s_{12}+s_{44})} \tag{5-25}$$

$$\alpha_{12}^{**} = \frac{[(2Q_{11}-Q_{44})(s_{11}+3s_{12})-2Q_{12}(2s_{11}+2s_{12}+s_{44})]Q_{44}}{(4s_{11}+8s_{12}+s_{44})(s_{11}-s_{12}+s_{44})} \tag{5-26}$$

$$G_0(u_m) = \frac{6u_m^2}{4s_{11}+8s_{12}+s_{44}} \tag{5-27}$$

5.2.2 Superlattice films with two types of PZT

A superlattice film usually consists of several layers with different compositions. In this superlattice model, it is assumed that two types of PZT, i.e. T-PZT and R-PZT, are alternatively deposited on the (111)-oriented substrates and the thickness of each layer is the same. To deduce the total free energy of the superlattice film, the model is equivalent to a bilayer film, in which either T-PZT or R-PZT layer takes up half of the volume as shown in Figure 5-2(a). The external electric field is as defined in the model of the single-layer films. Of note, the misfit strain for one layer is unequal to the other layer due to the different lattice constant. Various misfit strains are defined as shown in Figure 5-2(b). The misfit strain is denoted as u_{mT} in the T-PZT layer and u_{mR} in the R-PZT layer, and u_{m} is used as the average misfit strain of the superlattice film.

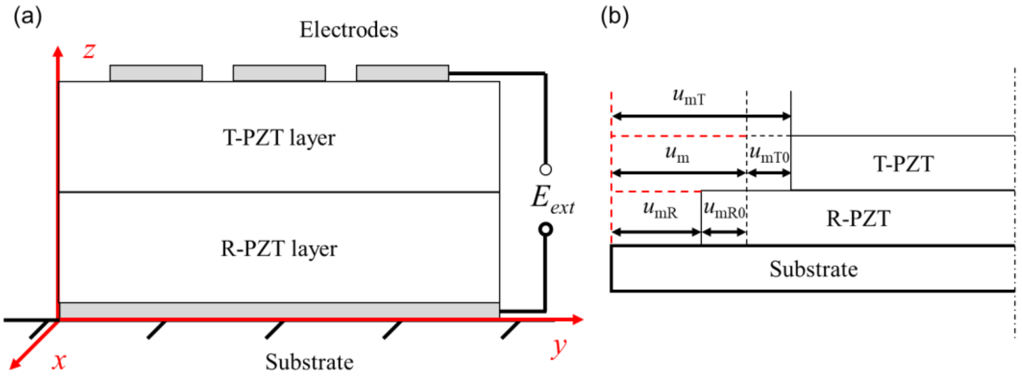

Figure 5-2 (a) Schematic model of a (111)-oriented superlattice film clamped by the substrate and (b) the various misfit strain

In addition, the depolarization field in either layer cannot be neglected due to the interaction of the polarization at the interface. Thus the total free energy of one layer is expressed as

$$G_3(\boldsymbol{P}, u_m, E_{ext}, \kappa) = G_2(\boldsymbol{P}, u_m, E_{ext}) - \frac{1}{2} E_D P_z \tag{5-28}$$

where E_{D} represents the depolarizing field caused by the possible incomplete screening. Hereafter, to distinguish the parameters in one layer from the other, the subscript "T" and "R", representing the T-PZT layer and R-PZT layer, respectively, are added to the parameters. Since the electric field must be continuous at the interface and the surface, E_{D} in the two layers should be related as follows.

$$\begin{cases} \kappa P_{zT} + \varepsilon_0 E_{DT} = \kappa P_{zR} + \varepsilon_0 E_{DR} \\ E_{DT} + E_{DR} = 0 \end{cases} \tag{5-29}$$

which gives

$$E_{DT} = -E_{DR} = -\frac{\kappa}{2\varepsilon_0}(P_{zT} - P_{zR}) \tag{5-30}$$

Here, κ $(0 \le \kappa \le 1)$ describes the coupling strength of the depolarization field caused by the possible interfacial localized charges [85]. For example, $\kappa = 1$ corresponds to a defect-free, perfectly insulating interface and $\kappa = 0$ indicates that the polarization of either layer is completely screened by interfacial localized charges.

Therefore, the total free energy of the superlattice film can be expressed by the average G_3 of the T-PZT and R-PZT layers as follows.

$$\tilde{G}(\boldsymbol{P_T}, \boldsymbol{P_R}, u_{mT}, u_{mR}, E_{ext}, \kappa) = \frac{1}{2}(G_{3T} + G_{3R}) \tag{5-31}$$

Then the polarization state with given u_m, E_{ext} and κ can be obtained by minimizing $\tilde{G}$ through the following system of equations.

$$\frac{\partial \tilde{F}}{\partial P_i} = 0 \ \ (i = 1T, 2T, 3T, 1R, 2R, 3R) \tag{5-32}$$

The possible equilibrium polarization states have been identified by Pertsev et al. [79,81] as follows, which are listed as follows and used for the later discussion.

(1) Paraelectric phase: $P_1 = P_2 = P_3 = 0$

(2) *a* phase: $P_1 \neq 0, P_2 = P_3 = 0$

(3) *c* phase: $P_1 = 0, P_2 = 0, P_3 \neq 0$

(4) *ac* phase: $P_1 \neq 0, P_2 = 0, P_3 \neq 0$

(5) *aac* phase: $P_1 = P_2 \neq 0, P_3 \neq 0$

(6) *r* phase: $P_1 = P_2 = P_3 \neq 0$

5.3 Results and discussion

5.3.1 u_m-E_{ext} phase diagrams for single-layer films and the superlattice film

The stabilized polarization state, determined by Eq. (5-5) for (001) film and Eq. (5-20) for (111) films and changed with u_m and E_{ext}, gives the u_m-E_{ext} phase diagrams. Table 5-1 lists the involved parameters for calculation. The values of the elastic compliances, stiffness coefficients and electrostrictive coefficients are obtained from Haun's literature [56,58]. The lattice constants of T-PZT and R-PZT are referred to the study of Pertsev *et al.* [86].

Table 5-1 Values of involved parameters of T-PZT and R-PZT for calculation [56,58,86]

	Lattice constant		α_1	α_{11}	α_{12}	Q_{11}	Q_{12}	Q_{44}	s_{11}	s_{12}	s_{44}
	a (Å)	c (Å)	$(10^7\ \ m/F)$ at 25°C	$(10^7\ \ m^5/C^2F)$		$(10^{-2}\ \ m^4/C^2)$			$(10^{-12}\ \ m^2/N)$		
T-PZT	4.04	4.14	-8.34	3.614	32.33	8.116	-2.95	6.71	8.6	-2.8	21.2
R-PZT	4.08	4.08	-7.904	13.62	23.91	7.26	-2.708	6.293	8.8	-2.9	24.6

Figure 5-3 and Figure 5-4 show the comparison of T-PZT and R-PZT on the u_m-E_{ext} phase diagrams. For the (001)-oriented films shown in Figure 5-3, the films mainly possess *c* phase or *aac* phase. In the region of a tensile strain over 0.005, *aa* phase, that is known as an in-plane polarization state, is stabilized at $E_{ext} = 0$, and tends to change to *aac* phase immediately when the external electric field is applied. Since the *aa-aac* phase transition is a second-order transition, it would be difficult to utilize the polarization rotation to achieve large piezoelectric response in this region.

For the (111)-oriented films, shown in Figure 5-4, *aac* phase or *r* phase may exist in the u_m range from -0.01 to 0.01. The directions of these phases are illustrated in Figure 5-5. The *r*-phase has an out-of-plane direction, while the *aac*-phase has a tilted direction which is different from the polarization state in PZT bulks. Of note, for T-PZT with u_m = -5–3 × 10^{-3} and R-PZT with u_m = 1–10 × 10^{-3}, phase transition from *aac* phase to *r* phase occurs when the external electric field is applied, indicating that the piezoelectric properties of these films would be enhanced by utilizing this transition. In addition, considering to achieve the large electric field induced strain at low applied voltage, u_m need to be set to 0.001 for R-PZT and -0.005 for T-PZT.

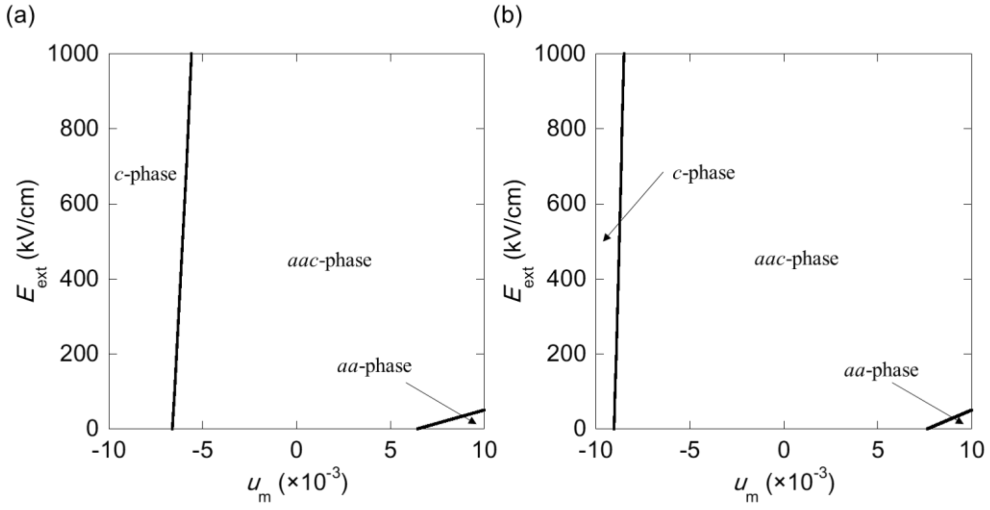

Figure 5-3 Comparison of (001)-oriented (a) T-PZT and (b) R-PZT on the u_m-E_{ext} phase diagrams.

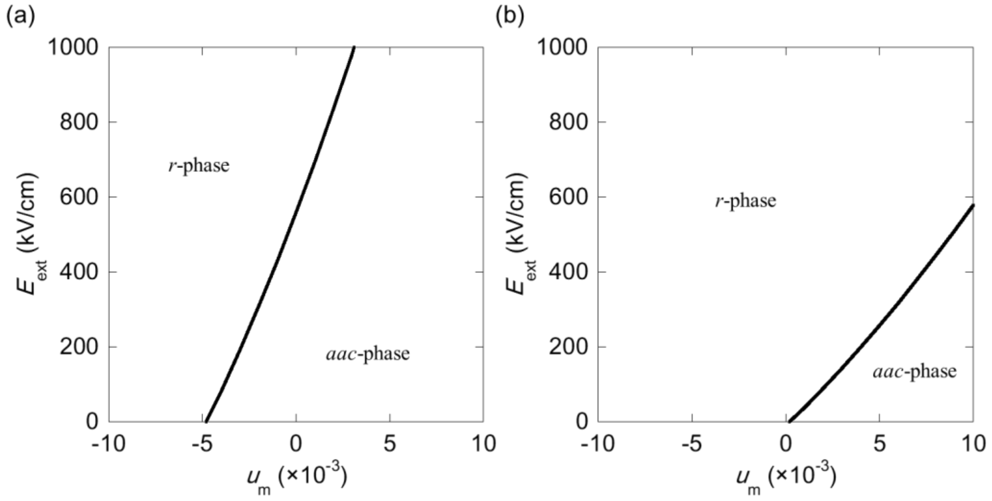

Figure 5-4 Comparison of (111)-oriented (a) T-PZT and (b) R-PZT on the u_m-E_{ext} phase diagrams.

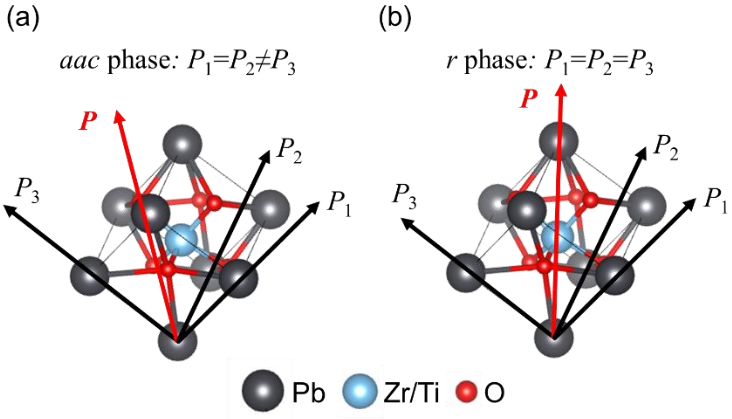

Figure 5-5 Stabilized polarization states in the (111)-oriented films. (a) *aac*-phase, (b) *r*-phase.

According to the calculated u_m-E_{ext} phase diagrams, it is indicated that the polarization rotation can be utilized by achieving a desired strain or stress state in the single-domain films, especially for the (111)-oriented films. However, as discussed above, it is difficult to form a single-domain structure in a single-layer film with the thickness over 100 nm. Thus using the superlattice structure is necessary for utilizing the polarization rotation. In the next discussion, the studied object will focus on the superlattice film consisting of (111) T-PZT and (111) R-PZT. Deduced from Eq. (5-31), $\tilde{G}$ can be expressed more explicitly as

$$\tilde{G}(\boldsymbol{P_T},\boldsymbol{P_R},u_{mT},u_{mR},E_{ext},\kappa)=\frac{1}{2}\left[G_{1T}^{(111)}(\boldsymbol{P_T},u_{mT},E_{ext})+G_{1R}^{(111)}(\boldsymbol{P_R},u_{mR},E_{ext})\right]+\frac{\kappa}{24\varepsilon_0}[(P_{1T}+P_{2T}+P_{3T})-(P_{1R}+P_{2R}+P_{3R})]^2 \tag{5-33}$$

where $G_{1T}^{(111)}$ and $G_{1R}^{(111)}$ are expressed by Eq. (5-20). Then theoretical analysis is able to compare with the experimental result. Figure 5-6 shows the u_m-E_{ext} phase diagram of the T-PZT and R-PZT layers in the (111) superlattice film, for the cases of $\kappa = 0$, 0.01 and 1. For $\kappa = 0$, the phase transition boundary is the case of the single-layer films, indicating that T-PZT and R-PZT layers are decoupled with each other. When κ increases, the position and slope of the phase transition boundaries are slightly changed, indicating that the effect of the electrostatic boundary condition is much smaller than that of the mechanical boundary condition.

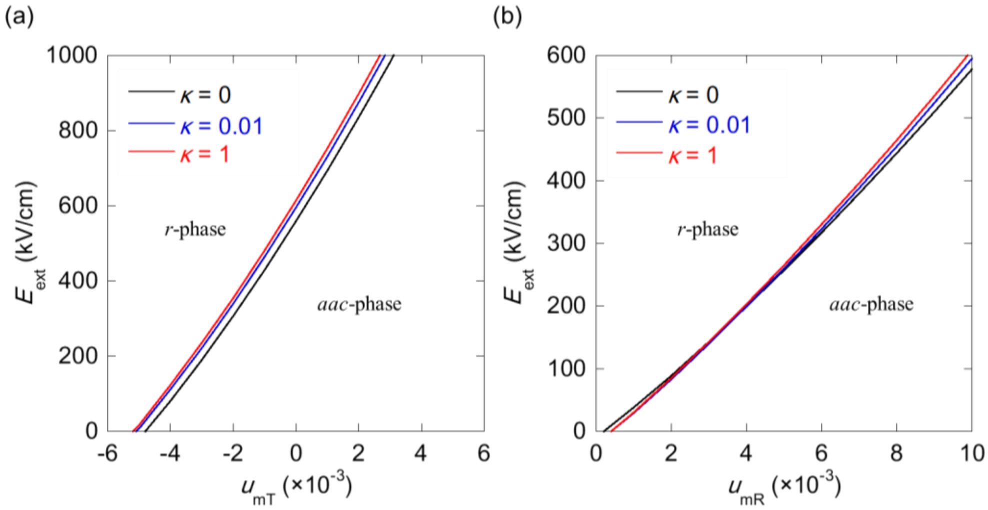

Figure 5-6 u_m-E_{ext} phase diagrams depended on κ in the superlattice films. (a) T-PZT layers and (b) R-PZT layers.

5.3.2 Polarization state for the superlattice film

When plotting the u_m-E_{ext} phase diagrams, one calculates the stabilized polarization state. Here, the polarization state is described based on the (x,y,z) system, using the coordinate transformation given in Eq. (5-15). Figure 5-7 shows the polarization state depended on u_m at $E_{ext} = 0$. In the (x,y,z) coordinate system, *r* phase has the polarization vector normal to the substrate ($P_x = P_y = 0, P_z \neq 0$) and *aac* phase has the tilted polarization vector away from the z-direction ($P_x \neq 0, P_y = 0, P_z \neq 0$). Thus, the polarization state shown in Figure 5-7 agrees with the phase diagram shown in Figure 5-4. In addition, it is shown that P_z increases while P_x decreases when enlarging the compressive strain, and vice versa. It is consistent with the fact that the direction of the polarization vector will turn to the stretching direction of the film.

Figure 5-8 shows the polarization state depended on E_{ext} at $u_m = 0$ and 0.003. Due to the trend of the electric field induced *aac*-*r* transition, P_z increases while P_x decreases when E_{ext} becomes large. The discontinuous change of P_z and P_x at the phase boundary indicates that the polarization rotation from *aac* phase to *r* phase is the first-order phase transition. Of note, in the case of $u_m = 0.003$, the polarization rotation occurs in both T-PZT and R-PZT films, which can be utilized to enhance the piezoelectric properties.

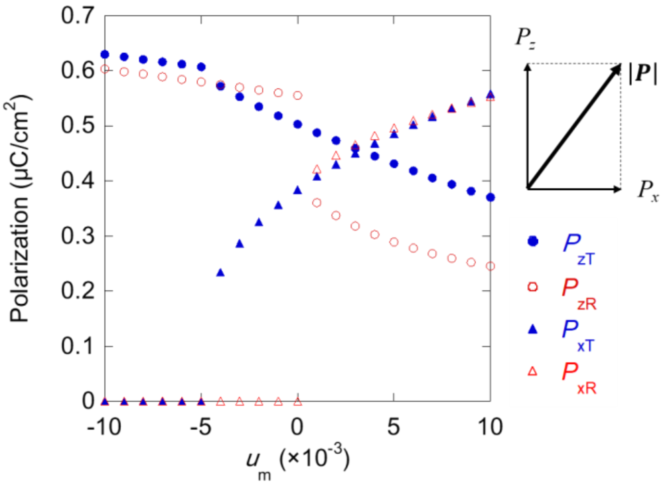

Figure 5-7 The stabilized polarization state depended on u_{m} at $E_{\mathrm{ext}} = 0$

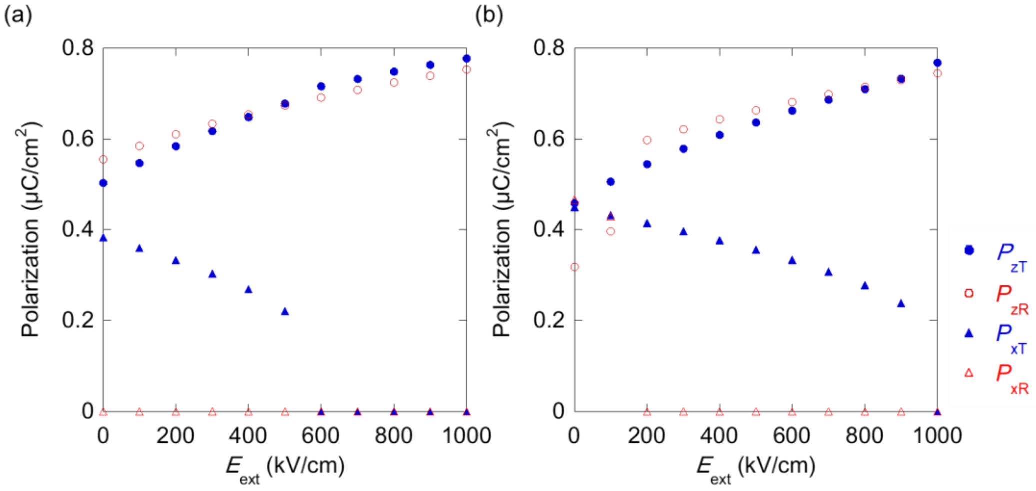

Figure 5-8 The stabilized polarization state depended on E_{ext} at (a) $u_{\mathrm{m}} = 0$ and (b) $u_{\mathrm{m}} = 0.003$.

The effect of κ on P_z and P_x is shown in Figure 5-9 and Figure 5-10, respectively, at $E_{\mathrm{ext}} = 0$ and $u_{\mathrm{m}} = 0$ and 0.003. As κ increases, P_z of T-PZT and R-PZT become close to each other and the average polarization increases slightly. For the case of $u_{\mathrm{m}} = 0.003$ where the phase transition occurs in both T-PZT and R-PZT, the change of P_z become clearer than that at $u_{\mathrm{m}} = 0$. It is indicated that the effect of κ on the polarization rotation is much smaller than that of the mechanical condition, but κ plays an important role in affecting the polarization extension. In addition, κ does not affect P_x which agrees with the assumption that the coupling effect only occurs in the z-direction.

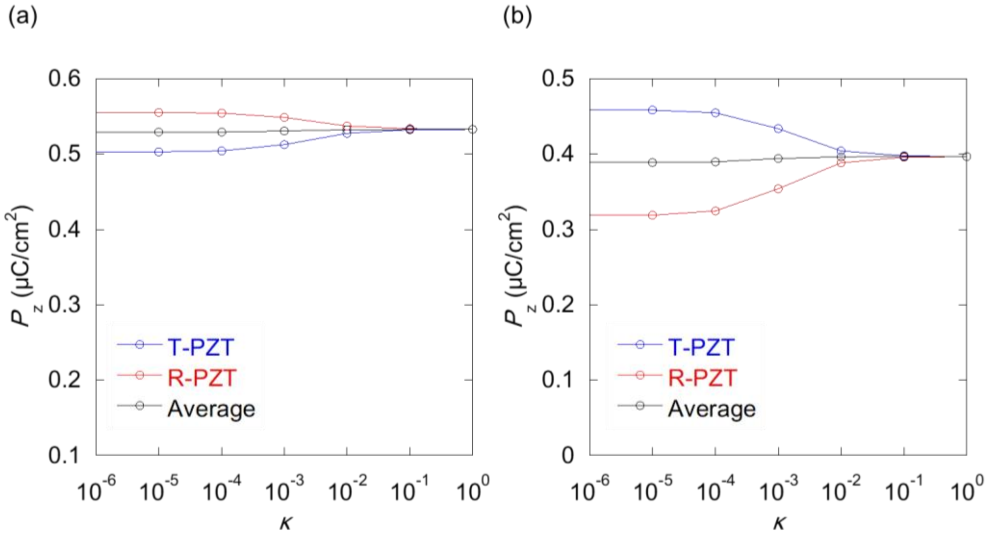

Figure 5-9 The effect of κ on P_z at (a) $u_m = 0$ and (b) $u_m = 0.003$

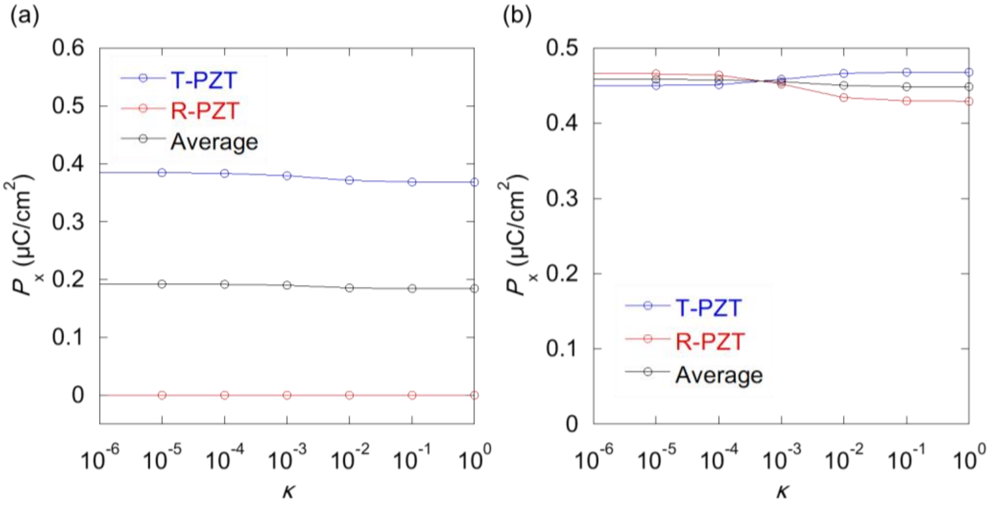

Figure 5-10 The effect of κ on P_x at (a) $u_m = 0$ and (b) $u_m = 0.003$

5.3.3 Dielectric constant of single-layer films

The dielectric constant depended on u_m and E_{ext} is analyzed with the following equation [58].

$$\frac{\partial^2 G}{\partial P_z^2} = \frac{1}{\varepsilon_{33}} = \frac{1}{\varepsilon_0 \varepsilon_r} \tag{5-34}$$

Here, ε_r is calculated with the stabilized polarization state that is deduced from the total free energy $\tilde{G}$, while G in which the depolarization energy and polarization energy from E_{ext} are neglected is used for the expression of ε_r. Figure 5-11 shows the relative dielectric constant ε_r depended on u_m at $E_{ext} = 0$. At the *aac*-*r* phase phase transition boundary, ε_r obtains a discontinuous change and increases as a tensile u_m is applied. Of note, ε_r of R-PZT decreases after the phase transition and continuing applying the tensile strain.

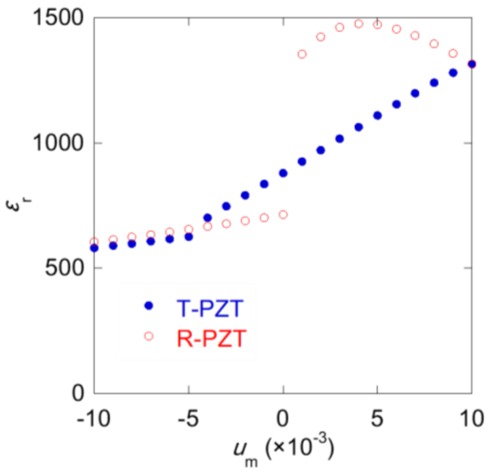

Figure 5-11 The dielectric constant depended on u_m at $E_{ext} = 0$

Figure 5-12 shows the relative dielectric constant ε_r depended on E_{ext}. It is shown the decreased ε_r with the increase of E_{ext}, which is beneficial to the enhancement of FOM. Discontinuous change of ε_r at the *aac*-*r* phase transition point, agreeing with the first-order transition of the polarization state. In addition, the change of ε_r for R-PZT is clearer than that for T-PZT.

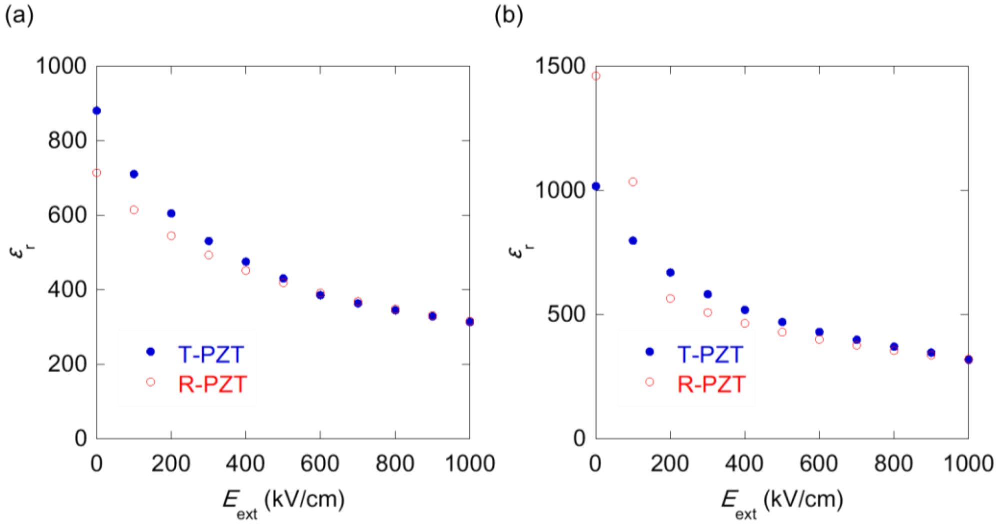

Figure 5-12 The dielectric constant depended on E_{ext} at (a) $u_m = 0$, (b) $u_m = 0.003$

5.3.4 Piezoelectric response of single-layer films and superlattice films

In a fabricated superlattice film, u_{mT} and u_{mR} are different due to the different lattice constants of T-PZT layers and R-PZT layers. Specifically, a tensile strain in T-PZT and a compressive strain in R-PZT if not considering the effect of the substrate. The misfit strain induced at the interface of the PZT layers can be approximately estimated as

$$u_{mT0} = -u_{mR0} = -\frac{a_{0T}-a_{0R}}{a_{0T}+a_{0R}} \tag{5-35}$$

where $a_{0\mathrm{T}}$ and $a_{0\mathrm{R}}$ stand for average lattice constant when assuming T-PZT and R-PZT as a cubic crystal, and the expressions for them are given as follows.

$$a_0 = \sqrt[3]{abc} \quad \Rightarrow \quad \begin{cases} a_{0T} = \sqrt[3]{a_T a_T c_T} \\ a_{0R} = a_R \end{cases} \tag{5-36}$$

The values of a_T, c_T and a_R are obtained in Table 5-1. Since the piezoelectric constant is not a linear function of E_{ext} due to the polarization rotation, the evaluation of the piezoelectric response should be reflected by the electric field induced strain instead of directly calculating the piezoelectric constants. Thus the 33 response can be evaluated by

$$\Delta u_{zz} = Q_{zzzz}(P_z^2 - P_r^2) \tag{5-37}$$

where P_{r} represents the remanent P_z (i.e. P_z at E_{ext}=0) and Q_{zzzz} the electrostrictive coefficient in the (x,y,z) coordinate system, which can be deduced from the second derivative of u_{zz} with respect to P_{z} [39], or using Eq. (5-18) to transform $\boldsymbol{Q}$ in the $(1,2,3)$ coordinate system.

$$Q_{zzzz} = -\frac{1}{2}\frac{\partial^2 u_{zz}}{\partial P_z^2} = \frac{s_{44}(Q_{11}+2Q_{12})+2(s_{11}+2s_{12})Q_{44}}{4s_{11}+8s_{12}+s_{44}} \tag{5-38}$$

With respect to the 31 response, it is difficult to evaluate the induced in-plane strain due to the clamping effect. Instead, one uses the induced in-plane stress and thus evaluate piezoelectric stress constant e_{31} referring to the approach of evaluating the 33 response. Thus

$$\Delta\sigma_{xx} = q_{zzxx}(P_z^2 - P_r^2) \tag{5-39}$$

where q_{zzxx} is proportional to the second derivative of σ_{xx} with respect to P_{z}.

$$q_{zzxx} = -\frac{1}{2}\frac{\partial^2 \sigma_{xx}}{\partial P_z^2} = \frac{2Q_{11}+4Q_{12}-Q_{44}}{4s_{11}+8s_{12}+s_{44}} \tag{5-40}$$

5.3.4.1 Evaluation of the d_{33} response

Figure 5-13 shows the dependence of Δu_{zz} on E_{ext} for (111)-oriented PZT bulks, (111)-oriented single-layer films and superlattice films. u_{m} and κ are both set to zero. Here the bulks are assumed to be clamped, i.e. the same mechanical boundary condition as the films, without considering the electric field induced phase transition. Thus their Δu_{zz} can be directly expressed with $\Delta u_{zz} = d'_{33}E_{ext}$, where d'_{33} is expressed by Eq. (2-24) with all parameters in the (111) direction. The piezoelectric constant $\boldsymbol{d}$ and the elastic compliance $\boldsymbol{s}$ in the (111) orientation can be figured out with Eq. (5-17) and Eq. (5-18), respectively. The calculation result is shown in Table 5-2 and Table 5-3.

Table 5-2 The calculated piezoelectric constant in the (111) orientation, derived from the (001) orientation

	In the (001) orientation $(10^{-12}$ pm/V)			In the (111) orientation $(10^{-12}$ pm/V)			
	d_{33}	d_{31}	d_{15}	d_{33}	d_{31}	d_{32}	d'_{33}
T-PZT	162	-58.9	169	73.6	-34.0	-14.0	53.1
R-PZT	189	-80.5	60	71.0	-11.2	-11.2	61.4

Table 5-3 The calculated elastic compliance in the (111) orientation, derived from the (001) orientation

	In the (001) orientation $(10^{-12}\ \mathrm{Pa}^{-1})$			In the (111) orientation $(10^{-12}\ \mathrm{Pa}^{-1})$	
	s_{11}	s_{12}	s_{44}	s_{11}	s_{12}
T-PZT	8.6	-2.8	21.2	8.2	-2.7
R-PZT	8.8	-2.9	24.6	9.1	-3.0

Comparing with the clamped bulks shown in Figure 5-13, the piezoelectric response of the R-PZT clamped film is comparable to the bulks, while the T-PZT film show a higher piezoelectric constant due to the *aac-r* phase transition. The superlattice film also shows an enhanced piezoelectric response comparing to the bulks. Of note, there is a discontinuous change of the slope for the T-PZT film around E_{ext} = 600 kV/cm and for the superlattice film around E_{ext} = 700 kV/cm, which is in accordance with the phase diagram shown in Figure 5-4.

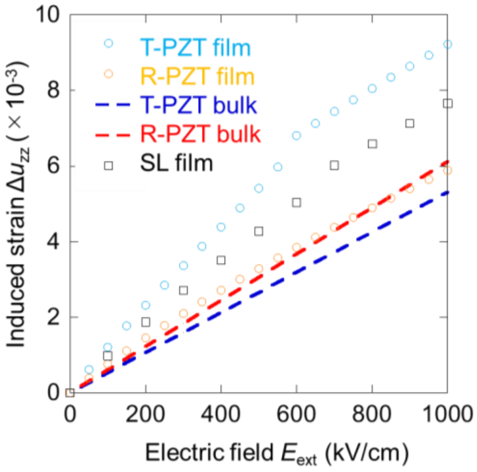

Figure 5-13 Dependence of the induced strain on the external electric field, with respect to (111)-oriented PZT bulks, single-layer films and superlattice films. u_{m} and κ are set to zero.

The effect of u_{m} on the piezoelectric response of the superlattice films is further clarified by Figure 5-14(a). Although there is no *aac-r* phase transition in the film with u_{m} = 0 at low E_{ext}, the piezoelectric response is larger than the clamped bulks, due to the *aac* phase stabilized in the film. Improved piezoelectric properties were found on the conditions of u_{m} = -0.005 or u_{m} = 0.003, which agree with the T-PZT and R-PZT transition points, respectively, as shown in Figure 5-14(b). d_{33} of the superlattice films with such u_{m} can be as high as 200 pC/N, showing the significance of adjusting the internal stress in the ferroelectric films.

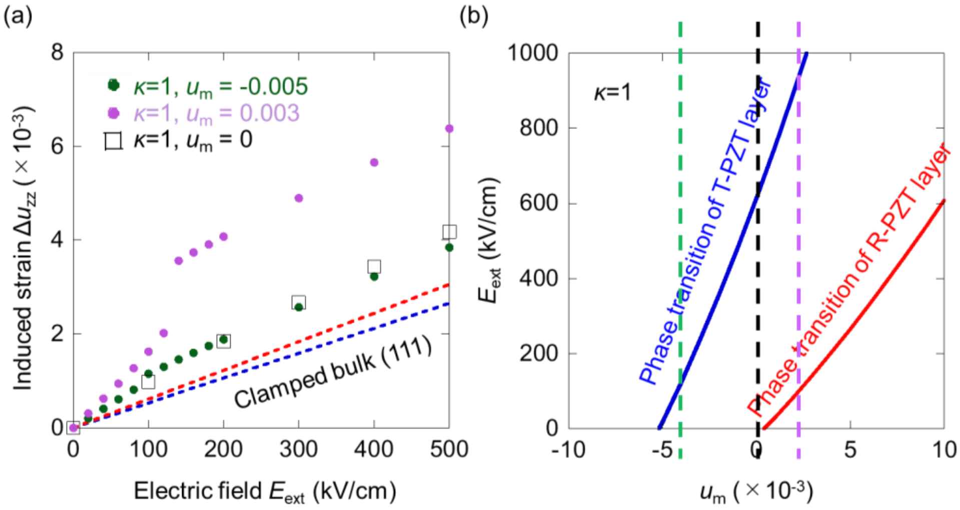

Figure 5-14 Dependence of the induced strain on the external electric field, with respect to the superlattice films with different u_m.

5.3.4.2 Evaluation of the e_{31} response

For the (111)-oriented bulks, e_{31} can be calculated with the following equation [87], with the values given in Table 5-2 and Table 5-3.

$$e_{31} = \frac{d_{31}}{s_{11}+s_{12}} \tag{5-41}$$

Then one can estimate the result of e_{31} = -4.37 C/m^2 for T-PZT and e_{31} = -1.85 C/m^2 for T-PZT. The 31 response of the bulk can be plotted with the relationship $\Delta\sigma_{xx} = e_{xzz}E_{ext}$ as shown in Figure 5-15. It is shown that the superlattice film has the average e_{31} of T-PZT and R-PZT, due to the phase transition only in T-PZT at u_m = 0. However, for the superlattice film with u_m = 0.003 shown in Figure 5-16, a large 31 response is obtained due to the phase transition in the R-PZT layer, and even higher than that of the bulk. The enhanced piezoelectric response in such superlattice films indicates a promising use for the PEH application.

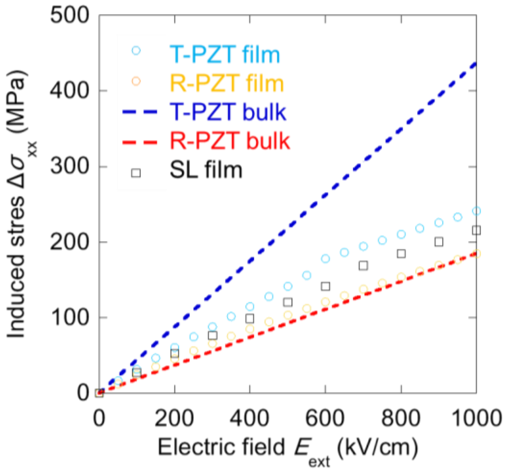

Figure 5-15 Dependence of the induced in-plane stress on the external electric field, with respect to (111)-oriented PZT bulks, single-layer films and superlattice films. u_m and κ are set to zero.

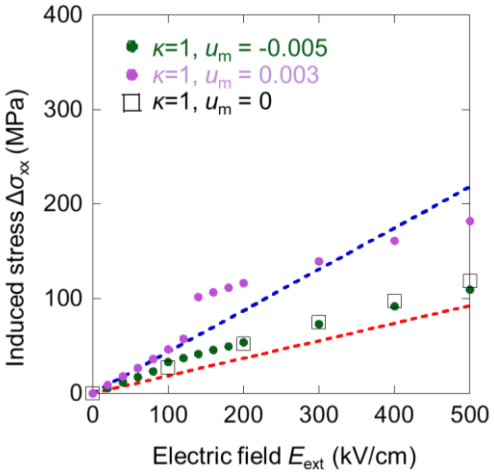

Figure 5-16 Dependence of the induced stress on the external electric field, with respect to the superlattice films with different u_m.

5.4 Conclusion

The possibility of utilizing the lateral stress to control the polarization rotation is predicted with the LGD phenomenological theory, with respect to the single-domain structure in the single-layer film and the superlattice film. u_m-E_{ext} phase diagrams of the single-layer films confirm this possibility, and detailed analyses on the stabilized polarization, dielectric and piezoelectric properties of the (111)-oritened superlattice films reveal the potential of exhibiting enhanced piezoelectric response. The following conclusion is also obtained in this study.

1) Phase transition from *aac* phase to *r* phase in (111)-oriented PZT films. Especially for T-PZT with a tetragonal phase in the bulk, the domain structure changed to a total different state with the induced stress normal to the (111) direction.

2) Discontinuous change of P_z, ε_r, d_{33} and e_{31} at the phase transition boundary. The polarization in the *z* direction and piezoelectric constant are increased and the dielectric constant is decreased with the electric field-induced phase transition, which is beneficial to enhance FOM of the superlattice films.

3) Small enhancement by increasing κ, compared with the effect of mechanical conditions. Although the coupling strength affects a little on the electrical and electromechanical properties, but affects greatly on forming a single-domain structured film which can be clearly shown from the experimental results in the later section.

5.5 References

79. N. A. Pertsev, A. G. Zembilgotov, and A. K. Tagantsev. Effect of mechanical boundary conditions on phase diagrams of epitaxial ferroelectric thin films. *Physical Review Letters*, **80**, 1988 (1998).
80. Z. G. Ban and S. P. Alpay. Phase diagrams and dielectric response of epitaxial barium strontium titanate films: A theoretical analysis. *Journal of Applied Physics*, **91**, 9288-9296 (2002).
81. Z. G. Ban, S. P. Alpay. Optimization of the tunability of barium strontium titanate films via epitaxial stresses. *Journal of Applied Physics*, **93**, 504-511 (2003).
82. M. Mtebwa, A. K. Tagantsev, T. Yamada, P. Gemeiner, B. Dkhil, and N. Setter. Single-domain (110) $PbTiO_3$ thin films: Thermodynamic theory and experiments. *Physical Review B*, **93**, 144113 (2016).
83. A. K. Tagantsev, N. A. Pertsev, P. Muralt, and N. Setter. Strain-induced diffuse dielectric anomaly and critical point in perovskite ferroelectric thin films. *Physical Review B*, **65**, 012104 (2001).
84. J. Ouyang, and A. L. Roytburd. Intrinsic effective piezoelectric coefficients of an epitaxial ferroelectric film. *Acta Materialia*, **54**, 531-538 (2006).
85. M. B. Okatan, J. V. Mantese, and S. P. Alpay. Polarization coupling in ferroelectric multilayers. *Physical Review B*, **79**, 174113 (2009).
86. N. A. Pertsev, V. G. Kukhar, H. Kohlstedt, and R. Waser. Phase diagrams and physical properties of single-domain epitaxial $Pb(Zr_{1-x}Ti_x)O_3$ thin films. *Physical Review B*, **67**, 054107 (2003).
87. A. Mazzalai, D. Balma, N. Chidambaram, L. Jin, and P. Muralt. Simultaneous piezoelectric and ferroelectric characterization of thin films for MEMS actuators. *In 2013 Joint IEEE International Symposium on Applications of Ferroelectric and Workshop on Piezoresponse Force Microscopy (ISAF/PFM)*, 363-366 (2013).

Chapter 6 - Large piezoelectric response from polarization rotation in artificial superlattice films

6.1 Introduction

The theoretical analysis has predicted the enhanced piezoelectric property by achieving a desired misfit strain to induce the polarization rotation in a single-domain film. However, realizing this prediction is difficult because a thermal strain may cause a multidomain structure in the epitaxial films with the thickness over 100 nm during cooling after high temperature deposition [88]. In order to deal with these problems, fabricating artificial superlattice films would be a promising approach to achieving improved ferroelectric and piezoelectric properties. Yadav et al. [89,90] reported that the superlattice films consisting of ferroelectric $PbTiO_3$ and paraelectric STO on $DyScO_3$ form the unique domain state so-called polar vortices in $PbTiO_3$ layer when certain superlattice periods. The formation of polar vortices can be achieved by the balance of elastic, electrostatic and gradient energies; thus, the polarization state can be expected to be sensitively varied by the eternal field [91]. Another example of superlattice films is of two different compositions of ferroelectric PZT, which are in tetragonal and rhombohedral phases at room temperature in bulk. One recently found that these (111) films on $SrTiO_3$ with each layer below 5 nm thickness apparently formed single domain structures in each layer and showed the increased piezoelectric response, which is seldom seen in the single-layer films [92].

In this chapter, (111)-epitaxial artificial superlattice films consisting of $Pb(Zr_{0.4}Ti_{0.6})O_3$ and $Pb(Zr_{0.6}Ti_{0.4})O_3$ were fabricated by PLD, which is in accordance with the theoretical model. The fabricated films with the layer thickness of 24, 12 and 3 nm are characterized on (1) the crystallinity and periodicity of the structure, (2) the domain structure and polarization state, and evaluated on (3) the piezoelectric property with comparison of the theoretical result.

6.2 Experimental

Figure 6-1 shows the schematic structure of the fabricated films. T-PZT and R-PZT, standing for $Pb(Zr_{0.4}Ti_{0.6})O_3$ and $Pb(Zr_{0.6}Ti_{0.4})O_3$, respectively, were deposited alternatively on (111)-oriented $SrTiO_3$ substrates. PZT ceramic targets were sintered by spark plasma sintering, containing 5%-excess PbO in order to achieve the stoichiometric lead composition during the lead evaporation in PLD. The fabrication parameters are listed in Table 6-1. Similar to the fabrication in Chapter 3, a laser energy of 59.4 mJ with a repetition rate of 7 Hz was used in PLD. The oxygen pressure was set to 200 mTorr. Before growing the PZT nanorods, SRO bottom electrode layers with a thickness of 30 nm were deposited on STO at 700°C with 200 mTorr of O2 via PLD. After the fabrication of the PZT films, 100-µm diameter Pt top electrodes were deposited by EBV. As a result, the total thickenss of the superlattice films is 240 nm, with the layer thickness of 3, 12 and 24 nm in this study.

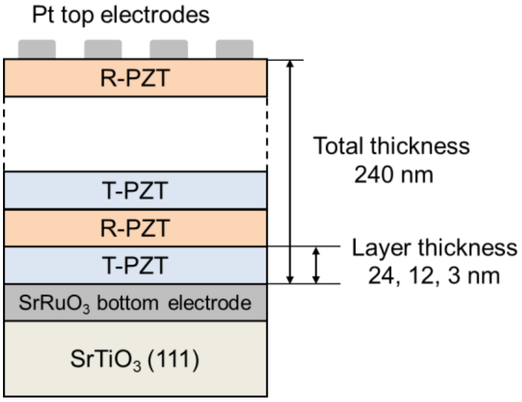

Figure 6-1 Schematic illustration of the fabricated artificial superlattice PZT films

Table 6-1 Fabrication parameters of each part in the superlattice films

	Method	Material	Temperature (°C)	Pressure (mTorr)	Energy / Current	Thickness (nm)
Bott. electrode	PLD	$SrRuO_3$	700	200	59.4 mJ, 10 Hz	30
T-PZT R-PZT	PLD	PZT	625	200	59.4 mJ, 7 Hz	240
Top electrode	EBV	Pt	RT	$<10^{-4}$	200 mA	30

The crystallinity, orientation and periodicity of the fabricated superlattice films were characterized by XRD using four-axis diffractometers with Cu Kα1 X-rays (Bruker D8 Discover). Atomic-resolution structures of the films were analyzed using annular bright-field scanning transmission electron microscopy (ABF-STEM) and high-angle annular dark field STEM (HAADF-STEM) (JEOL JEM-ARM200F Cold FEG) operated at 200 kV. It has been reported that the orientation of the polarization can be figured out by characterizing the position of the A-site and B-site atoms in the perovskite structure [89]. The ferroelectric property was measured with a ferroelectric tester (Toyo FCE-1). The piezoelectric response of each layer in the superlattice films was characterized by the change in the XRD peak profile under the application of short-voltage pulses using time-resolved synchrotron XRD system (SPring-8, BL13XU beamlines, Japan), with the photon energy of 12.4 keV (wavelength of 0.1 nm). The piezoelectric constant d_{33} of the total films were characterized by piezoresponse force microscopy (PFM).

6.3 Results and discussion

6.3.1 Crystallinity, periodicity and the polarization state of superlattice films

Figure 6-2 shows the XRD patterns of the fabricated films with the layer thickness of 24, 12 and 3 nm. For convenient discussion, one named them with SL24, SL12 and SL3 hereafter. Seen from the $2\theta/\omega$ scan shown in Figure 6-2(a), two strong diffraction peaks at around 49.8° and 50.6° accompanying with several weak peaks were observed in SL24. The two strong peaks, which correspond to (111) of R-PZT and T-PZT, respectively, show the periodicity within the T-PZT and R-PZT layers. The peaks that marked with an asterisk represent the periodicity of interface of two T-PZT and R-PZT layers. As the layer thickness decreased, the (111) peaks weakened gradually while the superlattice peaks become stronger and stronger. When the layer thickness is down to 3 nm, the (111) T-PZT and R-PZT peaks disappeared and one strong superlattice peak was observed, showing the long periodicity of the T-PZT and R-PZT artificial interface. Consistent patterns in reciprocal space mapping (RSM) were shown in Figure 6-2(b)-(d). Here the white broken line, connecting the substrate peak with original point, denotes the completely relaxed lattice constant of each phase. It is shown that T-PZT and R-PZT layers in SL24 almost released from the substrate, and the superlattice structure in SL3 obtained a tensile misfit strain.

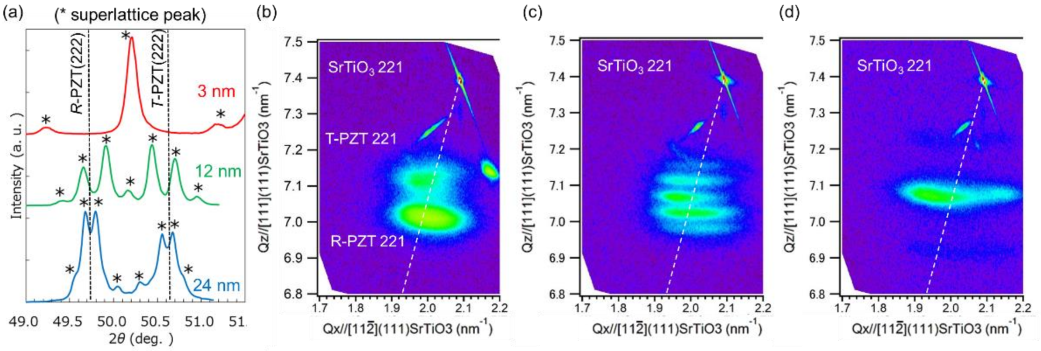

Figure 6-2 XRD patterns of (a) $2\theta/\omega$ scan and RSM of (b) SL24, (c) SL12, (d) SL3

The domain structure of the superlattice films was characterized using ABF-STEM shown in Figure 6-3. In SL12, the striped contrast indicating the {101} twin boundaries [93] of the 90°-domains was observed in the T-PZT layer. The striped domain structure also suggests that the T-PZT layers are spontaneously poled without any extremal bias field applied on the film. On the contrary, the similar striped contrast is not observed in SL3. It is indicated that the multi-domained film will change to a single-domain state as the layer thickness decreases.

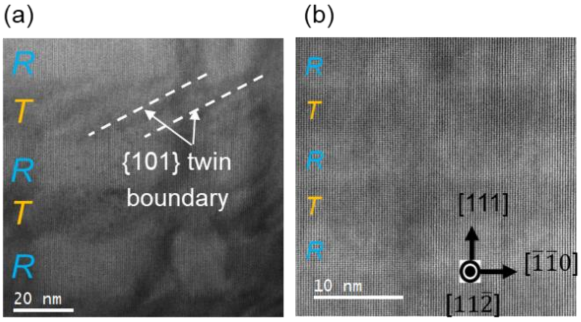

Figure 6-3 STEM images of the cross-sectional of the superlattice films. (a) SL12, (b) SL3

The polarization state of SL3 was analyzed by HAADF-STEM as shown in Figure 6-4. First, positions of the A-site atoms, Pb and B-site atoms, Zr/Ti, were characterized according the different brightness in the

STEM image. Then the center of the perovskite unit cell was confirmed by the B-site atoms and the polarization vector was found by characterizing the difference between the B-site center and A-site atom. It is clearly seen that the polarization state is divided in two parts by the inaccurate polarization states at the interface where the lattice structure distorts severely. However, the average polarization states in T-PZT and R-PZT layers are different from those in PZT bulks, and agree with the polarization state of *aac*-phase as discussed in Figure 5-5.

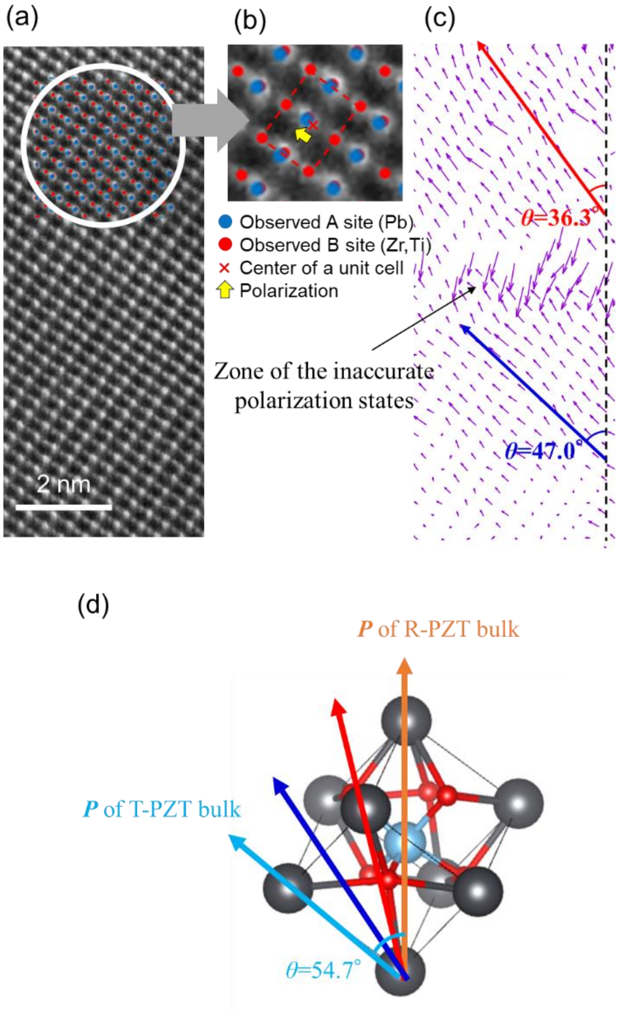

Figure 6-5 Characterization of the polarization state in SL3. (a) Positions of A-site and B-site atoms observed in the STEM image. (b) The approach to confirm the polarization vector in a perovskite unit cell. (c) The distribution of the polarization state of each unit cell and the average polarization direction of the layer. (d) The schematic image of polarization state in the superlattice film compared with that of the bulks.

The ferroelectric hysteresis loop of the fabricated films is shown in Figure 6-6. Observed remanent polarization P_r of the superlattice films is in between the theoretical values of the T-PZT bulk and R-PZT bulk. And P_r increased slightly as the layer thickness decreased.

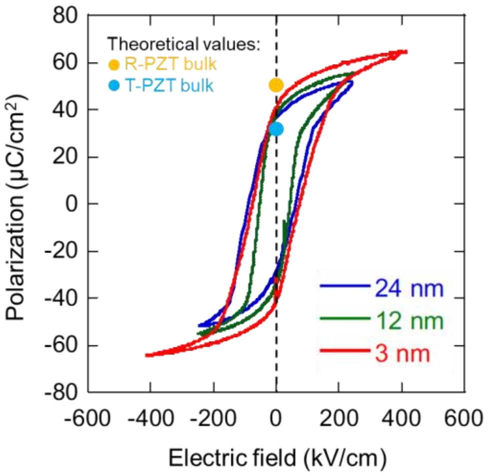

Figure 6-6 Hysteresis loop of the superlattice films, compared with the theoretical values of the PZT bulks

6.3.2 Dielectric and piezoelectric properties of superlattice films

The dielectric properties were measured by an LCR meter from 1 kHz to 1 MHz. As shown in Figure 3 3, The dielectric constant is stable within the measured range, dielectric loss is lower than 0.1, indicating that the fabricated electrodes showed excellent conductivity that would not affect the electrical properties of the PZT samples. In spite of the relative higher ε_r measured in SL12, there is no appreciable change between the fabricated films, which can be considered that the layer thickness does not account for the effect of ε_r.

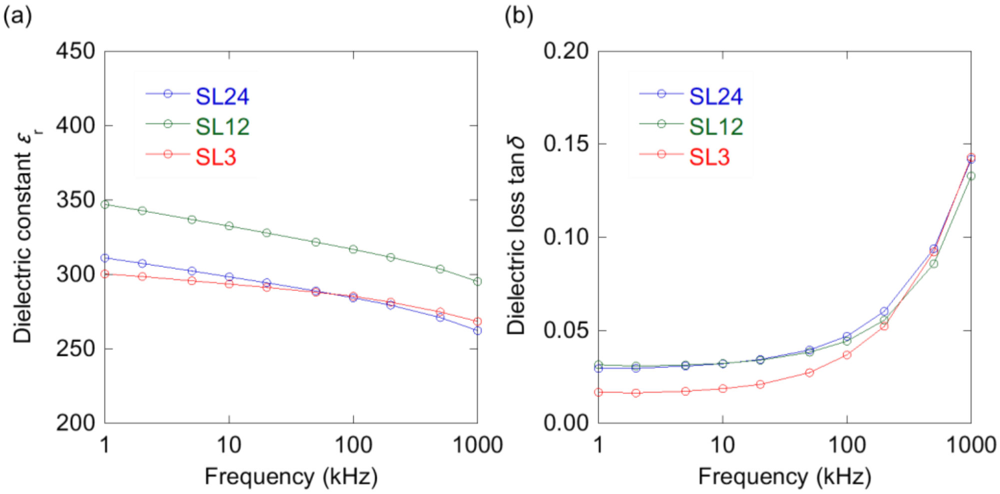

Figure 6-7 Frequency response on (a) dielectric constant and (b) dielectric loss from 1kHz to 1 MHz for the fabricated superlattice films

The piezoelectric response of the fabricated superlattice films were characterized by the time-resolved synchrotron XRD. The characterization procedure is illustrated in Figure 6-8. First, the focused monochrome x-ray with a wavelength of 0.1 nm is irradiated on the Pt electrode. Then The XRD pattern of the sample is characterized with a periodical pulse voltage of 200-300 ns applied on the electrode. It can be seen from Figure 6-8(b) that the XRD pattern shifts with the application of the voltage, due to the piezoelectric effect of the film.

Afterwards, d_{33} of T-PZT and R-PZT layers can be deduced from the difference of the shifted peaks as illustrated in Figure 6-8(c). First, with the model of T-PZT and R-PZT deposited alternatively, the thickness and lattice constant of each layer are used as the parameters for fitting. Then the position and intensity of the peaks are fit with respect to the peak profile of 0V to determine the corresponded lattice constant. After that the peak position is fit with respect to the peak profile of 10V to determine change of the lattice constant.

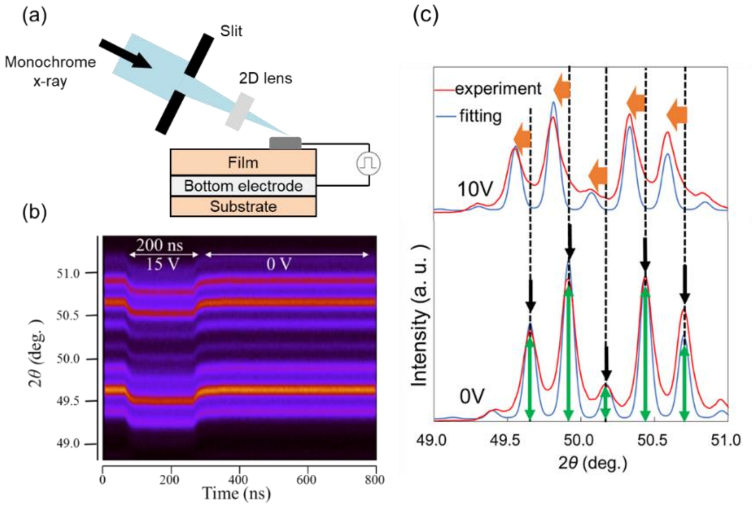

Figure 6-8 Characterization of the piezoelectric response by the time-resolved synchrotron XRD. (a) Schematic image of focused monochrome x-ray irradiated on the sample. (b) XRD patterns of the sample with pulse voltage applied on the electrode. (c) Calculation of d_{33} for each layer by fitting the peak profiles with the change of lattice constants

The peak profiles measured by time-resolved synchrotron XRD and the PFM measurement are shown in Figure 6-9, and summarized in Figure 6-10(a). It is worth noting that SL3 has the best d_{33} among the fabricated films, which verifies the contribution of a single-domain superlattice structure to the improvement of the piezoelectric response. The dependence of d_{33} in either layer agrees with that of the total layer, indicating that the enhanced d_{33} derives from the synergy of both T-PZT and R-PZT, instead of the possibility of a giant improvement in only one layer. Figure 6-10(b) shows the theoretical result of d_{33} for comparison. It is shown that d_{33} of the single-layer films is close to the theoretical values, and d_{33} of SL3 is close to the case of $u_m = 0$, which exceeds the piezoelectric property of the single-layer films. However, the measured polarization state, *aac*-phase in both layers, is not accordance with the case of $u_m = 0$. It would be due to the low accuracy of the measurement or the different coefficients used in the theoretical analysis. Nevertheless, the strategy to achieve the single-domain structure in the superlattice films and improve the piezoelectric response has been clarified in this study. If different lateral stress is induced in the film, for example, depositing films on different substrates, a higher d_{33} which can be comparable to the free bulks can be expected.

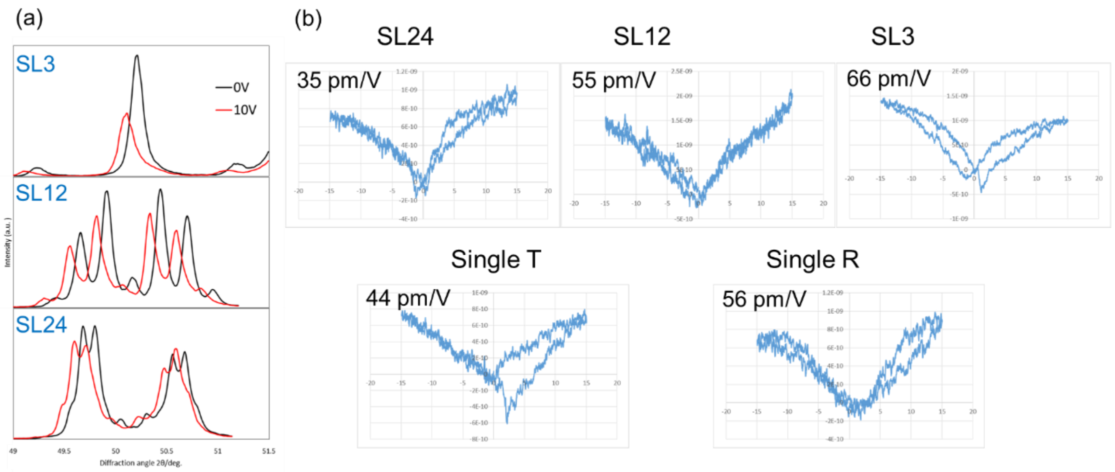

Figure 6-9 (a) The peak profiles measured by time-resolved synchrotron XRD and (b) the PFM measurement

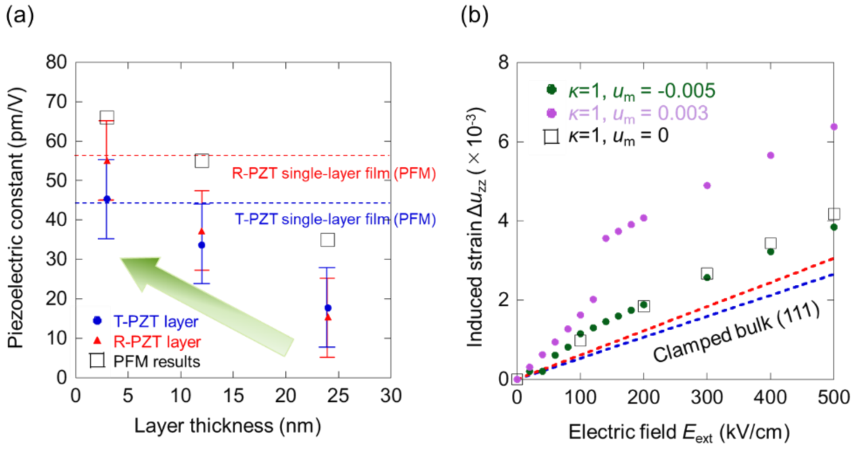

Figure 6-10 Comparison of d_{33} of the superlattice films. (a) Experimental results, (b) theoretical results.

6.4 Conclusion

The superlattice films according to the theoretical model are fabricated by PLD on STO (111). The following conclusion can be obtained as a validation of the theoretical analysis.

1) The single-domain structure formed in the superlattice films. From the characterization of XRD and STEM, the multidomain structure forms in the film with the thickness over 12 nm but the single-domain structure forms in that with 3 nm thickness. The superlattice structure can serve as an effective strategy to utilizing the lateral stress in the films with the thickness over 100 nm.

2) Unique polarization state in the single-domain films. A tilted polarization direction is characterized in SL3, agreeing with the *aac*-phase in the theoretical study. This polarization state is different from that in the PZT bulks, and indicates the polarization rotation which would improve the piezoelectric response.

3) Enhanced d_{33} in the single-domain structured superlattice film. Piezoelectric constant d_{33} of 66 pm/V is achieved in SL3, higher than the clamped PZT bulks as well as the multidomain films of which the layer thickness over 12 nm. The enhancement agrees with the theoretical analysis. It is considered that the polarization state of the *aac* phase would be susceptible to the external electric field and generate the polarization rotation easily.

6.5 References

88. V. Anbusathaiah, D. Kan, F. C. Kartawidjaja, R. Mahjoub, M. A. Arredondo, S. Wicks, I. Takeuchi, J. Wang, and V. Nagarajan. Labile ferroelastic nanodomains in bilayered ferroelectric thin films. *Advanced Materials*, **21**, 3497-3502 (2009).
89. A. K. Yadav, C. T. Nelson, S. L. Hsu, Z. Hong, J. D. Clarkson, C. M. Schlepütz, A. R. Damodaran, P. Shafer, E. Arenholz, L. R. Dedon, D. Chen, A. Vishwanath, A. M. Minor, L. Q. Chen, J. F. Scott, L. W. Martin and R. Ramesh. Observation of polar vortices in oxide superlattices. *Nature*, **530**, 198-201 (2016).
90. A. R. Damodaran, J. D. Clarkson, Z. Hong, H. Liu, A. K. Yadav, C. T. Nelson, S. L. Hsu, M. R. McCarter, K. D. Park, V. Kravtsov, A. Farhan, Y. Dong, Z. Cai, H. Zhou, P. Aguado-Puente, P. García-Fernández, J. Íñiguez, J. Junquera, A. Scholl, M. B. Raschke, L. Q. Chen, D. D. Fong, R. Ramesh and L. W. Martin. Phase coexistence and electric-field control of toroidal order in oxide superlattices. *Nature Materials*, **16**, 1003-1009 (2017).
91. Y. Iguchi, T. Yamada, O. Sakata, M. Yoshino, and T. Nagasaki. Fabrication of $(Pb_{0.9}Sr_{0.1})TiO_3/SrTiO_3$ artificial superlattice thin films and their electromechanical response. *Journal of the Ceramic Society of Japan*, **128**, 431-435 (2020).
92. T. Yamada, Y. Ebihara, T. Kiguchi, O. Sakata, H. Morioka, T. Shimizu, H. Funakubo, T. J. Konno, M. Yoshino and T. Nagasaki. Fabrication and characterization of (111)-epitaxial $Pb(Zr_{0.35}Ti_{0.65})O_3$/ $Pb(Zr_{0.65}Ti_{0.35})O_3$ artificial superlattice thin films. *Japanese Journal of Applied Physics*, **55**, 10TA20 (2016).
93. T. Yamada, J. Yasumoto, D. Ito, O. Sakata, Y. Imai, T. Kiguchi, T. Shirashi, T. Shimizu, H. Funakubo, M. Yoshino and T. Nagasaki. Negligible substrate clamping effect on piezoelectric response in (111)-epitaxial tetragonal $Pb(Zr,Ti)O_3$ films. *Journal of Applied Physics*, **118**, 072012 (2015).

Chapter 7 - General conclusion and future prospective

7.1 General conclusion

This dissertation aims on improving the electrical and electromechanical properties of the piezoelectric materials used for miniaturized PEH devices, with the strategies to deal with the internal stress induced in the materials. For one thing, it is possible to eliminate this internal stress to avoid the disadvantage of the substrate clamping and thus achieve the piezoelectric properties comparable to the bulks. The effectiveness is proved by the nanorod array theoretically and experimentally (Chapter 2–Chapter 4). For another thing, it is also possible to utilize this internal stress to control the polarization rotation, which can exhibit the similar behavior as the phase transition near MPB for the ferroelectric bulks. The effectiveness is proved by the superlattice film theoretically and experimentally (Chapter 5–Chapter 6). Accomplishments and conclusion of each chapter are presented below in detail.

Chapter 2 - Theoretical analysis on the output performance of piezoelectric nanorod arrays

From the perspective of reducing the clamping stress in the film, using the piezoelectric nanorod array would be an effective way to improve the output performance along the out-of-plane direction. In this chapter, a theoretical model of a nanorod array is studied on the output voltage and power, by deducing their expressions from the piezoelectric equations and conducting the FEM simulation in the software *COMSOL Multiphysics*. The nanorod structure has been proved to be an effective strategy to reduce the substrate clamping and enhance the out-of-plane output performance via the theoretical analysis. It is shown that a low lateral stress is induced in the piezoelectric unit with a large aspect ratio, indicating the easier deformation of the nanorods than that of the film when the same stress is applied. d_{33} of the nanorods is closed to the bulk d_{33} which is 33% higher than the clamped direct d_{33} for the film, and thus a 77% enhanced FOM_{33}. And the density of the nanorod array could achieve larger V_{open} and P_{out} than that of a dense film, showing a larger impact over the aspect ratio. The cantilever achieves large input power at resonance due to a low spring constant, while the 33-mode structures show the $P_{\mathrm{out}}/P_{\mathrm{in}}$ twice higher than that of the 31-mode film, because the substrate does not account for the energy conversion in the 33 mode. Finally, it is shown that the output of the nanorods increases with decreasing device length and tends exceed that of the film cantilever in the 31 mode when the length is less than 700 μm, because the resonant frequency of the film cantilever in the 31 mode significantly deviates from the vibration frequency.

Chapter 3 - Enhanced FOM from the decreased density of PZT nanorod arrays

The theoretical study has predicted the enhanced output power of using the nanorod array, due to the increased d_{33} and the decreased density compared with a 33-mode film. It is worth noting that the decreased density achieved in the nanorod array is significant to improve FOM for the PEH application, since there is seldom straightforward way to achieve a high FOM in a piezoelectric film due to the positive correlation between dielectric and piezoelectric properties. However, the effect of the decreased density was scarcely validated by direct experiments. This study experimentally clarified that the effective FOM of the PZT nanorod array can be enhanced by the decreased density by comparing the nanorods with a film having the same orientation and similar domain structure. This approach enables us to independently control the piezoelectric and dielectric constants of materials, making it possible to lower the effective dielectric constant while maintaining the piezoelectric constant. In addition, a method to distinguishes the effect of the decreased density from that of the other factors is proposed, which makes it possible to evaluate the FOM of the nanorod array in a more accurate way.

Chapter 4 - Fabrication of PZT nanorods by RF-magnetron sputtering

For the purpose of commercializing the nanorod-based PEH devices, PZT nanorods are expected to grow in an area up to several cm^2 and thus the fabrication using RF-magnetron sputtering is taken into consideration. Different from the fabrication in PLD, it is difficult to use high pressure for sputtering because the growth rate will be severely reduced by the interaction of the gas molecules. In this chapter, the strategy to grow PZT nanorods without elevating the pressure and the optimal fabrication condition are investigated. It is shown that the effect of the O_2 partial pressure plays a considerable important role in growing PZT nanorods, which makes it possible to achieve the nanorod structure at low pressure and thus the rapid growth can be the dominant factor to grow the nanorods by adjusting Ar:O_2. Finally, a nanorod-like PZT is obtained with Ar:O_2 = 2:1 at 650 ℃, even though using a general working pressure of 2.7 Pa. Unfortunately, the expected nanorod structure has not been realized by RF-magnetron sputtering with the studied conditions, due to the limitation of the used equipment. Nevertheless, the feasibility of growing nanorods can be predicted by the clarifying the effect of the temperature and O_2 pressure in the study. The possibility to achieve nanorods would be enhanced by further increasing the growth rate of sputtering.

Chapter 5 - Theoretical analysis on piezoelectric response of ferroelectric superlattice films

Previous studies have revealed the possibility of improving the piezoelectric response by utilizing the lateral stress. However, it is difficult to validate this possibility in a single-layer film with the thickness over 100 nm, in which a multidomain structure will form due to the local deformation determined by the minimal elastic energy. The possibility of utilizing the lateral stress to control the polarization rotation is predicted with the LGD phenomenological theory, with respect to the single-domain structure in the single-layer film and the superlattice film. u_{m}-E_{ext} phase diagrams of the single-layer films confirm this possibility, and detailed analyses on the stabilized polarization, dielectric and piezoelectric properties of the (111)-oritened superlattice films reveal the potential of exhibiting enhanced piezoelectric response. It is shown that a unique polarization state known as *aac* phase is stabilized in the single-domain films, different from the polarization in bulks. When the external electric field applied, discontinuity of the polarization extension, dielectric constant and piezoelectric constant is observed at *aac-r* phase transition boundary. It is worth noting that improved piezoelectric response that exceeds the clamped bulks and is comparable to the free bulks is observed by utilizing the lateral stress in the films.

Chapter 6 - Large piezoelectric response from polarization rotation in artificial superlattice films

The theoretical analysis has predicted the enhanced piezoelectric property by achieving a desired misfit strain to induce the polarization rotation in a single-domain film. The prediction can be validated by fabricating the superlattice films. In this chapter, (111)-epitaxial artificial superlattice films consisting of $Pb(Zr_{0.4}Ti_{0.6})O_3$ and $Pb(Zr_{0.6}Ti_{0.4})O_3$ were fabricated by PLD, which is in accordance with the theoretical model. From the characterization of XRD and STEM, the multidomain structure forms in the film with the thickness over 12 nm but the single-domain structure forms in that with 3 nm thickness. The superlattice structure can serve as an effective strategy to utilizing the lateral stress in the films with the thickness over 100 nm. For the superlattice film with 3 nm thickness, a tilted polarization direction is characterized, agreeing with the *aac*-phase in the theoretical study. This polarization state is different from that in the PZT bulks, and indicates the polarization rotation which would improve the piezoelectric response. The piezoelectric constant d_{33} of 66 pm/V is achieved, higher than the clamped PZT bulks as well as the multidomain films of which the layer thickness over 12 nm. The enhancement agrees with the theoretical analysis. It is considered that the polarization state of the *aac* phase would be susceptible to the external electric field and generate the polarization rotation easily.

7.2 Positioning and meaning of this research method

Figure 7-1 shows position of the piezoelectric properties and FOM achieved in this dissertation, with the reference of the theoretical values. The effectiveness of the approaches employed in this research is described as follows.

The PZT nanorod structure has been achieved in order to improve the output performance by releasing the substrate clamping. The fabricated $Pb(Zr_{0.35}Ti_{0.65})O_3$ nanorod arrays discussed in Chapter 3 show higher d_{33} and effective FOM than the clamped films. In addition, the output performance of the nanorod arrays could be further improved by (1) employing spatially separated nanorods with the MPB composition, and (2) further decreasing the density of the nanorod array. The (111)-oriented PZT nanorods, fabricated at elevated O_2 pressure by PLD in other works, show an excellent d_{33} and competitive FOM, compared with the theoretical values. The theoretical analyses on the output performance, conducted in Chapter 2, show the possibility to achieve a unclamped d_{33} but much higher FOM which would exceed the best-performing PZT films.

The PZT superlattice films have been investigated in order to improve the piezoelectric properties by achieving the desired stress state in the films. Unfortunately, the fabricated superlattice films discussed in Chapter 6 did not show an expected piezoelectric constant that should have exceeded the theoretical values of the single-layer films. The reason could be due to inaccurate evaluation of d_{33} or the difficulty in evaluating the internal stress in the films. Nevertheless, the superlattice film with the 3-nm-thick layer shows an improved d_{33} and higher than the single-layer film that was fabricated in the same method, indicating the effectiveness of this strategy. The potential of achieving a much higher piezoelectric response is revealed by the theoretical analyses in Chapter 5. For example, by depositing superlattice films on different substrates to achieve different misfit strain u_m, d_{33} and FOM that are comparable to the best-performing PZT films can be expected.

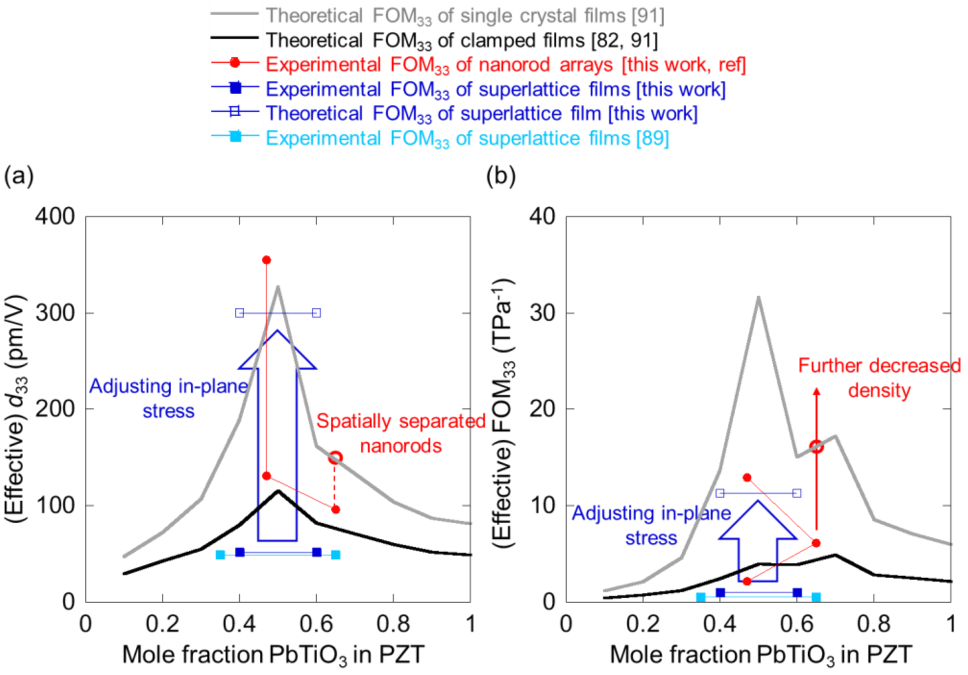

Figure 7-1 Positioning and meaning of this research method

7.3 Future perspective

Studies in this thesis have shown the feasibility of achieving enhanced output performance in piezoelectric PZT thin films via controlling the stress in the films, such as nanorods to reduce the clamping and superlattice films to improve the physical properties using phase transition. However, there are still many topics remained to be solved in the future study. On one hand, the studied material is only limited to PZT, and it is not yet known whether the strategy can work well for other piezoelectric materials. In particular, due to the enforcement of the RoHS Directive including the ban on lead-containing products in the EU in 2007, it is required to exploit the substitute of lead-containing piezoelectric elements including PZT. On the other hand, the improved PZT materials achieved by this strategy have not met the commercial use for PEH devices. As mentioned in Chapter 2 and Chapter 3, the mechanical strength and damping caused by the vibration are also the important issues to achieve enhanced and stable output power, which has not been considered in details in this study. The superlattice films may lead to a wide range of applications both in resonant and off-resonant PEH, but the lateral stress is difficult to control precisely as the desired misfit strain is limited by the finitely selected piezoelectric materials and substrates. More efforts need to be taken on the conversion of experimental progress to practical use in the future study.

7.4 References

94. M. J. Haun, E. Furman, S. J. Jang, and L. E. Cross. Thermodynamic theory of the lead zirconate-titanate solid solution system, part V: Theoretical calculations. *Ferroelectrics*, **99**, 63-86 (1989).

Appendix

Programming in Mathematica

The theoretical analyses on fully clamped films and superlattice films, discussed in Chapter 5, are conducted in the technical computing system *Wolfram Mathematica 12.0*. The related code is given as follows.

(* Coefficients *)

```
(* um0 in superlattice *)
aT = 4.04*10^(-10);  cT = 4.14*10^(-10);  aR = 4.08*10^(-10);
a0T = (aT*aT*cT)^(1/3);  a0R = aR;
umT0 = ( (a0T + a0R)/2 - a0T ) / ( (a0T + a0R)/2 );
umR0 = ( (a0T + a0R)/2 - a0R) / ( (a0T + a0R)/2 );

(* s, Q and α *)
s11T = 8.6*10^(-12); s12T = -2.8*10^(-12); s44T = 21.2*10^(-12);
s11R = 8.8*10^(-12); s12R = -2.9*10^(-12); s44R = 24.6*10^(-12);

Q11T = 8.116*10^(-2); Q12T = -2.95*10^(-2); Q44T = 6.71*10^(-2);
Q11R = 7.26*10^(-2); Q12R = -2.708*10^(-2); Q44R = 6.293*10^(-2);

α1T = -8.34*10^7; α11T = 3.614*10^7; α12T = 3.233*10^8;
α111T = 1.859*10^8; α112T = 8.503*10^8; α123T = -4.063*10^9;
α1R = -7.904*10^7; α11R = 13.62*10^7; α12R = 2.391*10^8;
α111R = 2.713*10^8; α112R = 12.13*10^8; α123R = -5.69*10^9;
```

(* Original expression of G *)

```
GP24 =α1*(P1^2 + P2^2 + P3^2) +α11*(P1^4 + P2^4 + P3^4) +α12*(P1^2*P2^2 + P2^2*P3^2 + P3^2*P1^2);
GP6 =α111*(P1^6 + P2^6 + P3^6) +α112*( P1^4*(P2^2 + P3^2) + P2^4*(P3^2 + P1^2) + P3^4*(P1^2 + P2^2) ) +α123*(P1*P2*P3)^2;
Gσ = -s11/2*(σ1^2 +σ2^2 +σ3^2) -s12*(σ1*σ2 + σ2*σ3 + σ3*σ1) -s44/2*(σ4^2 + σ5^2 + σ6^2);
GσP = -Q11*(σ1*P1^2 + σ2*P2^2 + σ3*P3^2) -Q12*( σ1*(P2^2 + P3^2) + σ2*(P3^2 + P1^2) + σ3*(P1^2 + P2^2) ) - Q44*( σ4*P2*P3 + σ5*P3*P1 + σ6*P1*P2);
G0 = GP24 +Gσ +GσP;
```

(* G expressed by P,um, (001)-oriented *)

```
G0Plane = G0 /. {σ3 -> 0, σ4 -> 0, σ5 -> 0};
u1Plane = -D[G0Plane, σ1]; u2Plane = -D[G0Plane, σ2]; u6Plane = -D[G0Plane*2, σ6];
σPlaneSol = Solve[{u1Plane == um, u2Plane == um, u6Plane == 0}, {σ1, σ2, σ6}];
G0Pum = (G0Plane + σ1*um + σ2*um) /. σPlaneSol //Simplify;
```

(* Expression of q31 for (001) films*)

```
q31m = -1/2*D[σ1 /. σPlaneSol, {P3, 2}] // Simplify;
```

(*Rotation matrix expressed by Euler angle*)

```
Rx = {{1, 0, 0}, {0, Cos[θ], -Sin[θ]}, {0, Sin[θ], Cos[θ]}} /. θ -> -ArcCos[1/Sqrt[3]];
Rzold = {{Cos[ψ], -Sin[ψ], 0}, {Sin[ψ], Cos[ψ], 0}, {0, 0, 1}} /. ψ -> -Pi/4;
Rznew = {{Cos[φ], -Sin[φ], 0}, {Sin[φ], Cos[φ], 0}, {0, 0, 1}} /. φ -> Pi;

Rmat = Inverse[Rzold.Rx.Rznew]; Rmat // MatrixForm
```

(* G expressed by P,um, with coordinate transformation, (111)-oriented *)

```
σnew = SparseArray[{{1, 1} -> σxx, {1, 2} -> σxy, {1, 3} -> σzx, {2, 1} -> σxy, {2, 2} -> σyy, {2, 3} -> σyz,
{3, 1} -> σzx, {3, 2} -> σyz, {3, 3} -> σzz}];
σold = Inverse[Rmat].σnew.Rmat;
G0new = G0old /. {σ1 -> σold[[1, 1]], σ2 -> σold[[2, 2]], σ3 -> σold[[3, 3]] , σ6 -> σold[[1, 2]], σ4 -> σold[[2,
3]], σ5 -> σold[[3, 1]]};

G0newPlane = G0new /. {σzz -> 0, σyz -> 0, σzx -> 0};
uxxPlane = -D[G0newPlane, σxx];
uyyPlane = -D[G0newPlane, σyy];
uxyPlane = -D[G0newPlane, σxy];

σPlaneSol = Solve[{uxxPlane == um, uyyPlane == um, uxyPlane == 0}, {σxx, σyy, σxy}];
G0newPum = (G0newPlane + σxx*um + σyy*um) /. σPlaneSol // Simplify;
```

(* Expression of Qzzzz and qzzxx for 111 films*)

```
uzz = -D[G0new, σzz] /. σPlaneSol // Simplify; uzzmid = uzz[[1]] /. {σzz -> 0};
Qzzzzmid = (1/Sqrt[3])*(D[uzzmid, P1] + D[uzzmid, P2] + D[uzzmid, P3]);
Qzzzz = (1/2/Sqrt[3])*(D[Qzzzzmid, P1] + D[Qzzzzmid, P2] + D[Qzzzzmid, P3]) // Simplify

σxxmid = σxx /. σPlaneSol // Simplify;
```

```
qzzxxmid = (1/Sqrt[3])*(D[σxxmid[[1]], P1] + D[σxxmid[[1]], P2] + D[σxxmid[[1]], P3]);
qzzxx = (-1/2/Sqrt[3])*(D[qzzxxmid, P1] + D[qzzxxmid, P2] + D[qzzxxmid, P3]) // Simplify
```

(* Total G of the superlattice films *)

```
epsilon0 = 8.854*10^(-12);

G0PumT = G0Pum /. {s11 -> s11T, s12 -> s12T, s44 -> s44T, Q11 -> Q11T, Q12 -> Q12T, Q44 -> Q44T, α1
-> α1T, α11 -> α11T, α12 -> α12T, P1 -> P1T, P2 -> P2T, P3 -> P3T} // Expand;
G0PumR = G0Pum /. {s11 -> s11R, s12 -> s12R, s44 -> s44R, Q11 -> Q11R, Q12 -> Q12R, Q44 -> Q44R,
α1 -> α1R, α11 -> α11R, α12 -> α12R, P1 -> P1R, P2 -> P2R, P3 -> P3R} // Expand;
GDepol = kappa/24/epsilon0*( (P1T + P2T + P3T) - (P1R + P2R + P3R) )^2;
Gext = -1/Sqrt[3]*( (P1T + P2T + P3T) + (P1R + P2R + P3R) )*Eext;
GTotal = (G0PumT + G0PumR)/2 + GDepol + Gext // Simplify
```

(* Solution for um- Eext phase diagram *)

```
GTotal2 = GTotal /. {kappa -> 0};

PDT = {}; PDR = {};

For[umfun = -10, umfun <= 10, umfun += 1,    (*10^(-3)*)
    GTotal3 = GTotal2 /. {um -> umfun*10^(-3)};
    For[Eextfun = 0, Eextfun <= 1000, Eextfun += 100, (*kV/cm*)
      GTotal4 = GTotal3 /. {Eext -> Eextfun*10^5};
      PSol = NSolve[{D[GTotal4, P1T] == 0, D[GTotal4, P2T] == 0, D[GTotal4, P3T] == 0, D[GTotal4,
P1R] == 0, D[GTotal4, P2R] == 0, D[GTotal4, P3R] == 0}, {P1T, P2T, P3T, P1R, P2R, P3R}, Reals];
      GTotalSol = GTotal4 /. PSol;
      opt = Position[GTotalSol, GTotalSol // Min];
      Pmin = PSol[[ opt[[1]] ]];

      P1TSol = Round[Abs[P1T], 0.001] /. Pmin[[1, 1]];
      P2TSol = Round[Abs[P2T], 0.001] /. Pmin[[1, 2]];
      P3TSol = Round[Abs[P3T], 0.001] /. Pmin[[1, 3]];
      P1RSol = Round[Abs[P1R], 0.001] /. Pmin[[1, 4]];
      P2RSol = Round[Abs[P2R], 0.001] /. Pmin[[1, 5]];
      P3RSol = Round[Abs[P3R], 0.001] /. Pmin[[1, 6]];

      phaseT = 0; phaseR = 0;
```

```
    If[P1TSol == P2TSol == P3TSol == 0, phaseT = 1,
    If[(P1TSol == P2TSol == 0 && P3TSol != 0) || (P2TSol == P3TSol == 0 && P1TSol != 0) || (P3TSol
== P1TSol == 0 && P2TSol != 0), phaseT = 2,
      If[(P1TSol != 0 && P2TSol != 0 && P3TSol == 0) || (P1TSol != 0 && P2TSol == 0 && P3TSol != 0)
|| (P1TSol == 0 && P2TSol != 0 && P3TSol != 0), phaseT = 3,
        If[(P1TSol == P2TSol != P3TSol != 0) || (P2TSol == P3TSol != P1TSol != 0) || (P3TSol == P1TSol !=
P2TSol != 0), phaseT = 4,
          If[P1TSol == P2TSol == P3TSol != 0, phaseT = 5] ] ] ] ];

If[P1RSol == P2RSol == P3RSol == 0, phaseR = 1,
    If[(P1RSol == P2RSol == 0 && P3RSol != 0) || (P2RSol == P3RSol == 0 && P1RSol != 0) || (P3RSol
== P1RSol == 0 && P2RSol != 0), phaseR = 2,
      If[(P1RSol != 0 && P2RSol != 0 && P3RSol == 0) || (P1RSol != 0 && P2RSol == 0 && P3RSol != 0)
|| (P1RSol == 0 && P2RSol != 0 && P3RSol != 0), phaseR = 3,
        If[(P1RSol == P2RSol != P3RSol != 0) || (P2RSol == P3RSol != P1RSol != 0) || (P3RSol ==
P1RSol != P2RSol != 0), phaseR = 4,
          If[P1RSol == P2RSol == P3RSol != 0, phaseR = 5] ] ] ] ];
AppendTo[PDT, {umfun, Eextfun, phaseT}];
AppendTo[PDR, {umfun, Eextfun, phaseR}];    ];    ];
```

(* Solution for P3r *)

```
GTotal2 = GTotal /. {kappa -> 0, um -> 0} // Simplify;
GTotalr = GTotal2 /. {Eext -> 0*10^5};

PrSol = NSolve[{D[GTotalr, P1T] == 0, D[GTotalr, P2T] == 0, D[GTotalr, P3T] == 0, D[GTotalr, P1R] ==
0, D[GTotalr, P2R] == 0, D[GTotalr, P3R] == 0}, {P1T, P2T, P3T, P1R, P2R, P3R}, Reals];
GTotalrSol = GTotalr /. PrSol;
optr = Position[GTotalrSol, GTotalrSol // Min];
Prmin = PrSol[[ optr[[1]] ]]

PzrT = ((Round[Abs[P1T], 0.00001] + Round[Abs[P2T], 0.00001] + Round[Abs[P3T], 0.00001])/Sqrt[3] )
/. Prmin[[1]]
PrT = Sqrt[P1T^2 + P2T^2 + P3T^2] /. Prmin[[1]];
PzrR = ((Round[Abs[P1R], 0.00001] + Round[Abs[P2R], 0.00001] +Round[Abs[P3R], 0.00001])/Sqrt[3] )
/. Prmin[[1]]
PrR = Sqrt[P1R^2 + P2R^2 + P3R^2] /. Prmin[[1]];
```

(* Solution for dielectric and piezoelectric properties *)

```
QzzzzT = Qzzzz /. {s11 -> s11T, s12 -> s12T, s44 -> s44T, Q11 -> Q11T, Q12 -> Q12T, Q44 -> Q44T};
QzzzzR = Qzzzz /. {s11 -> s11R, s12 -> s12R, s44 -> s44R, Q11 -> Q11R, Q12 -> Q12R, Q44 -> Q44R};
qzzxxT = qzzxx /. {s11 -> s11T, s12 -> s12T, s44 -> s44T, Q11 -> Q11T, Q12 -> Q12T, Q44 -> Q44T};
qzzxxR = qzzxx /. {s11 -> s11R, s12 -> s12R, s44 -> s44R, Q11 -> Q11R, Q12 -> Q12R, Q44 -> Q44R};

Abscissa = {};    Ordinate = {};
For[Eextfun = 0, Eextfun <= 1000, Eextfun += 100, (*kV/cm*)
   GTotal3 = GTotal2 /. {Eext -> Eextfun*10^5};
   PSol = NSolve[{D[GTotal3, P1T] == 0, D[GTotal3, P2T] == 0, D[GTotal3, P3T] == 0, D[GTotal3, P1R]
== 0, D[GTotal3, P2R] == 0, D[GTotal3, P3R] == 0}, {P1T, P2T, P3T, P1R, P2R, P3R}, Reals];
   GTotalSol = GTotal3 /. PSol;
   opt = Position[GTotalSol, GTotalSol // Min];
   Pmin = PSol[[ opt[[1]] ]];

   PzT = ((Round[Abs[P1T], 0.001] + Round[Abs[P2T], 0.001] + Round[Abs[P3T], 0.001])/Sqrt[3] ) /.
Pmin[[1]];
   PzR = ((Round[Abs[P1R], 0.001] + Round[Abs[P2R], 0.001] + Round[Abs[P3R], 0.001])/Sqrt[3] ) /.
Pmin[[1]];

   EzT = 1/Sqrt[3]*D[GTotal, P1T] + 1/Sqrt[3]*D[GTotal, P2T] + 1/Sqrt[3]*D[GTotal, P3T];
   EzR = 1/Sqrt[3]*D[GTotal, P1R] + 1/Sqrt[3]*D[GTotal, P2R] + 1/Sqrt[3]*D[GTotal, P3R];
   chizzT = 1/Sqrt[3]*D[EzT, P1T] + 1/Sqrt[3]*D[EzT, P2T] + 1/Sqrt[3]*D[EzT, P3T];
   chizzR = 1/Sqrt[3]*D[EzR, P1R] + 1/Sqrt[3]*D[EzR, P2R] + 1/Sqrt[3]*D[EzR, P3R];
   chizzTsol = chizzT /. Pmin; chizzRsol = chizzR /. Pmin;
   epsilonzzT = 1/chizzTsol/epsilon0; epsilonzzR = 1/chizzRsol/epsilon0;

   deltauzzT = QzzzzT*(PzT^2 - PzrT^2)*1000; (*10^(-3)*)
   deltauzzR = QzzzzR*(PzR^2 - PzrR^2)*1000; (*10^(-3)*)
   deltauzz = (deltauzzT + deltauzzR)/2;

   AppendTo[Abscissa, Eextfun];
   AppendTo[Ordinate, Abs[deltauzz]]; ];
```

Accomplishments

Publications

Chapter 2

[1] **J. Song**, T. Yamada, M. Yoshino, and T. Nagasaki. Theoretical Analysis of Nanogenerators with Aligned Nanorods for Piezoelectric Energy Harvesting. *Sensor. Mater.*, 2019. **31**(11): 3669-3679. (doi: 10.18494/SAM.2019.2149)

Chapter 3

[2] **J. Song**, T. Yamada, K. Okamoto, M. Yoshino, and T. Nagasaki. Enhanced figure of merit in Pb(Zr,Ti)O_3 nanorods for piezoelectric energy harvesting. *AIP Advances*, 2020. In printing. (doi: 10.1063/5.0023937)

Others

[3] **J. Song**, and J. Wang. Ferroelectric materials for vibrational energy harvesting. *Sci. China Tech. Sci.*, 2016. **59**: 1012-1022. (doi:10.1007/s11431-016-6081-7)

[4] **J. Song**, G. Zhao, B. Li, and J. Wang. Design optimization of PVDF-based piezoelectric energy harvesters. *Heliyon*, 2017. **3**: e00377. (doi: 10.1016/j.heliyon.2017. e00377)

[5] T. Yamada, **J. Song**, and T. Nagasaki. Ferroelectric Nanorods: Control and Application to Piezoelectric Energy Harvesting. *AAPPS bulletin*, 2020. **30**:15-20.

Presentations

[1] **J. Song**, T. Yamada, M. Yoshino, T. Nagasaki, "Theoretical investigation of output voltage of piezoelectric nanogenerators with aligned nanorods", in the 10th Japan-China Symposium on Ferroelectric Materials and Their Applications. (Sept. 2018, Nagoya, Japan).

[2] **J. Song**, T. Yamada, M. Yoshino, T. Nagasaki, "Theoretical comparison on output voltage of resonant and off-resonant nanogenerators fabricated with (001)-oriented PZT", in the 38th Electronics Division Meeting of the Ceramic Society of Japan. (Nov. 2018, Kawasaki, Japan).

[3] **J. Song**, T. Yamada, M. Yoshino, T. Nagasaki, "Theoretical analysis of the influence of aspect ratio and density of nanorod arrays for piezoelectric energy harvesting", in the 66th JSAP Spring Meeting. (Mar. 2019, Tokyo, Japan).

[4] **J. Song**, T. Yamada, M. Yoshino, T. Nagasaki, "Study on Output Power of Nanogenerators with Tetragonal Pb(Zr,Ti)O_3 Nanorods for Piezoelectric Energy Harvesting", in joint ISAF-ICE-EMF-IWPM-PFM conference. (July 2019, Lausanne, Switzerland).

[5] **J. Song**, T. Yamada, Y. Ebihara, O. Sakata, T. Kiguchi, M. Yoshino, T. Nagasaki, "Large Piezoelectric Response Driven by Polarization Rotation in $Pb(Zr_{0.4}Ti_{0.6})O_3/Pb(Zr_{0.6}Ti_{0.4})O_3$ Artificial Superlattice Films", in 40th Electronics Division Meeting of the Ceramic Society of Japan. (Nov. 2020, Japan)

Awards

[1] **Best Student Paper Award** of joint ISAF-ICE-EMF-IWPM-PFM conference at EPFL in Lausanne, Switzerland, for the poster. (2019)

Acknowledgements

First of all, I would like to appreciate the dedicated support and guidance from my supervisor, Associate Professor Tomoaki Yamada. When I first came to Japan as a foreign student, I went through many inconvenient things owing to the inexpert language skills and unfamiliar environments. It is in my most difficult time in Japan that Prof. Yamada provided me with many precious suggestions and timely help. Throughout my doctoral study, I kept receiving valuable advice and inspiring ideas from him and being equipped with many scientific principles and practical research techniques. Even for my research career that has become more and more competitive in recent years, he encouraged me and offered much related information, which gave me confidence and perseverance to finish my PhD study.

Then I would like to thank Professor Takanori Nagasaki, Professor Ayae Narutaki, Professor Eiji Ikenaga, Associate Professor Masato Nakaya in Nagoya University, and Associate Professor Takashi Teranishi in Okayama University, for their patient instructions and precious advice on my PhD dissertation and presentation as the members of the thesis screening committee.

Next I would like to thank all the members of the Nagasaki Laboratory, where I spent a pleasant and meaningful time in learning and researching. Professor Takanori Nagasaki, Associate Professor Tomoaki Yamada, Associate Professor Junji Yuhara and Assistant Professor Masahito Yoshino provided me with many valuable suggestions during every regular presentation and helped me with my published papers and conference presentations. Student members, Dr. Daisuke Kato, Dr. Shinya Kondo, Mr. Yohei Ebihara, Mr. Shogo Matsuo, Ms. Mitsuki Kawano and Mr. Yuto Oda who have graduated from the laboratory, as well as Dr. Xueyou Yuan, Mr. Kazuki Okamoto, Mr. Yusuke Iguchi, Mr. Kohei Kawade and other members in the laboratory, also gave me a lot of help and support on my living and researching.

In addition, I would like to acknowledge JST-PRESTO (Grant No. JPMJPR16R9), JST-CREST (Grant No. JPMJCR20Q2), JSPS KAKENHI (Grant Nos. 26709047 (T.Y.) and 19J21955 (K.O.)) and China Scholarship Council (File No. 201808050188) for financially supporting my research. Thank all the people who offered financial or technical support to my research.

Finally, I am grateful to my parents from the bottom of my heart for their emotional and physical support on my study. Without their selfless devotion, I would never persist on the career of the scientific research till today and achieve such accomplishments.